

FLORIDA STATE UNIVERSITY
COLLEGE OF ENGINEERING

LIQUID HELIUM TURBULENT PIPE FLOW AND
MAGNETIC LEVITATION RESEARCH

By

HAMID SANAVANDI

A Dissertation submitted to the
Department of Mechanical Engineering
in partial fulfillment of the
requirements for the degree of
Doctor of Philosophy

2022

Hamid Sanavandi defended this dissertation on June 23, 2022.

The members of the supervisory committee were:

Wei Guo

Professor Directing Dissertation

Jingjiao Guan

University Representative

Louis Cattafesta III

Committee Member

Lance Coolay

Committee Member

The Graduate School has verified and approved the above-named committee members, and certifies that the dissertation has been approved in accordance with university requirements.

I dedicate this dissertation to my family. I never thought having a reunion with them would become the deepest desire of my heart. May our world be a place where this will never be the aspiration of any soul who is seeking the truth, a pure goal, or simply a fair place to live.

ACKNOWLEDGMENTS

I would like to thank my supervisor, Dr. Wei Guo, for his passion and his good heart. His care for his students like a second father, and his enthusiasm for science is heart-warming, and inspirational. I also thank all my labmates in Cryolab, colleagues at FCAAP, and the entire National High Magnetic Field Laboratory family who helped me in every stage of my PhD. This was truly never possible without you amazing people.

TABLE OF CONTENTS

List of Tables	viii
List of Figures	ix
I Experimental Work: Liquid Helium Turbulent Pipe Flow	1
1 Introduction	2
2 Superfluid Helium-4 Fundamentals	4
3 Introduction to the Law of the Wall in Fully-developed Turbulent Pipe Flow	8
3.1 Motivation: Near-wall velocity profile in high Reynolds superfluid helium pipe flow	11
4 Experimental Apparatus	13
4.1 Restoration and Upgrade of LHFVF	13
4.2 Description of Liquid Helium Flow Visualization Facility	14
4.2.1 Flow Pipe and Bottom Window Surface Condition	15
4.2.2 Cooldown Procedure for LHFVF	18
4.2.3 Implementation and Testing of the Flow Driving System	19
4.2.4 Generating Controlled High <i>Re</i> He II Flows in LHFVF	21
4.2.5 Measurement Time Window	22
4.2.6 Pressure Drop Measurements in LHFVF	22
5 Optical System and Measurement Procedures	25
5.1 Flow Visualization Technique in He II: Molecular Tagging Velocimetry	25
5.1.1 Metastable Helium Molecules	26
5.1.2 Cycling-transition Laser-induced Fluorescence	27
5.1.3 LHFVF Laser System for Creating Tracerlines using MTV	28
5.1.4 LHFVF Optical Design for Quantitative MTV	30
5.1.5 Preventing Breakdown Near the Solid Wall	33
5.2 Measurements in High-velocity He II Pipe Flows using MTV	35
5.2.1 Resolution of Our Flow Field Measurement Technique	36

6	Data Analysis	37
6.1	Obtaining NVP Data By Developing A Robust Image Processing Algorithm	37
6.1.1	Analysis of Background Images	39
6.1.2	Analysis of Tracerline Images	41
6.1.3	Obtaining the Mean Flow Velocity Field	43
6.1.4	Constructing the Mean Flow Velocity Profile	44
6.2	Friction Factor in He II pipe Flows	46
6.2.1	Classical and Non-classical Friction Factor Data	46
6.2.2	He II Friction Factor Correlation	48
6.2.3	Effects of the Non-circular Flow Pipe	48
6.3	Obtaining Law of the Wall in Superfluid Helium	50
6.3.1	Quantitative Determination of Law of the Wall Fitting Range	51
6.3.2	Law of the Wall Fitting Parameters in He II	52
6.4	Discussion	53
7	Results and Uncertainty Analysis	54
7.1	Uncertainty Analysis of the Law of the Wall in He II	54
7.1.1	Evaluation of the Uncertainties	55
7.1.2	Uncertainty in Location of Tracerline	56
7.1.3	Uncertainty of wall velocity profile and the logarithmic fitting	60
7.1.4	Fitting constants of the law of the wall in He II	62
7.1.5	Discussion	63
8	Summary and Future Work	64
II	Design Work: A magnetic levitation based low-gravity simulator	66
1	Introduction	67
2	Fundamentals of Magnetic Field Calculations	69
2.1	Magnetic Field Calculation	69
2.2	Potential Energy and Gradient Force Calculation	71
3	Magnetic Levitation-based Low-gravity Simulators	72
3.1	Levitation by a solenoid magnet	72

3.2	Concept and Performance of our MLS	73
3.3	A Practical Design for our MLS	76
3.3.1	Emulating Reduced Gravity in Extraterrestrial Environment	77
4	Summary and Future Work	79
III	Computational work: Transient Heat Transfer and Boiling in Superfluid Helium	80
1	Introduction	81
2	Fundamentals of Transient Heat Transfer in He II	82
3	Numerical Methods	85
4	Peak Heat Flux and Model Validation	89
5	Critical peak heat flux	92
5.1	Explanation and theoretical model of critical peak heat flux	93
6	Summary and Future Work	97
	Bibliography	98
	Biographical Sketch	114

LIST OF TABLES

6.1	Flow parameters and calculated log-law range based on classical relationships	51
-----	---	----

LIST OF FIGURES

2.1	a) Liquid helium-4 phase diagram. Below 2.17 K at saturated vapor pressure, classical liquid helium (He I) undergoes a phase transition and becomes superfluid (He II). b) The fraction of two fluids including the normal component (subscribed as n) and the superfluid component (subscribed as s) as a function of temperature. c) Kinematic viscosity of some common test fluids compared to that of liquid helium He I and He II.	4
2.2	a) A schematic showing an array of quantized vortices in a unit volume of He II and the mean vortex line spacing ℓ . b) Real photo of quantized vortices decorated with micron-scale solidified hydrogen particles [7].	5
2.3	a) Scattering of quasi-particles by a quantized vortex line resulting in a momentum exchange and a dissipative mechanism. b) A unit volume inside He II where interaction between the normal fluid and quantized vortices results in the non-classical force of mutual friction \mathbf{F}_{ns}	6
3.1	a) The overlap region laying between the viscous inner layer and the bulk fluid in the outer layer in turbulent wall-bounded flows. b) Scaling of the inner layer and the overlap region and their approximate range with respect to the wall in classical turbulent pipe flow. Beyond the overlap region, the scaling deviates from the logarithmic law. .	8
3.2	Experimental wall velocity profiles from Superpipe data for $Re_D = 31 \times 10^3$ up to $Re_D = 35 \times 10^6$ [30].	9
3.3	A schematic showing possible mismatch of the velocity profiles of the two fluids in the forced He II pipe flow.	11
4.1	A schematic of the Liquid Helium Flow Visualization Facility including the vacuum space, cryogenic vessels and fluids (blue), the flow pipe (green), optical ports (red), and mechanical equipment (black). LHe denotes liquid helium and LN ₂ denotes liquid nitrogen.	14
4.2	a) Bottom window glued to the flow pipe flange using the black stycast with no tolerance. The laser hole can be seen at the center of the window. b) Typical images in the microscopic imagery. The acrylic is decorated with paint for better optical focus during the measurements.	16
4.3	Velocity profile in wall coordinates in Wilkinson's experiments for a smooth non-porous flat plate $U = 21.3$ m/sec $u_\tau=0.819$ m/s (diamonds) and the perforated flat plate places on the walled honeycomb $U = 25.3$ m/sec $u_\tau=0.991$ m/s (circles) [52]. The dashed line shows the law of the wall for boundary layer flows from experimental data reviewed by Österlund <i>et al.</i> [31].	17
4.4	A schematic diagram of the precooling process of the flow pipe with cryogenic GHe (gaseous helium)	18

4.5	(a) A schematic diagram of the liquid helium pumping system where the bellows and the filling valves are depicted. E, N, and C subscripts stand for expanded, natural, and compressed, respectively, and L denotes length. $L_N = 4.88 \text{ in} \pm 15\%$ and allows 1 inch expansion and 3 inches compression. (b) A schematic diagram of the bellows geometry during contraction. (c) Normalized volumetric rate ratio as a function of normalized bellows top surface position for a full-stroke contraction. The time that the sequence of images take place are highlighted with red rectangles.	20
4.6	(a) Bellows displacement in He II analyzed as a function of time for a compression with a input control velocity of 5.08 mm/s (b) Five bellows motion runs in He II and their uncertainty (lays within the data points). It is clear that the variation between runs is negligible.	22
4.7	The flow pipe and the locations where the pressure drop is measured by using the DPT sensor. The optical view ports are shown for reference.	23
5.1	Cycling-transition laser-induced fluorescence for imaging metastable He_2^* molecules [73]. 0, 1, 2 denote the vibrational levels of the corresponding state. Color coded percentages show the amount of transited molecules.	28
5.2	Internal structure of the 905-nm imaging laser including the Nd:YAG 1064-nm laser cavity, second harmonic generator, and optical parametric oscillator (HWP stands for half wave plate).	29
5.3	(a) Secondary optical breadboard installed on top of the LHFVF view port#1. Lasers enters from the top window and imaging occurs through the side window. (b) The Schematic diagram of the system. The configuration can switch between single-line and double-line MTV using the beam splitter specified with the arrow. The reference laser can be merged to the beam path using a mirror for perpendicularity tuning. . .	31
5.4	(a) schematic diagram of the spatial and focal coincidence of the FS and IMG lasers to create a desired arbitrary Rayleigh range within the flow pipe. (b) A schematic showing a tracerline inside the flow pipe where the tracerline drifts with He II flow and then will be imaged. Flow field can be obtained by measuring the displacement of the drifted tracerline at any y location from the bottom wall. The average thickness of the beam in the Rayleigh range is typically about $80 \mu\text{m}$. (c) Test fluorescence images of the He_2^* tracerline generated in LHFVF He II flow pipe at 1.9 K (left:baseline, right: driftline). The width of the tracerlines is about $80 \mu\text{m}$ and the length is about 20 mm. 32	32
5.5	(a) Dielectric breakdown near the bottom wall and consequent molecular deposition in He II at 1.8 K inside the flow pipe (b) Complete elimination of the breakdown near the bottom wall by a precise tune of the FS-beam through the hole.	34
5.6	Schematic diagram of the configuration of the flow pipe and the lasers	34
5.7	The femtosecond, camera signal, and imaging laser pulses at 500 Hz. The green highlights depicts the camera exposure time which starts $1.5 \mu\text{s}$ before the IMG-beam radiation. When timed properly, all driftline profiles spatially collapse.	35

6.1	(a) Baseline image in still He II at 1.9 K 50 μ s after the creation. (b) Subsequent driftline image with $\delta t = 600 \mu$ s and 600 snapshot superimposition at FS-1 kHz when $U = 0.468$ m/s and $Re_D = 1.01 \times 10^6$	38
6.2	(a) A typical background image in He II at 1.9 K (b) Determination of the pixel size in the flow pipe by fitting horizontal lines to the light intensity one the bottom and the top windows	40
6.3	(a) Sweeping the entire frame of analysis in each binning bar parallel to the bottom solid boundary (b) The light intensity in binning bar at $y = 2.186$ mm as a function of streamwise pixel number, X , and the Gaussian functions fit to the intensity data at the first and second peak. The absolute maximum is denoted with \times and \times , respectively.	41
6.4	(a) A representative result of the image processing algorithm used to determine the baseline. (b) Determination of the subsequent driftline. (c) A schematic diagram showing the procedure for determining the mean velocity profile based on the drift distance and the drift time. Subscripts b and d denote baseline and driftline, respectively	42
6.5	(a) A representative mean velocity profile in He II at 1.9 K, where $U=0.468$ m/s and $Re_D = 1.01 \times 10^6$. The scaling of the near-wall region is clearly captured. The spatial resolution is 55 μ m. (b) The $U^*(\eta)$ velocity profile for recent experiments, both for the main and the second peak, and data from literature including Superpipe [46] and Hi-Reff [4]	45
6.6	The major body of friction factor data in literature in both classical and non-classical pipe flow [3, 4, 46, 89–91]. The Princeton-Oregon and Hi-Reff correlations are given. .	46
6.7	Friction factor data for non-classical pipe flow [90, 91] at similar conditions to those of our flow pipe. He II correlation fitted on the data using ODR with a similar format to that of the Prandtl global relationship.	47
6.8	Representative results for wall velocity u^+ as a function of dimensionless wall coordinate y^+ in He II at 1.9 K where $U=0.468$ m/s and $Re_D = 1.01 \times 10^6$. A strong logarithmic scaling exists from $y^+ = 330$ to $y^+ = 1800$ which shows a good agreement with the classical turbulence range. Least squares method is used for the fit to determine the von Kármán and additive constants. Superpipe [46] and Hi-Reff [4] classical data is shown for comparison.	50
6.9	Quantitative determination of the linear region using Φ function where the lower and upper limits of about $y^+ = 400$ and $y^+ = 2000$ are consistent throughout the experiments.	52
7.1	(a) Mean velocity PDF at $y = 0.49$ mm when involved parameters are perturbed within their error using a Monte-Carlo simulation with 10^4 perturbations. (b) Scanning the y location extending to 3 mm to acquire the velocity profile and associated uncertainty for a representative experiment where $U=0.468$ m/s and $Re_D = 1.01 \times 10^6$. The error calculated using derivations and the Monte-Carlo method are similar and can be compared at $y = 0.49$ mm as a representative.	58

7.2	(a) Scaling of the overlap region for a representative flow of $U = 0.468$ m/s and $Re_D = 1.01 \times 10^6$. Experimental data, the calculated error, and the linear fit to the experimental data are shown. (b) Monte-Carlo simulation of 1000 linear regressions within the log-law range from $y^+ = 330$ to $y^+ = 1800$, fit to the random data generated within the standard error of the wall velocity profile. The fits are achieved using least squares method. (c) 10 representative linear fits around the experimental data for a closer look at individual perturbations.	61
7.3	Representative PDF of (a) von Kármán constant and (b) additive constant as results of the 1000 fits to the perturbed wall velocity profiles as a result of the Monte-Carlo simulation. The means and the errors are shown.	61
7.4	Results of the law of the wall experiment in He II at 1.9 k and the overall error of the von Kármán constant for identical-condition experiments. Classical value is shown for comparison. (a) $U=0.47$ m/s and $Re_D = 1.01 \times 10^6$. (b) $U=0.56$ m/s and $Re_D = 1.21 \times 10^6$	62
7.5	Results of the law of the wall experiment in He II at 1.9 k and the overall error of the additive constant for identical-condition experiments. (a) $U=0.47$ m/s and $Re_D = 1.01 \times 10^6$. (b) $U=0.56$ m/s and $Re_D = 1.21 \times 10^6$	62
7.6	Elimination of the molecular deposition near the bottom wall using 500 Hz FS laser in a driftline image obtained with the superimposition of 500 snapshots in a test He II flow.	63
8.1	(a) Background Image at 1.8 K (b,c) Images showing two tracerlines created at different streamwise separation distances (d) Tunability of the vertical positions of the two tracerlines	65
2.1	(a) Schematic and dimensions of a gradient-field Maxwell coil with a diameter $D = 8$ cm. The origin of the coordinate system is at the center of the bottom Maxwell loop. (b) Schematic and dimensions of a solenoid magnet with a diameter of $D = 8$ cm and a height of $\sqrt{3}D/2$. The center of the solenoid is the coordinate system origin.	69
3.1	(a) Calculated specific potential energy $E(\mathbf{r})$ of a small water sample placed in the magnetic field. The turn-current NI of the solenoid is 607.5 kA. The origin of the coordinates is at the center of the solenoid. The dashed contour denotes the boundary of the trapping region, and the solid contour shows the low-force region. (b) The functional volume $V_{0.01g}$ (i.e., overlapping volume of the two contours) versus the turn-current NI . Representative shapes of the low-force region are shown.	73
3.2	Calculated specific potential energy $E(\mathbf{r})$ of a small water sample placed in the magnetic field for $I = 112.6$ kA and $B_0 = 24$ T. The origin of the coordinates is at the center of the bottom current loop. The black dashed contour denotes the boundary of the trapping region, and the black solid contour shows the low-force region (i.e., acceleration less than $0.01g$).	74

3.3	(a) Calculated $V_{0.01g}$ as a function of the coil current I for the Maxwell coil shown in Fig. 2.1(a) with $B_0 = 24$ T. The largest $V_{0.01g}$ is denoted as V_{peak} . (b) The optimal V_{peak} versus B_0 is shown. The absolute maximum of V_{peak} is showed as V_{max}	75
3.4	(a) Maximum functional volume V_{max} for the Maxwell coil as a function of diameters D . (b) The optimal I_{max} and $B_{0,\text{max}}$ in order to acquire the maximum volume are shown as a function of the coil diameter D	75
3.5	(a) Schematic of the practical MLS configuration composed of a 24-T outer superconducting magnet and four sets of inner gradient-field Maxwell coils. Coils are made of REBCO pancake rings. The bore of the superconducting magnet is 12 cm and the average diameter of the pancake rings is 8 cm, same as the ideal design. The origin of the coordinate system is at the center of the lowest pancake ring. (b) Computed contour map of the specific potential energy $E(\mathbf{r})$ for a small water sample inserted slightly above the center of the practical MLS while a total current-turn of $NI = 108.37$ kA is applied. The dashed contour depicts the magnetic trap whereas the solid contour shows the 0.01g force region. (c) Computed $V_{0.01g}$ as a function of the total current-turn, NI , at $B_0 = 24$ T. The maximum $V_{0.01g}$ is denoted as V_{peak} . (d) Peak functional volume, V_{peak} , is computed versus B_0 . The maximum V_{peak} is again achieved at $B_0=24$ T.	76
3.6	(a) Contour plot of calculated specific potential energy $E(\mathbf{r})$ of a water sample inserted in the practical MLS at $NI = 66.55$ kA and $B_0 = 24$ T. The black solid contours depicts functional volumes at 1% and 5% g_M , respectively. (b) The functional volume V_M in which the gravity varies within 5% of g_M as a function of the total current-turn NI . The optimal value is denoted as V_{peak} (c) The peak functional volume V_{peak} as a function of the base magnetic field B_0	78
2.1	In He II in the presence of a heat flux q , the normal fluid carries the heat away from the heat source with a velocity v_n whereas the superfluid moves in the opposite direction towards the heat source with a velocity v_s to satisfy the conservation of mass.	82
3.1	(a) A schematic diagram of the planar heater placed in a He II channel where the bath temperature is $T_B = 1.78$ K. A second sound generates and propagates downstream as a results of the applied heat flux. (b) Second sound propagation in space by time after applying a heat flux of $q_h = 30$ W/cm ² for a duration t_h . A temperature spike occurs at the heater surface as a result of the thermal layer development. (c) The spatial development of the thermal layer by time near the heater surface region where the temperature spike eventually reaches the saturation temperature.	87
4.1	(a) Evolution of the He II thermodynamics state at $x = \Delta x$ when heat pulses of $q = 30$ W/cm ² with different duration t_h are applied. The filled circles indicate the He II states at the end of the heat pulses. (b) The simulated curve showing the dependance of the peak heat flux q^* and the pulse duration t_h . The dashed line denotes that above a critical peak heat flux q_c^* (marked by the red diamond), the onset time of boiling suddenly drops to the order of $\Delta x/c_2$	90
4.2	Comparison of the simulated peak heat flux q^* and some relevant experimental data. The blue circles and squares are data obtained by Tsoi and Lutset at 1.794 K [190].	

The open and filled circles are data obtained by Shimazaki *et al.* at 2 K [189], where the open circles indicate possible onset of the boiling while the filled circles denote firm observation of the boiling. The purple and the green curves are our simulation at $T_b = 1.794$ K with $H = 1$ m and $T_b = 2$ K with $H = 0.3$ m, respectively. The purple band indicates the span of the curve when H is varied in the range of $0.8 - 1.5$ m, while the green band is for H in the range of $0.2 - 0.4$ m. 91

5.1 (a) Calculated q^*-t_h curves at various T_b with a fixed He II depth $H = 0.5$ m. The critical peak heat flux q_c^* for each curve is marked by the filled circle of the respective color. (b) The obtained critical peak heat flux q_c^* as a function of T_b . The black dots are simulation data. The solid and the dashed curves are calculated using Eq. (5.6) with and without the ΔP_1 term, respectively. 92

5.2 (a) Calculated q^*-t_h curves at various H with a fixed bath temperature $T_b = 1.78$ K. The critical peak heat flux q_c^* for each curve is marked by the filled circle of the respective color. (b) The obtained critical peak heat flux q_c^* as a function of H . The black dots are simulation data. The solid and the dashed curves are calculated using Eq. (5.6) with and without the ΔP_1 term, respectively. 93

5.3 (a) Evolution of the He II state at $x = \Delta x$ when heat pulses of different q_h are applied. The asterisk in each curve denotes the end state of the fast process, and the filled circle marks where the state curve reaches the saturation line. The inset shows the obtained correlation between q_c^* and t_h . (b) Time evolution of the He II pressure P , temperature T , and the vortex-line density L at $x = \Delta x$, 1 mm, and 2 mm for the case with $q_h = 50$ W/cm². All the simulations are conducted at $T_b = 1.78$ K and $H = 1$ m. 94

5.4 A schematic diagram showing the temperature and pressure changes as well as the motion of the two fluids in the first-sound and the second-sound pulse zones. 96

Part I

**Experimental Work:
Liquid Helium Turbulent Pipe Flow**

CHAPTER 1

INTRODUCTION

Liquid helium-4 undergoes a phase transition below about 2.17 K where it is called the superfluid (He II). He II is a non-classical fluid which is one of the very few macroscopic manifestation of the quantum mechanics. He II entails several bizarre properties including an extremely low kinematic viscosity. Due to this, He II has been proposed as an exceptional working fluid for turbulence research. The primary goal of the current thesis is to design a pioneering experiments to investigate the possibility and potential non-classical behavior of a law of the wall scaling in turbulent He II pipe flow. Here we report assembling a 5-m long He II flow facility so-called Liquid Helium Flow Visualization Facility which can generate He II turbulent flows with Reynolds numbers (Re) larger than a million. Inside an optically-accessible square flow pipe of $2 \times 2 \text{ cm}^2$ cross-section, we generate fully-turbulent He II forced flows using an automated bellows-linear actuator pump. We also report the incorporation of a quantitative flow visualization technique called molecular tagging velocimetry (MTV) using metastable triplet helium molecules as tracers. This visualization technique is based on a combination of a femtosecond laser-field ionization together with a 905-nm laser-induced fluorescence scheme to generate and illuminate the metastable helium molecules, respectively. We have designed and implemented a novel optical system to guide and satisfy the optical criteria for visualization of He II. Using this one-of-a-kind facility, we report the first quantitative flow visualization study of the law of the wall in He II turbulent pipe flow. We acquire the mean velocity profile near the wall region using a robust image processing algorithm, specifically developed for the type of images we acquire in our flow pipe and we compare it with the existing data in classical fluid research. Our data shows the existence of a logarithmic profile of “the near-wall mean velocity profile in turbulent pipe flow (NVP) in He II”. By fitting the velocity profile using the law of the wall formula, we determined the two fitting coefficients including the von Kármán coefficient κ and the additive constant B in He II. We also conducted a comprehensive uncertainty analysis of data to evaluate the associated error. It turns out $\kappa = 0.160 \pm 0.015$ and $\kappa = 0.154 \pm 0.010$, and $B = -23.2 \pm 0.4$ and $B = -24.0 \pm 0.4$ for $Re_D = 1.01 \times 10^6$ and $Re_D = 1.21 \times 10^6$, respectively. On the other hand, the values of these two constants in classical turbulent pipe flow are determined about $\kappa = (0.37 - 0.42)$ and $B = (4 - 6)$. This significant difference suggests that the non-classical

properties of He II affects the velocity profile in extremely high Re He II pipe flow. This deviation from classical turbulence is of great significance for future numerical research as well as engineering designs of the He II pipe systems. The essential contents in Chapter 2-5 are peer reviewed and published in [1].

CHAPTER 2

SUPERFLUID HELIUM-4 FUNDAMENTALS

Cryogenic helium-4 provides distinctive advantages in thermal engineering applications and in fluid dynamics research due to its unique thermal and mechanical properties. Ordinary liquid helium (He I) exists at 4.2 K and atmospheric vapor pressure. As shown in Fig. 2.1 (a), when He I is cooled (e.g., evaporative cooling) below a transition point $T_\lambda = 2.17$ K, liquid helium undergoes a phase transition from a classical fluid to a non-classical quantum fluid (He II). This non-classical state of liquid helium can be regarded as a two-fluid system which consists of a normal fluid component (a collation of thermal excitations or quasi-particles) and a superfluid component (a collection of atoms in quantum mechanical ground state) [2]. The normal component behaves more like a classical fluid and has viscosity and entropy. on the other hand, the superfluid component is a quantum fluid which is inviscid and carries no entropy. As shown in Fig. 2.1 (b), the fractions of these two components depend on the temperature. The relative density of the superfluid (normalized by the total density) starts from zero above the transition point and increases to about 1 at below 0.5 K. The two-fluid system is characterized with some extremely bizarre properties. For example, the kinematic viscosity ν of He II can be smaller than 10^{-8} m²/s, which is lower than any other known substance and usually orders of magnitude smaller than that of ordinary fluids as shown in Fig. 2.1 (c). This is particularly useful for so-called high Re flow research. Reynolds number

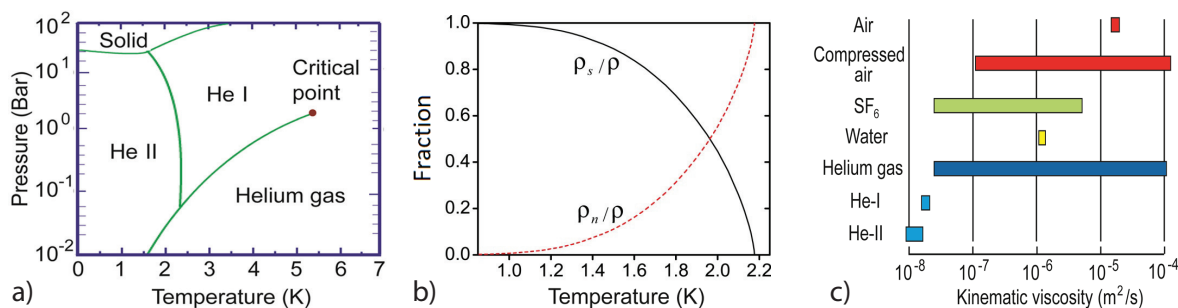


Fig. 2.1: a) Liquid helium-4 phase diagram. Below 2.17 K at saturated vapor pressure, classical liquid helium (He I) undergoes a phase transition and becomes superfluid (He II). b) The fraction of two fluids including the normal component (subscribed as n) and the superfluid component (subscribed as s) as a function of temperature. c) Kinematic viscosity of some common test fluids compared to that of liquid helium He I and He II.

is defined as $Re = DU/\nu$, where U and D stand for the characteristic velocity and length scale, respectively. So we can see when the kinematic viscosity is small such as in He II, one can generate flows with extremely high Re using relatively small-size and low-speed flow facilities. For example, liquid helium flow facilities [3] were shown capable of generating the same magnitude Re flows in far smaller-size facilities [4]. A high Re liquid helium flow facility only needs flow velocity as low as 0.5 - 5 m/s [1, 5] which makes the pumping system less complex without introducing compressibility effects in opposite to high-speed facilities such as wind tunnels [6].

In this research, we will particularly focus on turbulent pipe flow. Due to the omnipresent and simple applications, turbulent pipe flow has been excessively subject to experimental and numerical studies in the past 100 years, however, there is still a large body of ongoing studies and unresolved problems regarding this long-lasting research topic. For example, over the past 2 decades, the state-of-the-art Superpipe at Princeton uses high pressure air up to 220 bars as the working fluid to achieve a low kinematic viscosity [8]. Apart from manufacturing and safety complexities, such high pressures make it very challenging to incorporate optical accesses in the body of a facility for visualization measurements of the flow field. On the other hand, compact liquid helium cryostats have been already built for optical flow visualization of high Re flows [1, 9]. Furthermore, some of the published results [10] are in slight contrast with the Superpipe results, which cast doubt on the universality and Re dependence of the fitting coefficient of the NVP. These discrepancies obviously call for more systematic studies, especially direct visualization measurements, which are possible using liquid helium flow facilities.

In addition to the smallest kinematic viscosity, helium is also known for its fascinating quantum hydrodynamics in the superfluid phase. For instance, rotational motion in the superfluid can occur

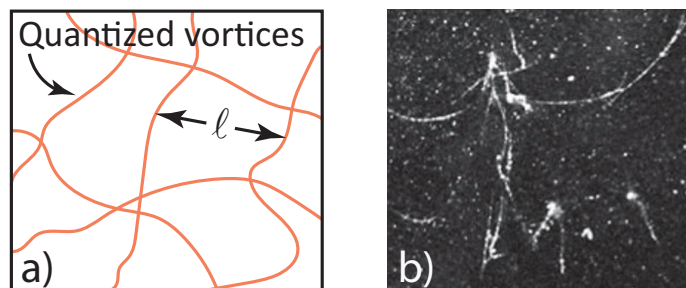


Fig. 2.2: a) A schematic showing an array of quantized vortices in a unit volume of He II and the mean vortex line spacing ℓ . b) Real photo of quantized vortices decorated with micron-scale solidified hydrogen particles [7].

only with the formation of topological defects in the form of quantized vortex lines [11]. These vortex lines all have identical cores (about 1 Å in radius), and they each carry a single quantum of circulation $\Gamma \simeq 10^{-3} \text{ cm}^2/\text{s}$. Turbulence in the superfluid therefore takes the form of an irregular tangle of vortex lines (quantum turbulence). The vortex lines can be nucleated, decay or reconnect inside He II which leads to a dynamic and time variant behavior. One can define the vortex line density L as the vortex line length per unit volume of fluid which is related to the mean vortex line spacing ℓ via $\ell \sim L^{-1/2}$ as shown in Fig. 2.2 (a). Fig. 2.2 (b) shows a real photo of quantized vortices decorated with micron-sized solidified hydrogen particles obtained at the University of Maryland [7].

In the two-fluid system, quasi-particles can have interaction with the quantized vortices as shown in Fig. 2.3 (a). Quasi-particles will scatter off the vortex lines and exchange momentum with them, depending on their velocity and the dynamics of the quantized vortices. This interaction and momentum exchange results in a dissipative mechanism. This mechanism is the origin of a non-classical force so-called the mutual friction \mathbf{F}_{ns} [12] as shown in Fig. 2.1 (b). The mutual friction acts as a viscous-like drag between the normal fluid component containing the quasi-particles and the superfluid component with vortices. In practice, when there is a relative motion between the two fluids, it results in arising the mutual friction. Mutual friction can affect the flow in both fluids and significantly alter the turbulence characteristics of He II in various flows.

Despite the advantages of cryogenic helium, it must be noted that conventional flow treatments, measurements, and visualization techniques cannot be incorporated in a cryogenic environment [13]. Flows visualization in cryogenic helium is very challenging, largely due to the extremely low tem-

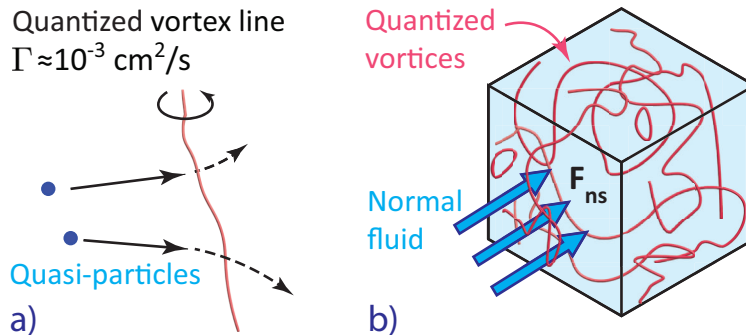


Fig. 2.3: a) Scattering of quasi-particles by a quantized vortex line resulting in a momentum exchange and a dissipative mechanism. b) A unit volume inside He II where interaction between the normal fluid and quantized vortices results in the non-classical force of mutual friction \mathbf{F}_{ns} .

perature and low density of helium [14]. In the past, particle tracking velocimetry and particle image velocimetry (PIV) were developed where micron-sized frozen hydrogen particles are used as tracers in He II [5, 7, 15–18]. These tracer particles are injected into liquid helium as a mixture of hydrogen and helium gases, however, this introduces a huge heat load into the system and the induced boiling strongly disturbs the flow field under the study. Moreover, the tracers produced in these methods are in a wide range of sizes and irregular shapes, and they are not neutrally buoyant which is not desirable in flow measurements. Furthermore, it is known that the micron-sized tracers can interact with both the normal fluid and the quantized vortices, complicating the analysis of their motion [19]. For all these reasons, a powerful visualization technique designed to work in cryogenic helium known as Molecular Tagging Velocimetry has been developed in our lab [20] which will be explained upon in Chapter 5. This technique has been successfully used in the past for different types of flow measurements in superfluid liquid helium [21–27] and is utilized in this research as well.

CHAPTER 3

INTRODUCTION TO THE LAW OF THE WALL IN FULLY-DEVELOPED TURBULENT PIPE FLOW

Fully-developed pipe flow is a state in which the flow is no longer under the influence of the entrance. As a consequence, all the flow properties become independent of the streamwise axis. For such fully-developed flow in a smooth pipe when the surface roughness is sufficiently small, the mean velocity profile in the pipe would be only a function of Re [28]. For such a pipe flow, the mean velocity profile established near the wall can be non-dimensionalized using a set of appropriate properties. This dimensionless profile is called the wall velocity profile. It can be shown that when Re is sufficiently large, the wall velocity profile might become universal for wall-bounded fully-developed turbulent flows. In different regions of the pipe with respect to the distance from the wall y , there exists different velocity scalings. A thin layer adjacent to the wall is called the inner layer and is strongly viscous-dominant. The bulk region far from the wall is called the outer layer. There exist a so-called overlap region between these two layers where the scaling of the wall velocity profile is governed by a logarithmic relationship. This physical picture is schematically shown in Fig. 3.1

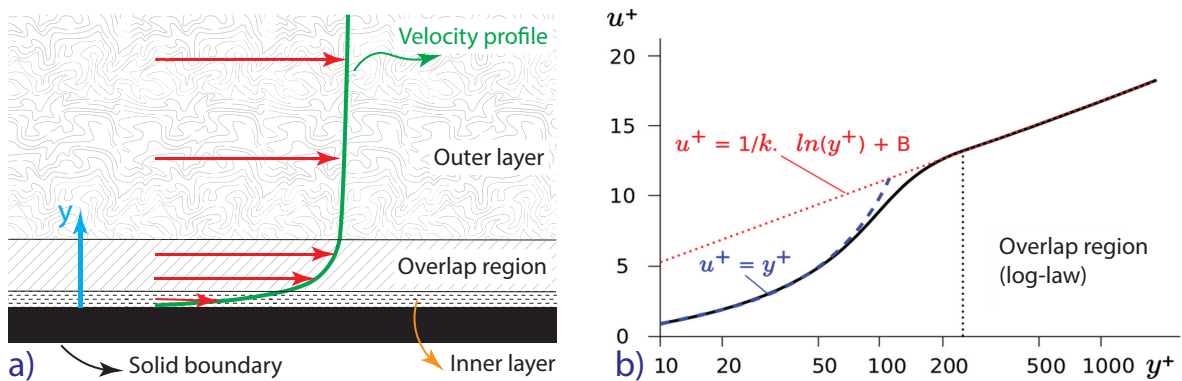


Fig. 3.1: a) The overlap region laying between the viscous inner layer and the bulk fluid in the outer layer in turbulent wall-bounded flows. b) Scaling of the inner layer and the overlap region and their approximate range with respect to the wall in classical turbulent pipe flow. Beyond the overlap region, the scaling deviates from the logarithmic law.

(a). This logarithmic scaling, known as the law of the wall (the log-law), is given by:

$$u^+ = \frac{1}{\kappa} \ln(y^+) + B, \quad (3.1)$$

where $u^+ = \bar{u}/u_\tau$, $y^+ = yu_\tau/\nu$, \bar{u} is the mean flow velocity, κ is von Kármán constant and B is the additive constant which depends on the inner limit of the integration of the log-law. $\nu = \mu/\rho$ is the kinematic viscosity where μ is the viscosity and ρ is the fluid density. Friction velocity is defined as:

$$u_\tau = \sqrt{\tau_w/\rho} = U \sqrt{\frac{f_D}{8}}, \quad (3.2)$$

where τ_w is the wall shear stress, U is mean velocity averaged over the pipe cross-section, and f_D is the friction factor. Friction factor is a flow property related to the friction losses. It can be either calculated using the existing correlations or directly determined via measuring the pressure drop ΔP using $f_D = 2\Delta P \cdot D_h/(L_f \cdot \rho U^2)$ where D_h is the hydraulic diameter and L_f is the pipe length [29]. The scaling of the viscous sublayer in the inner layer (the linear region) and the overlap region (the log-law) and their approximate distance from the wall in the classical turbulent pipe flow is schematically shown in Fig. 3.1 (b).

There have been extensive experimental [4, 28, 31–33] and numerical [34–36] studies of the law of the wall in wall-bounded turbulent flows. For instance, in the Superpipe experiment, the researchers measured the velocity profile using the hot-wire velocimetry and first observed the log-law in a region between $y^+ = 100$ and $y/R = 0.2$ when $Re_D > 4.0 \times 10^5$. They derived

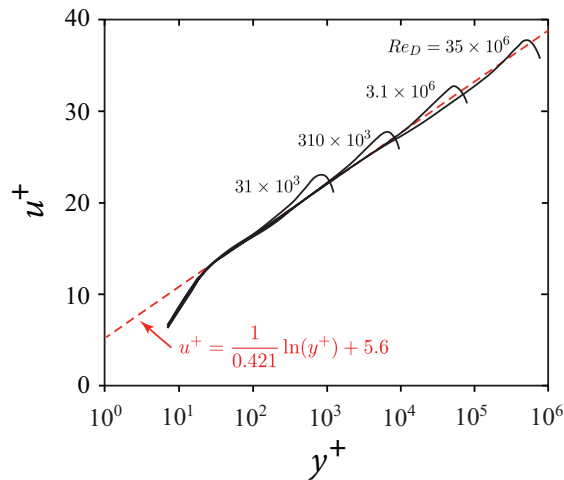


Fig. 3.2: Experimental wall velocity profiles from Superpipe data for $Re_D = 31 \times 10^3$ up to $Re_D = 35 \times 10^6$ [30].

the universal constants as $\kappa = 0.41$ and $B = 5.2$ [28]. Later, they updated their results after a more careful data collection and analysis. They proposed that the log-law exists in the range of $600 < y^+ < 0.07Re_\tau$ where the constants are $\kappa = 0.436$ and $B = 6.15$. More recently, they improved the measurement quality and published the results. They stated that the log-law exists between $600 < y^+ < 0.12Re_\tau$ for $Re_D > 2.3 \times 10^5$ where the updated constants are $\kappa = 0.421$ and $B = 5.6$ [30] as shown in Fig. 3.2. On the other hand, the data produced by Japan HI-Reff via measuring the velocity profile using laser Doppler velocimetry proposes that the log-law region exists for $y^+ > 400$ when $Re_D > 3.9 \times 10^5$. They derive the constants equal to $\kappa = 0.382$ and $B = 4.4$ [4]. They also use the pressure drop measurements to calculate the constants based on the Prandtl friction factor equation. The results are in good agreement with the velocity profile results and suggest $\kappa = (0.390, 0.385)$ and $B = (5.0, 4.7)$ for two different pipe diameter when $1.2 \times 10^4 < Re_D < 1.8 \times 10^7$ and $3.0 \times 10^5 < Re_D < 1.0 \times 10^7$, respectively [4]. Later they improved the measurement quality [10] and published the results. They stated that the log-law region exists between $3\sqrt{Re_\tau} < y^+ < 0.2Re_\tau$ when $1.0 \times 10^3 < Re_\tau < 5.3 \times 10^4$ where κ asymptotically approaches a constant value of $\kappa = 0.384$ and $B = (4, 4.8)$ for two pipes of experiments with an average value of $B = 4.53$. In the experiments conducted by other researchers, other values such as $\kappa = 0.383$ from data of CICLoPE facility [32], and $\kappa = (0.384, 0.386)$ by Monty [33] have been reported.

On the numerical side, Wu and Moin [34] conducted direct numerical simulations (DNS). In a review paper, Nagib and Chauhan [37] analyze their data and estimate $\kappa = 0.384$. In other DNS studies of infinite channel flow, $\kappa = 0.384$ [35] and $\kappa = 0.387$ [36] were reported. Also on the theoretical side, it has been shown that law of the wall in wall-bounded turbulence is indeed a valid outcome of the Navier-Stokes equation using a symmetry invariant solution for infinite set of moment equations [38].

In conclusion, there are several experimental and numerical studies suggesting $\kappa = 0.38 - 0.39$. This is why κ might be regarded as a universal constant for canonical wall-bounded turbulent flows at sufficiently large Re . However, the data from Superpipe experiments over 2 decades suggests $\kappa = 0.42$ and casts a shadow over this universality. A review paper in 2012 stated that there is no consensus regarding the universality of the law of the wall [39].

3.1 Motivation: Near-wall velocity profile in high Reynolds superfluid helium pipe flow

In mechanically-driven He II flows, there are both experimental [40] and numerical [40] studies showing that the two fluids can be strongly coupled by mutual friction and behave like a single fluid. In this case, the flow can exhibit classical features. This is why this type of flow is sometimes called quasi-classical flow or co-flow. The mutual friction tend to eliminate the velocity difference between the two fluids. However, when the length scales becomes comparable or smaller than the mean vortex line spacing ℓ , the superfluid velocity would be controlled by individual quantized vortices whereas in the normal fluid the velocity field is smooth since there are no quantized vortices. As a consequence, the velocity field of the two fluid can no longer couple. Therefore, a strong dissipation mechanism occurs which is due to the mutual friction [41]. This physical picture raises a possibility to exploit the low kinematic viscosity of He II for classical turbulent research. However, all the previous studies were conducted in relatively low Re and a low velocity gradient region. So a natural question is whether the two fluids still remain fully-coupled in the most extreme case of a very high Reynolds number pipe flow when the velocity profile near the wall can become highly gradient.

In He II pipe flows, the two fluids can become coupled in the bulk liquid at scales greater than the mean vortex-line spacing [42]. However, the situation may change near the pipe wall. Due to the no-slip boundary condition of the viscous normal fluid, there is a strong velocity gradient in a very thin boundary layer. There is no guarantee that the mutual friction could be effective enough to maintain a similar velocity gradient in the superfluid. A no-slip velocity boundary layer

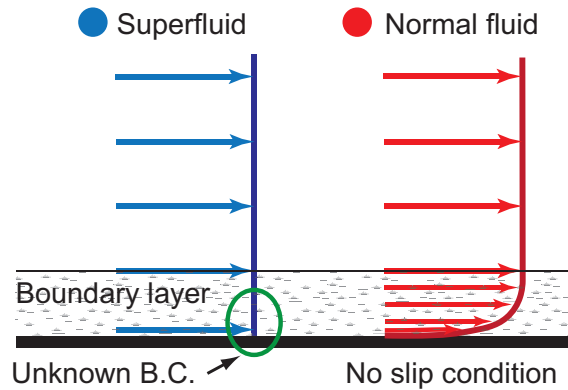


Fig. 3.3: A schematic showing possible mismatch of the velocity profiles of the two fluids in the forced He II pipe flow.

in the superfluid would require a highly nonuniform distribution of the quantized vortices [43]. These vortices also need to polarize parallel to the wall and perpendicular to the flow direction. However, there is no existing knowledge whether such configuration of vortices can be achieved and maintained. If this were indeed not possible, then the two fluids could have mismatched velocity profiles in the narrow region near the wall which is schematically shown in Fig. 3.3. Therefore, the relative velocity in the boundary layer leads to a mutual friction per unit volume between the two fluids that affects the classical logarithmic velocity profile of the normal fluid. Measuring the possible revised law-of-the-wall in the normal fluid will enrich our knowledge of boundary layer flows. Moreover, it will also benefit various He II pipe-flow based applications.

Despite the evident importance of such measurements, there is no existing knowledge about such physics due to its great complexity. On one hand, DNS studies of high Re pipe flow in He II are impractical at the current stage. He II is a two-fluid system. The normal fluid is governed by the Navier-Stokes equation but numerical simulations of classical high Re pipe flow is already a very challenging problem. But adding the Biot-Savart equations of the superfluid complicates the situation even further. The simulation of the quantized vortices and the superfluid hydrodynamics with very high vortex line density is very difficult. Therefore, numerical investigations of the two-fluid system in the high Re pipe flow is currently impossible due to extempore high computational expenses. This is why an emergent need for experimental studies designed to tackle such physics becomes evident. On the experimental side, there is a very limited experimental measurement in He II turbulent pipe flow using PIV [44]. But more importantly, this measurement does not have the required resolution to capture the NVP. Therefore, the need for designing a unique experimental setup and a novel measurement procedure capable of resolving the fine region near the wall in turbulent pipe flow in He II was our greatest motivation.

Considering the countless applications of turbulent He II transfer pipes in magnet and aerospace engineering, healthcare industry, and fundamental physics research, a first high resolution flow visualization and study of the boundary layer in extremely high Re He II pipe flows appears of great significance. The primary goal of the current thesis is to design a pioneering experiment to investigate the possibility of a law of the wall scaling in turbulent He II pipe flow.

CHAPTER 4

EXPERIMENTAL APPARATUS

The Liquid Helium Flow Visualization Facility (LHFVF) is a cryostat designed for generating and visualizing liquid helium pipe flows. LHFVF is schematically shown in Fig. 4.1. In the past, this cryostat was used by Dr. Van Sciver and his students [44, 45]. However, the cryostat had a major incident in 2013 due to overpressurizing the two bellows pumps. This incident resulted in a severe damage of the internal components, especially the bellows pumps. Following the incident, the cryostat was not used for 6 years. As a results, there was no documentation about its structure and operational procedures.

4.1 Restoration and Upgrade of LHFVF

In 2019, we started systematic repairs and modifications in order to fully restore and upgrade the facility for the newly designed turbulent pipe flow experiments in He II. This repair process included troubleshooting, repairing, designing new systems and parts, implementing, testing, repeating and finally optimizing parts and functions of LHFVF systems. In November 2021, this extensive effort successfully restored and upgraded the cryostat for the desired pipe flow experiments. The major improvements include the following:

1. Obtained a significant decrease in the boil-off rate of liquid helium by a factor of about 8 and a corresponding increase in operational time from 4 hours to 16 hours. This was achieved by repairing the vacuum space leak, improving the multi-layer insulations (MLI), and mitigating internal solid contact heat leaks.
2. Developed a fully automated system for monitoring the temperatures and pressures, and controlling the fluid motion, the image acquisition, and the motor motion.
3. Developed an optical system for implementing the MTV technique to this facility. The details will be explained upon in Sec. 5.1.4
4. Developed an effective gas handling system for reliable operation of the vacuum space, experimental gases and fluids, purge gases, thermal shield fluids, etc.
5. Optimized and implemented a bellows pump control system for driving the fluid inside the pipe

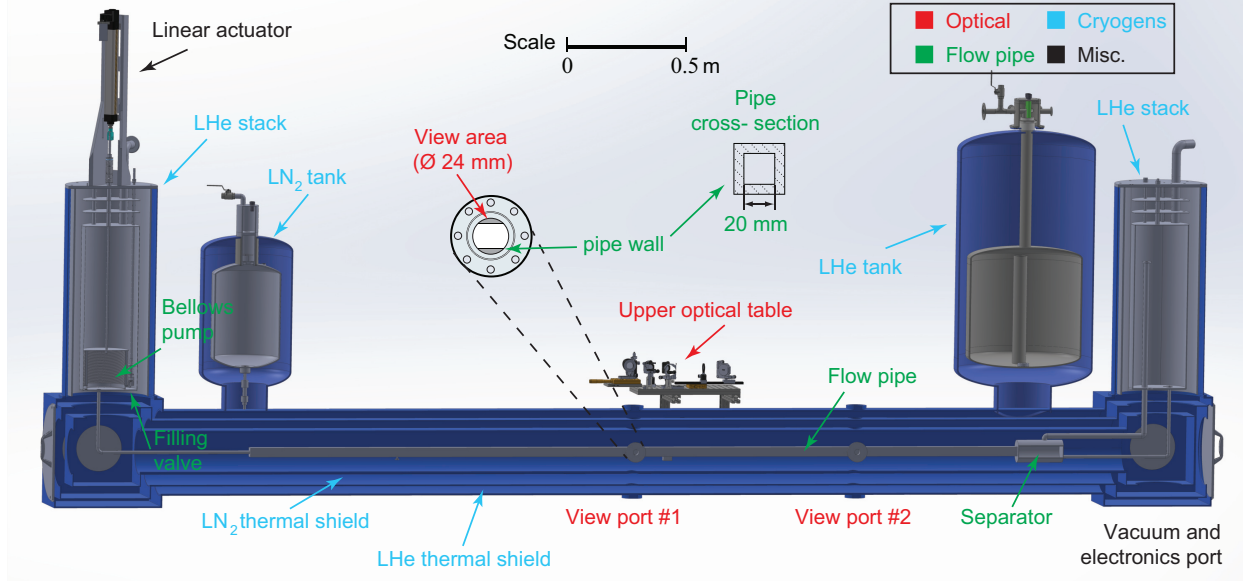


Fig. 4.1: A schematic of the Liquid Helium Flow Visualization Facility including the vacuum space, cryogenic vessels and fluids (blue), the flow pipe (green), optical ports (red), and mechanical equipment (black). LHe denotes liquid helium and LN₂ denotes liquid nitrogen.

6. Developed a timing control of the laser systems so we can accurately create and image the tracerlines after a desired drift time. The details will be explained upon in Sec. 5.1.3
7. Numerous other modifications/optimizations of the parts and systems, including the helium thermal shield, the flow pipe, the turbo-molecular pumps, differential pressure transducer carrier demodulator, and the laser systems internal configuration including the Femto-second laser system and the 905-nm laser.

4.2 Description of Liquid Helium Flow Visualization Facility

LHFVF has a cylindrical experimental space with an inner diameter of 0.2 m and the length of 4.5 m. The experimental space is protected by two concentric thermal radiation shields. These shields are cooled by natural convection loops from the liquid helium and the liquid nitrogen tanks as shown schematically in Fig. 4.1. These shields are wrapped with MLI and housed inside the evacuated cryostat body. A turbo-molecular pump and a diffusion pump are used to evacuated the cryostat vacuum space to below 10^{-3} Pa. The flow pipe is a 3.35 m long pipe with a square 2×2 cm² cross-sections that sits at the center of the experimental space. The distance from the pipe entrance to the visualization optical port is 100 times greater than the hydraulic diameter of the flow pipe $D_h=2$ cm. This distance is much larger than the turbulence development length

which is typically around $25 - 40D_h$ [44]. Therefore, our He II flows would be free of entrance effects. The flow pipe is welded with a special technique to ensure the equal thickness of welding faces to minimize the welding distortion. The flow pipe is connected to two vertical helium storage stacks at the two ends of the LHFVF which are protected with separate liquid nitrogen jackets and MLIs. Flow visualization in LHFVF can be made through two sets of optical ports, one at the midpoint and the other about 1 m downstream. Each optical port consists of 3 windows on the top, the bottom, and the side on each shield and the flow pipe. These windows have optimal clearance area to minimize radiative heating. The side window of the pipe has a diameter of 24 mm which is larger than the inner width of the flow pipe for full optical access (see the view area in Fig. 4.1). This design allows the study of the boundary layer flow in the vicinity of the solid walls. In the experiments, the laser beams go through the top and bottom windows. An intensified charge-coupled device (ICCD) camera (ANDOR Oxford Instrument iStar) is placed in front of the side window for image acquisition. The temperature is measured using Cernox thermometers placed at multiple locations inside LHFVF. Baratron capacitance manometers are used to read the pressure in each stacks whereas the vacuum space pressure is accurately measured using a thermal contact and a cold cathode pressure sensor. The temperature of the liquid helium in the stacks can be controlled by regulating the vapor pressure.

4.2.1 Flow Pipe and Bottom Window Surface Condition

There are numerous experimental and numerical studies on the effect of the surface roughness of a flow passage on the flow, in particular, the turbulent pipe flow [46–50]. A natural question is what pipe surface condition is considered smooth. The relative roughness $e = k/D_h$ is sometimes used to evaluate the smoothness of a pipe where k is the roughness height and is usually taken as the root-mean-square roughness height k_{rms} [47]. Nikuradse [48] showed that the wall roughness defined as $k_s^+ = k_s u_\tau / \nu$ can be used to better evaluate the smoothness of the pipe wall where k_s is the equivalent sandgrain roughness height and ν/u_τ is the wall unit. He showed nondimensionalizing the roughness using the wall unit is preferred because the roughness is compared to a more relevant length scale rather than the hydraulic diameter. He found that the flow can be considered smooth for $k_s^+ \leq 5$, transitionally rough for $5 \leq k_s^+ \leq 70$, and fully rough for $k_s^+ \geq 70$. In another study, based on the Superpipe experimental data, Zagarola and Smits [46] suggested that the equivalent sandgrain roughness height can be taken as $k_s \simeq 3k_{rms}$. In other research works, the effect of surface roughness and porosity on the law of the wall has been subject to extensive experimental

and numerical studies [47, 49, 50]. These studies clearly show that the surface roughness and even porosity only affect the intercept of the log law B , and do not affect the slope of the log law κ .

With this background, we can quantitatively evaluate the surface condition of our flow pipe, and particularly, around the bottom window. The root-mean-square roughness height of our flow pipe is about 2 micro-inch ($0.051\mu\text{m}$) for polished stainless steel. In our typical experiments, we show in chapter 6 that the wall unit is about $0.5\mu\text{m}$. This results in a wall roughness $k_s^+ = 0.3 \ll 5$ which is far smaller than the transition value i.e., five. This clearly shows that our flow pipe is smooth. The flow measurements in our experiments are taken above the bottom window, thus the surface condition of this window is important. The bottom window is made of acrylic which is far smoother than stainless steel. We used an epoxy called stycast to mount the bottom wall to the pipe flow flange. This mounting method was performed manually, therefore, the acrylic surface will not be perfectly flush with the flange. If this step is too large, it can introduce unwanted disturbance in the flow to be studied. The downstream edge of the acrylic is far from the tracerline. We used an all-automated Nikon microscope camera (iNEXIV VMA-2520) with 120x magnification and a measurement resolution of $0.1\mu\text{m}$ to measure the step size of our window. Two images taken by this microscope are shown in Fig. 4.2. For three measurements from different angles of the window performed by an expert operator, we obtain the step size $30 \pm 1\mu\text{m}$ which is roughly 3% of the upper height of the log law region in our typical pipe flows. Depending on the ratio of a step size to the boundary layer thickness, Awasthi *et al.* [51] showed that the disturbances created at the edge of a forward step affect the downstream flow over a distance 2-4 times larger than the height of the step in turbulent boundary layer flows. Therefore, we expect the disturbances created due

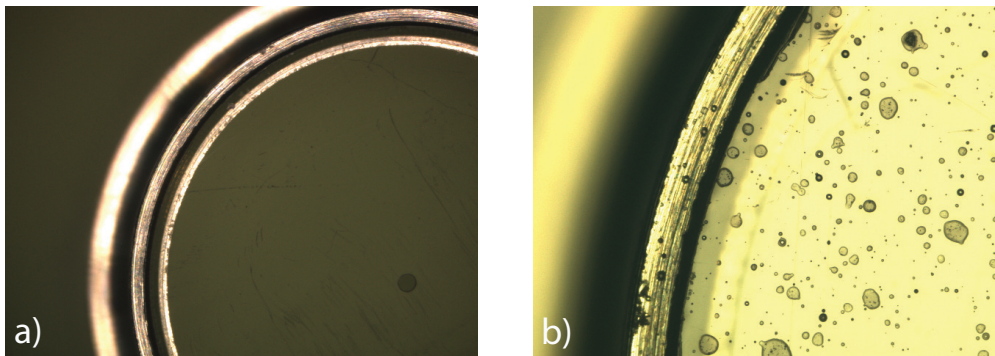


Fig. 4.2: a) Bottom window glued to the flow pipe flange using the black stycast with no tolerance. The laser hole can be seen at the center of the window. b) Typical images in the microscopic imagery. The acrylic is decorated with paint for better optical focus during the measurements.

to the upstream edge of the bottom window only affect about $100 \mu\text{m}$ of the downstream which is much smaller than the distance from the edge of the window to our measurements (8 mm).

To pass the FS laser beam through the acrylic without burning it or causing dielectric breakdown of liquid helium [20], we drilled a precise hole in the center of the acrylic with a radius of $250 \mu\text{m}$. In the experiments, the size of the FS beam is about $80 \mu\text{m}$. Using a beam profile camera, we tune the FS-beam closer to the upstream edge of the hole. As a consequence, the drifted tracerline is never farther than $200 \mu\text{m}$ from this edge regardless of the flow velocity. This distance is 400 wall units. Wilkinson [52] conducted experiments to study the effect of a perforated flat boundary on the law of the wall using air as the working fluid. Underneath the perforated surface, he used a honeycomb structure to mitigate the flow circulations. The honeycomb was placed on an impervious surface which bonded the flow. The diameter of the holes in his setup is $1680 \mu\text{m}$ which is about 110 wall units. This hole geometry is similar to the one in the bottom window in our experiment. Wilkinson showed that the effect of such porous boundary on the law of the wall is quite small. His experimental results are shown in Fig. 4.3. Since the size of our laser hole in the wall unit is comparable to that in Wilkinson’s experiments, the hole in the bottom window should not have a significant effect on our results.

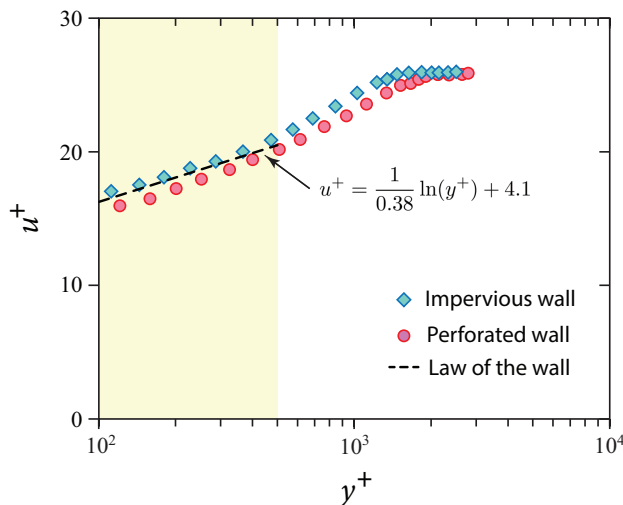


Fig. 4.3: Velocity profile in wall coordinates in Wilkinson’s experiments for a smooth non-porous flat plate $U = 21.3 \text{ m/sec}$ $u_\tau=0.819 \text{ m/s}$ (diamonds) and the perforated flat plate places on the walled honeycomb $U = 25.3 \text{ m/sec}$ $u_\tau=0.991 \text{ m/s}$ (circles) [52]. The dashed line shows the law of the wall for boundary layer flows from experimental data reviewed by Österlund *et al.* [31].

4.2.2 Cooldown Procedure for LHFVF

We have developed an effective cooldown procedure that minimizes the usage of liquid helium. First, we cool the nitrogen and helium radiation shields and nitrogen jackets by introducing liquid nitrogen. The thermal conduction from these components to the flow pipe cools down the pipe to about 160 K in 4 days. Second, we directly cool down the flow pipe using liquid nitrogen. Next, the liquid nitrogen is purged and pumped out. It is crucial to make sure liquid nitrogen no longer exists in the pipe before the pumping process. It is important to keep the vacuum pressure above 20 kPa during the first pumping cycle to ensure the triple point of liquid nitrogen will not be reached. Therefore, nitrogen does not freeze inside the flow pipe. By the end of this stage, the pipe temperature can reach as low as 90 K. This procedure allows us to minimize the liquid helium consumption by removing most of the thermal energy from the pipe using the inexpensive liquid nitrogen. At this stage, the stacks and the flow pipe are ready to be further cooled down using cold helium vapor from a liquid helium storage Dewar. Practically, what we find most effective is to flow the helium vapor from one stack through the flow pipe to the other stack. This process is schematically shown in Fig. 4.4. When the temperature of the stacks and flow pipe system falls below 15 K, we then transfer liquid helium to the right stack while its level can be monitored via a superconducting helium level meter (24 inches). The liquid helium spontaneously flow from the right stack through the pipe to the left stack. After both stacks are fully filled, we remove the liquid helium fill line and start pumping on the stacks. As the vapor pressure drops around 4.8

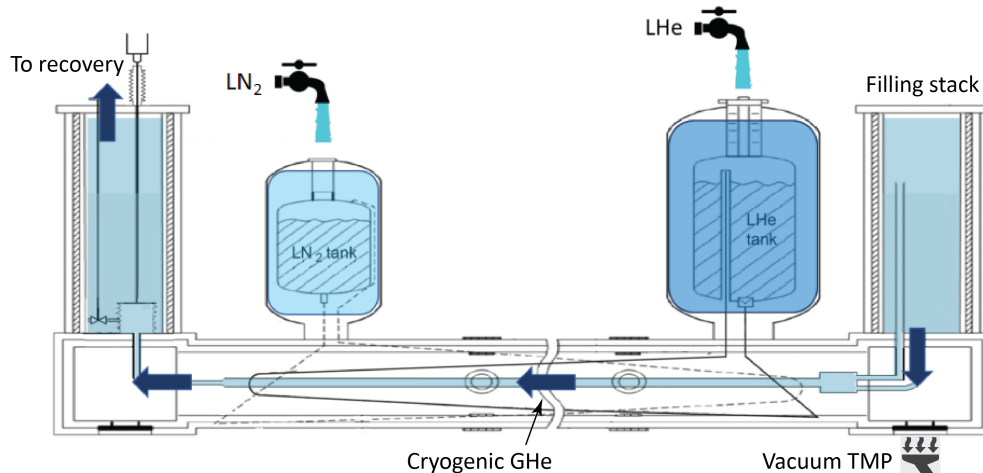


Fig. 4.4: A schematic diagram of the precooling process of the flow pipe with cryogenic GHe (gaseous helium)

kPa, the liquid helium undergoes the lambda transition and enters the superfluid phase. We have tested this cooldown procedure and proved that it is safe, efficient, and with a minimum liquid helium consumption. In a typical run, we have tested that only 160 liters liquid helium is needed. For each transfer, the cryostat can be kept cold for about 16 hours.

Due to the high cost of liquid helium, currently liquid nitrogen is used for cooling the helium radiation shield. Note that the radiative heating power from the helium shield to the flow pipe is calculated by:

$$\dot{q} = \sigma \epsilon F_{12} A T_{shield}^4 \quad (4.1)$$

where σ is Stefan-Boltzmann constant, ϵ is emissivity and is about 0.2 for clean polished stainless steel at 2 K [53], $F_{12} \simeq 1$ is the corresponding view factor, and $A \simeq 0.3 \text{ m}^2$ is the surface area of the flow pipe. We estimate that the radiative heat flux is 0.46 W/m^2 when the shield temperature is 80 K. Although this is locally a very small heat flux, the total radiative heating power on the flow pipe can still cause unwanted flow disturbances and increase the boil-off rate by 0.27 L/h . To solve this issue, we added 20 layers of MLI wrapped around the flow pipe. In this case, the heat flux is reduced to about 23 mW/m^2 which is completely negligible.

4.2.3 Implementation and Testing of the Flow Driving System

The two old bellows pumps in helium stacks were ruptured in the incident. In order to generate He II flows in the pipe, a single functional bellows pump system is sufficient. Therefore, we removed the ruptured bellows and installed a new bellows in the left stack to serve as the liquid helium pumping mechanism. This liquid helium bellows pumping system is shown in Fig. 4.5(a). The bellows is manufactured by BellowsTech, LLC. The inner and outer diameters of the bellows are 181.6100 and mm 205.3082 mm, respectively. The mean effective geometric area A_{eff} is 29394.651 mm^2 at the natural length. The stroke length is 10.16 cm which allows a maximum volume displacement of about 3000 cm^3 . We connected the bellows pump to a linear actuator (Parker ETS32) using a transmission rod. The actuator is mounted co-axially on the top of the left stack. We used a new sealing bellows to connects the rod to the actuator on top of the left stack and seal the system. A computer-controlled stepper motor (Parker S57-102) is geared in parallel to drive the linear actuator. The stepper motor is a precise motion controller capable of sending motion pulses with a resolution of $0.3 \mu\text{s}$. The linear actuator has a maximum thrust of 600 N which can generate He II flows with Re_D exceeding a million in the flow pipe. To ensure a convenient

operation of the pump system and a constant flow rate through the flow pipe, a cryogenic filling mechanism was needed. We installed a superfluid leak-tight valve to the bellows which allows us to control the liquid helium supply into the bellows. The bellows is connected to the flow pipe through a corrugated tubing with smooth ends. The corrugated geometry is chosen to provide flexibility and withstand thermal contractions. At the end of the flow pipe, liquid helium will be collected through two wide tubes in the right stack. Between runs, we usually wait for at least two minutes so the liquid level can relax back to equilibrium in the stacks.

The mean flow velocity averaged over the pipe cross-section area U (we simply call it average velocity) is an important parameter in our experiments. To accurately measure U , we measure the bellows velocity v using a precision laser displacement (Micro-Epsilon ILD-1220) with a resolution of $1 \mu\text{m}$ and an acquisition rate of 1 kHz . The average velocity U can be calculated based on the mass flow rate:

$$U = \frac{v \times A_{\text{eff}}}{A_{ch}} \quad (4.2)$$

where A_{ch} is the pipe flow cross-section area.

In general, when a bellows is contracted with a constant velocity, the volumetric flow rate does not necessarily remain constant. In practice, the outer diameter of the bellow is mechanically constrained and remains constant. However, the inner diameter will slightly reduce in contraction. This effect on the bellows geometry is schematically shown in Fig. 4.5(b). By analyzing the bellows

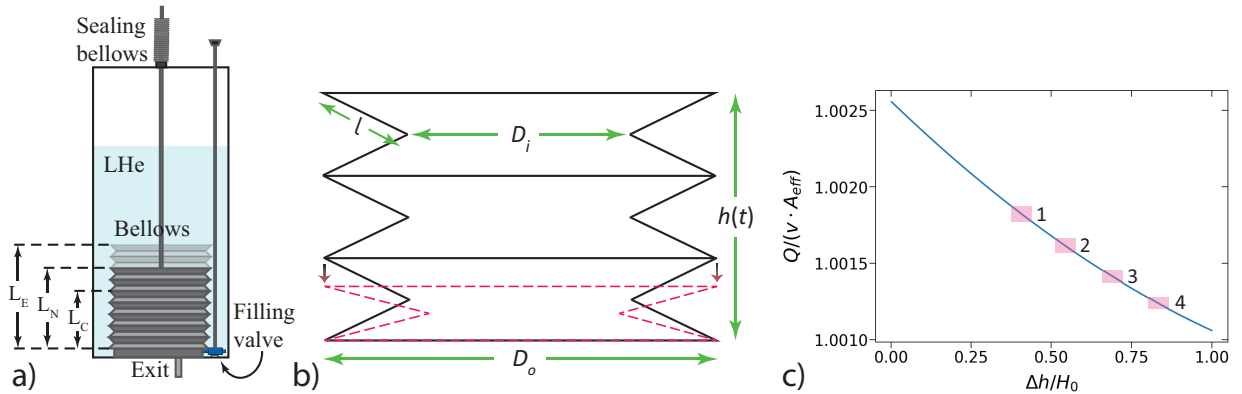


Fig. 4.5: (a) A schematic diagram of the liquid helium pumping system where the bellows and the filling valves are depicted. E, N, and C subscripts stand for expanded, natural, and compressed, respectively, and L denotes length. $L_N = 4.88 \pm 15\%$ and allows 1 inch expansion and 3 inches compression. (b) A schematic diagram of the bellows geometry during contraction. (c) Normalized volumetric rate ratio as a function of normalized bellows top surface position for a full-stroke contraction. The time that the sequence of images take place are highlighted with red rectangles.

geometry, the instantaneous bellows volume flow rate $Q(t)$ as a function of the bellows top surface position $h(t)$ can be calculated using:

$$Q(t) = \frac{d\left(\frac{\pi}{3} \left[\frac{D_o^2 + D_i^2 + D_o D_i}{4} \right] h(t)\right)}{cdotdt} \quad (4.3)$$

such that $D_i = D_o - 2[\sqrt{l^2 - (h(t)/2N)^2}]$, $l = \sqrt{(H_0/N)^2 + (D_o - D_i)^2/4}$ is the length of the teeth and can be calculated at the natural length, $N = 100$ is the number of teeth, and $h(t) = H_0 - vt$ where H_0 is the initial height of the bellows, usually at 10 cm. The flow rate ration can be defined as the instantaneous volumetric flow rate divided by the multiplication of the effective cross-section area provided as the specification of the bellows by the manufacturer A_{eff} , and the bellows compression velocity.

Our bellows is thin-wall, high-pitch, and narrow-teeth. This particular design ensures a very constant flow rates in a motion. Our bellows normalized volumetric flow rate $Q/(vA_{\text{eff}})$ with respect to the normalized bellows top surface position $\Delta h/H_0$ is calculated and shown in Fig. 4.5(c) where the typical time intervals where the images are taken are highlighted. As it can be seen, the normalized flow rate remains very constant. The variation in the flow rate between images is smaller than 0.1%. To be completely precise, we still conciser these slight changes in our calculations and use the accurate instantaneous flow rate for each image to calculate the average velocity in each experimental measurement. The above analysis assumes there is no fluid leakage during the flow motion. We have conducted leak checking tests and proved that this is indeed the case in our system.

4.2.4 Generating Controlled High *Re* He II Flows in LHFVF

To generate a flows in the flow pipe, we first fill the bellows by moving the actuator up gradually while keeping the filling valve open. Then, we close the filling valve and push the bellows down by controlling the stepper-motor using a LabVIEW computer program. It is important to keep a very constant averaged velocity in the flow pipe. We can achieve that using our computer program by controlling the bellows velocity v , its transient acceleration a_{bel} , and the total displacement Δh . Fig. 4.6(a) shows a representative bellows displacement data as a function of time obtained using the laser displacement. A linear fit to the data allows us to determine the bellows velocity and the associated uncertainty. The uncertainty of the data is very small and is shown for five runs in Fig. 4.6(b) as error bars. It is clear that under the same control condition, there is negligible variation of the bellows velocity in different runs.

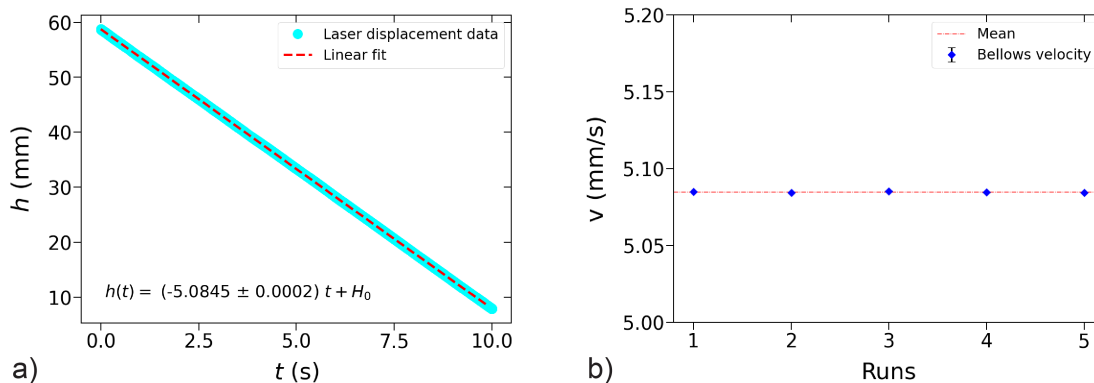


Fig. 4.6: (a) Bellows displacement in He II analyzed as a function of time for a compression with an input control velocity of 5.08 mm/s (b) Five bellows motion runs in He II and their uncertainty (lays within the data points). It is clear that the variation between runs is negligible.

4.2.5 Measurement Time Window

Typically in the experiments, we use bellows velocities in the range of $4 < v < 8$ mm/s. These velocities are corresponded to flows with Reynolds numbers in the range $6.3 \times 10^5 < Re_D < 1.3 \times 10^6$. Due to the finite stroke length of the bellows, the experimental time Δt_e for flow measurements is limited to approximately $\Delta h/v$. Therefore, the experimental times in the range of $10 < \Delta t_e < 20$ s are achieved. The time scale of the full development of pipe flow turbulence Δt_p can be estimated as $25D_h U^{-1}$ [44]. Thus development times in the range of $850 < \Delta t_p < 1700$ ms would be needed. As a consequence, we will have measurement time windows Δt_m in the range of $9.1 < \Delta t_m < 18.3$ s depending on the flow average velocity.

4.2.6 Pressure Drop Measurements in LHFVF

In pipe flow research and applications, the fluid pressure drop due to frictional losses is an important parameter and is related to the friction factor f_D . In order to make pressure drop measurements in-situ, we installed a Validyne DP10-20 sensor on the flow pipe as shown schematically in Fig. 4.7(a). This sensor is a variable-reluctance differential pressure transducer (DPT) that provides output voltage signals proportional to the pressure difference. The DPT operates based on the deformation of a sensing membrane when there is a pressure difference on the two sides of this membrane. The sensor has two legs connected to the body of the flow pipe separated by $L_f = 1.83$ m. A Validyne CD19A carrier demodulator is used to trigger the sensor and read the inductance changes due to the membrane deformation. The output voltage signal from CD19A

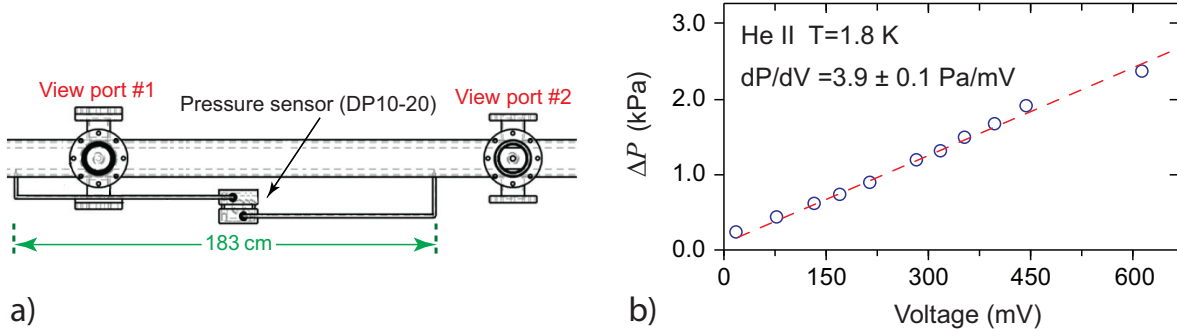


Fig. 4.7: The flow pipe and the locations where the pressure drop is measured by using the DPT sensor. The optical view ports are shown for reference.

can be calibrated to produce accurate differential pressure readings. We chose model DP10-20 for its matching differential pressure reading range of 0–860 Pa and a very good linearity in signal response. As the manufacturer specifies and it was verified later in our experiments, the response remains linear up to 200% full pressure span with less than 0.5% zero shift. This range is sufficient to entirely covers the range of the anticipated pressure drop in our He II pipe flows. Depending on the flow velocity, a pressure drop of several tens of Pascal is expected.

Since DP10-20 is not calibrated at temperatures below 220 K, we calibrated the sensor by submerged it in still liquid helium in a calibrator cryostat at a regulated bath temperature in the range of 1.5-4.2 K. We connect one side of the membrane to high vacuum while the pressure on the other side can be controlled using a helium gas supply. A representative calibration curve at 1.8 K is shown in Fig. 4.7(b) as an instance. The sensor response behaves linearly up to about 2500 Pa pressure difference. The conversion coefficient between voltage and ΔP can be determined through the slope of a linear fit to the data since we zero CD19A prior to calibrations.

We have tested the DP10-20 sensor in both He I and He II flows. However, in our experiments we have identified some issues that make the pressure drop measurements in He II impossible. It turns out the sensor noise increases by orders of magnitude when we go across the lambda phase transition. It is likely due to the fact that in superfluid phase, He II can easily leak through microscopic holes on and around the membrane. As a result, when there is pressure difference He II can move back and forth through the membrane easily which can cause large signal fluctuations. We find out the noise level in He II is usually as large as several hundreds of Pascal which is similar to the results reported in early research [5]. This noise level is much larger than the anticipated pressure drop in our He II flows, thus no meaningful measurements can be done. To make reliable

pressure drop measurements in He II, a much larger pressure drop is needed so the relative noise level would be insignificant. To achieve that, one needs to either significantly increase the motor actuating force and accordingly the flow velocity as was done in [5] or reduce the pipe size as was done in [3]. Therefore, we did not make any pressure drop measurements in He II in our experiments. Instead, we rely on the existing He II friction factor data from the literature as discussed in Chapter 5.

CHAPTER 5

OPTICAL SYSTEM AND MEASUREMENT PROCEDURES

Experimental flow visualization is still a very powerful tool in studying the fluid flows, especially where using numerical simulations are practically impossible. He II turbulent pipe flow is indeed an example of such problems. On the other hand, He II is notoriously difficult to visualize as well, due to the extremely cold and partial vacuum condition, and the low density of helium. In this chapter, we introduce the details of the MTV visualization technique in He II. We explain how we have incorporated this powerful technique to the LHFVF system for visualizing High Re He II pipe flows.

5.1 Flow Visualization Technique in He II: Molecular Tagging Velocimetry

There are serious concerns in the conventional solidified particle as tracers in cryogenic flow visualization. The measurement resolution is often relatively poor and the injected particles usually strongly disturb the flow to be studied. In the case of He II, they can also get trapped in quantized vortices [19]. In our MTV technique, there is no foreign tracer particles introduced into the fluid. Instead, metastable helium molecules He_2^* in the excited electron-spin triplet state serve as tracers. These excimer molecules can be created in helium as a consequence of ionization or excitation of the ground state helium atoms [14, 54]. These molecules form tiny bubbles in liquid helium (about 6 Å in radius [55]) and have an exceptionally long lifetime of about 13 s [56] due to a strongly forbidden spin flip during the decay [56, 57]. This gives abundant time to study the flow under the experiment. Standard tracer particles in fluid dynamics are those that faithfully follow the flow motion. He_2^* molecules follow the fluid motion in He I. In He II, these molecules are still entrained by the viscous normal-fluid component since the Stokes drag easily dominates other forces simply due to their small size and density [58]. At sufficiently low temperatures (below 0.6 K) in the relative absence of the normal fluid, they can bind to and visualize the quantized vortices [59, 60].

Generating tracerlines in a fluid by exciting the fluid molecules or creating new molecules using high energy means such as powerful laser beams has been adapted in classical fluids research [61, 62]. For instance, molecular tagging velocimetry for studying air flows was adapted in Princeton University via tagging oxygen molecules in Raman excitation [63]. Tracerline patterns produced in air can be followed in time and by measuring their displacement, information about the velocity field can be obtained while the dispersion of the tracer molecules can be related to the mixing processes in the flow. Recognizing the power of MTV, there have been various molecular tagging techniques incorporated in air and other gases for a wide range of practical flows (e.g., jet flows, pipe flows, etc.) [64–68]. However, these experiments are usually limited to relatively lower Re due to the working fluid properties. Developing quantitative MTV techniques applicable to cryogenic helium-4 provides new opportunities in turbulence research as it combines the strength of MTV and the advantage of helium-4 as the working fluid.

5.1.1 Metastable Helium Molecules

When helium atoms are ionized or excited in cryogenic helium, the resulting ions or excited atoms can undergo chemical reactions with surrounding ground-state helium atoms, leading to the spontaneous formation of metastable He_2^* molecules [14, 54]:



where “*” denotes excited electronic states. Therefore, there is no need for seeding the helium with foreign particles to create the He_2^* molecules. The excited molecules are produced in both electron-spin singlet ($A^1\Sigma_u^+$) and triplet ($a^3\Sigma_u^+$) states. The singlet state molecules radiatively decay in a few nanoseconds [69], but the triplet state molecules have a lifetime of about 13 s. These triplet molecules form tiny bubbles in liquid helium or dense helium gas that can serve as tracer particles.

These He_2^* tracers have many distinct advantages compared to the tracer molecules used in typical MTV experiments [64–68]. For instance, the tagging lifetimes of the molecules in classical fluids are very short, normally in the range of 1-10 μs [62]. Therefore, those molecules are only applicable in flows with high mean velocities such that the tracer-line displacement within the short experimental time can be obtained. On the other hand, He_2^* molecules allows an experimental window sufficiently long to examine flows in helium essentially in any desirable range of velocities.

Additionally, in fluid dynamics research, tracers with limited molecular diffusion are desirable. He_2^* molecules show very small diffusion in liquid helium above 1 K [70] which is another unique advantage of helium versus room temperature MTV molecules. Moreover, above 1 K, these molecules faithfully follow the motion of the normal fluid (the bulk fluid) rather than getting trapped in the quantized vortices. Also the viscous relaxation (Stokes) time (τ_s) of these molecules is in the order of pico-second, therefore, they immediately start drifting with the normal fluid. In the opposite, the conventional frozen particles used in superfluid visualization experiments can easily get trapped in the quantized vortices due to their much larger micron-sized volume. This results in a much greater needed force for deattaching them from the quantized vortices and also their viscous relaxation time is much longer (about 0.2 ms [71]) which is not suitable for the time scales involved in the physics under our study. Viscous relaxation time can be calculated as:

$$\tau_s = \rho_p D_p^2 / 18\mu \quad (5.2)$$

where subscript “p” denotes the particles and μ is the viscosity of the fluid. It should also be noted that light refraction in liquid helium is a very small effect due to its small refraction index ($n=1.05$)

5.1.2 Cycling-transition Laser-induced Fluorescence

He_2^* molecules emit strong scintillation light upon creation. This scintillation light is generated upon the ionization (perfect synchronization) and produce strong visible light perfect for camera excitation. Unfortunately, our measurements show that the lifetime of the scintillation light in He II is less than 5 μs independent of temperature. Although we show in Chapter 6 that we use this technique to produce unprecedentedly clean baselines images, however, this lifetime is too short for most flow measurements in our range of velocities. For the same reason, an innovative visualization technique was first developed at Yale University and advanced by Guo’s group [70, 72, 73]. This method relies on a cycling-transition laser-induced fluorescence (LIF) technique to image the He_2^* molecules. The technique involves a quantized optical transitions of the He_2^* molecules as it is schematically shown in Fig. 5.1. The complete physical picture is given in [73]. The He_2^* molecules in their original state, i.e., triplet ground state $a^3\Sigma_u^+$, can be excited using two infrared photons at 905 nm to an excited electronic state, i.e., $d^3\Sigma_u^+$. The occurring rate of this transition is usually above 5%. Majority (more than 90%) of the molecules that were successfully transitioned to the d state decay to the $b^3\Pi_g$ state in about 10 ns. The key feature comes from the fact that during this decay, the molecules release energy in the form of emitting fluorescence photons in the visible

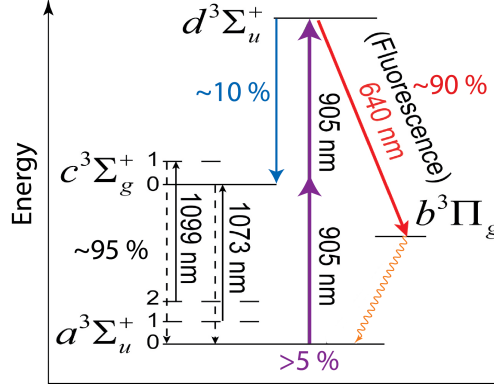


Fig. 5.1: Cycling-transition laser-induced fluorescence for imaging metastable He₂* molecules [73]. 0, 1, 2 denote the vibrational levels of the corresponding state. Color coded percentages show the amount of transited molecules.

range of 640 nm [73], which is straightforward to detect in an intensified CCD camera. From the intermediate $b^3\Pi_g$ state, molecules quench back to the $a^3\Sigma_u^+$ state, where their lifetime still lets them to survive and the entire transition path can be recycled to produce more fluorescence light. Each cycle occurs approximately in 50 ns. To enhance the LIF efficiency, re-pumping fiber lasers at 1073 nm and 1099 nm can be used to recover the molecules that fall to the long-lived excited vibrational levels [74]. Without the fiber lasers, the emission efficiency drops to less than a third of its initial value after a few cycles. It should be noted that even with the repump lasers, usually only 5% of the molecules in the 905-nm laser sheet emit 640 nm photon for each imaging pulse [73]. To filter ambient noise and unwanted laser light, a 640 nm filter with a FWHM bandwidth of 20 nm is used to minimize background noise. This technique has been successfully applied to image the He₂* tracers in various flows in helium [9, 72, 75–77]. To acquire quantitative flow field information, the displacement and distortion of the tracerlines are analyzed to determine the spatial velocity profile of the He II flow.

5.1.3 LHFVF Laser System for Creating Tracerlines using MTV

By creating and tracking the patterns formed by large amounts of He₂* tracers in He II, quantitative velocity-field measurements can be conducted. In fluid dynamic research, orthogonal velocity field information are often more desirable. Therefore, creating linear patterns of He₂* molecules, serving as tracerlines, can be a great advantage. In the past years in our lab, an advancement was accomplished on creating thin lines of He₂* tracers via laser-field ionization in helium. For this purpose, laser intensity as high as 10^{13} W/cm² is needed [78]. This high instantaneous laser

intensity can indeed be achieved by focusing a laser beam with extremely short pulse duration. A 5-kHz femtosecond regenerative amplifier laser system (FS-laser) allows the generation of 35-fs ($1 \text{ fs} = 10^{-15} \text{ s}$) pulses with a tunable pulse energy up to 4 mJ at wavelengths centered around $\lambda = 780 \text{ nm}$.

Subsequently, pulses from an imaging laser at 905 nm (IMG laser) can be used to drive the tracer molecules to produce fluorescent light at 640 nm [72, 75] for line imaging. The 905-nm imaging laser (Ekspla NP220-SP) is a 7-ns pulse lasers. The system had received minimal maintenance over the past 20 years of operation and suffered from two major incidents. Therefore, the functionality of this laser system as a key part of the MTV system was unstable. To improve the laser system and increase the imaging quality, we started a set of upgrading measures performed on the imaging laser system.

Ekspla NP220-SP is shown in Fig. 5.2. The first section of this laser system is a solid-state YAG (neodymium-doped yttrium aluminum garnet) laser where the photon generation occurs based on the atomic transition in the neodymium ion after being excited from an external source. A pockel cell is used to generate pulses with a 7 ns width and up to 5 W of power. The Nd:YAG laser is then guided to a second harmonic generator (SHG). Second-harmonic generation is a nonlinear

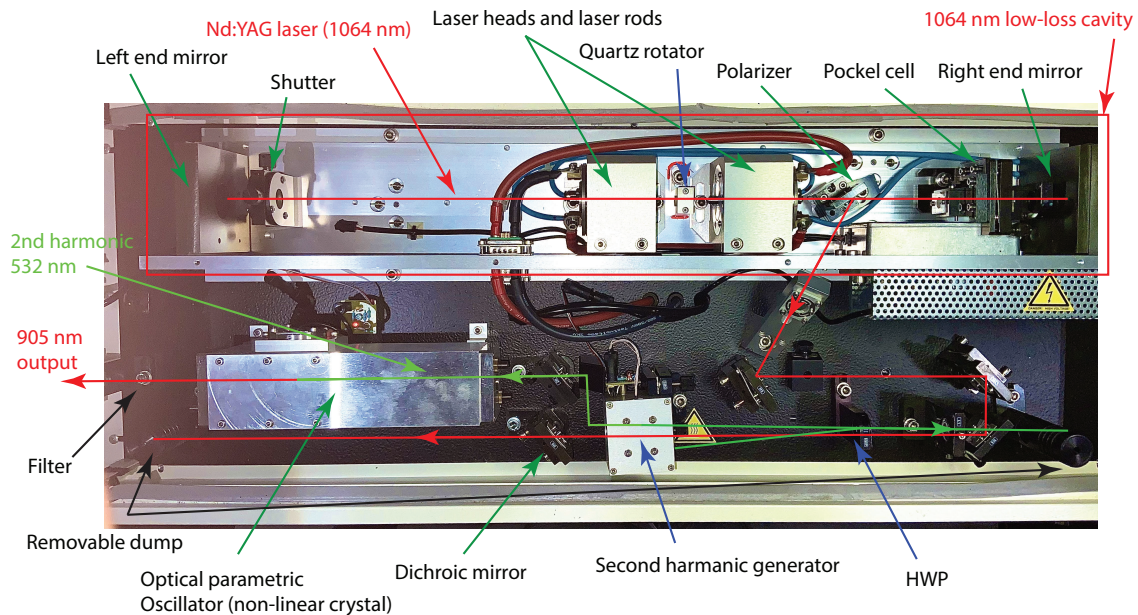


Fig. 5.2: Internal structure of the 905-nm imaging laser including the Nd:YAG 1064-nm laser cavity, second harmonic generator, and optical parametric oscillator (HWP stands for half wave plate).

optical process where two photons with the same frequency interact with a nonlinear material and generate a new photon with twice the energy of the initial photons. The second harmonic beam is then guided to an optical parametric oscillator (OPO) to generate 905 infrared laser with an efficiency of about 20%. The OPO is a solid state source of visible and near IR radiation which includes a type-II KTP nonlinear crystal. The desired 905 nm output is only achieved when the incident beam has a unique angle with the principle axes of the crystalline (vertical axes of KTP). The generated beam, in both intensity and wavelength, also strongly depends on intensity and perpendicularity of the pump radiation to the resonator mirror.

These laser systems are complicated and sensitive commercial systems which can degrade by time, ambient fluctuations, or vibrations. Therefore, they must be optimized or tuned once in a while to maintain optimal performance.

5.1.4 LHFVF Optical Design for Quantitative MTV

To implement the described “laser-field ionization+LIF” scheme, a dedicated optical system must have been designed. For the MTV technique to operate successfully in He II, 4 high energy laser systems including the femtosecond system, 905-nm imaging laser, and two re-pumping fiber lasers must be perfectly synchronized in space, time, and focusing domains. These criteria must be especially achieved precisely above the bottom solid wall of the flow pipe. During the experiments, this region of interest is always inside the body of the cryostat and thus inaccessible. Therefore, the spatial and focal coincidence must be approximately achieved outside the cryostat and be optimized during the experiment in-situ.

A simplified model of the optical design is described here while only the essential components are included. Firstly, the spatial and temporal optimization of the internal configuration of the major laser systems, i.e., FS and IMG systems, are achieved. Subsequently, the FS and IMG beams are guided from the main optical table (FS and IMG emission plane) to a secondary optical breadboard installed on top of the LHFVF first optical set. This configuration is shown in Fig. 5.3.

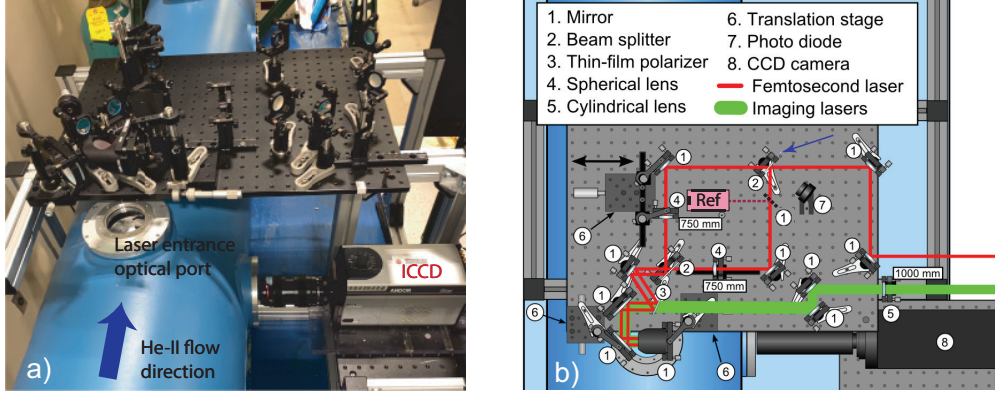


Fig. 5.3: (a) Secondary optical breadboard installed on top of the LHFVF view port#1. Lasers enters from the top window and imaging occurs through the side window. (b) The Schematic diagram of the system. The configuration can switch between single-line and double-line MTV using the beam splitter specified with the arrow. The reference laser can be merged to the beam path using a mirror for perpendicularity tuning.

A beam expander is used to increase the FS beam diameter from 1 cm to about 2 cm so that the desired 5-mm Rayleigh range with the proper field intensity can be created within the flow pipe. For an ideal Gaussian beam with a beam radius ω_0 at the focal plane, one can define a Rayleigh range $Z_R = \pi\omega_0^2/\lambda$ where ω_0 is the beam waist and λ is the wavelength. The laser intensity drops by 50% due to beam spreading within the Rayleigh range [79]. The FS-Beam is then focused using a plano-convex lens with $f = 750$ mm, mounted on an translation stage. This configuration can insert the focal point at any arbitrary distances from the bottom wall of the flow pipe. The fine tune is achieved using the translation stage without affecting the parallelity or orientation of the beam. This feature is especially useful for examining the NVP. On the other hand, the IMG-beam and the fiber beams are reshaped to sheet lasers (thickness: 1 mm and width: 10 mm) using cylindrical lens of $f= 500$ mm and 700 mm, respectively, and are spatially merged together using a beam combiner. They are then guided through a cylindrical lens of $f=1000$ mm placed on a translation stage to be focused in the flow pipe. Subsequently, all four beams are merged together using an ultra-fast polarization-based beam combiner for spatial coincidence. The temporal coincidence is purely achieved using the laser systems internal timing. The focal coincidence must be achieved via the fine tune of the focusing lenses. The last two mirrors that guide all the beams into the cryostat are each placed on a micrometer resolution translation stage such that their combination creates a $x-z$ (horizontal) control plane. Therefore, the 4 merged beams can be spatially placed on any point of the bottom wall as desired. The ultimate goal is to achieve four coincident beams perpendicular

to the bottom wall where the FS beam is placed in the center of the imaging-fiber sheet such that the laser sheet plane is in the streamwise direction and all focal points occur coincidentally in space. Only with this configuration, one can assure that the sufficient optical intensity for both creating the helium molecules and exciting them to produce fluorescence light will be achieved in a properly oriented laser field with respect to the flow direction. The orientation of the beams, including perpendicularity and the streamwise plane of the IMG sheet are crucial features. The first one assures the measured velocity field is indeed the velocity profile perpendicular to the wall, while the latter guarantees that the molecules are not washed out of the imaging domain due to the drifting. The entire aforementioned laser timing is indeed synchronized with the bellows motion control system via the LabVIEW code such that the laser timing and the He II fully-developed turbulent flow can be precisely overlapped. This is important because the length of the bellows only provided a limited experimental time. The spatial and focal coincidence of the laser beams are schematically shown in Fig. 5.4 (a).

The emitted fluorescence is captured through an appropriately focused collector lens into the ICCD camera mounted perpendicular to the tracerline plane. The spatial tune of the camera is indeed important to mitigate the camera curvature effects and picture distortion for more precise

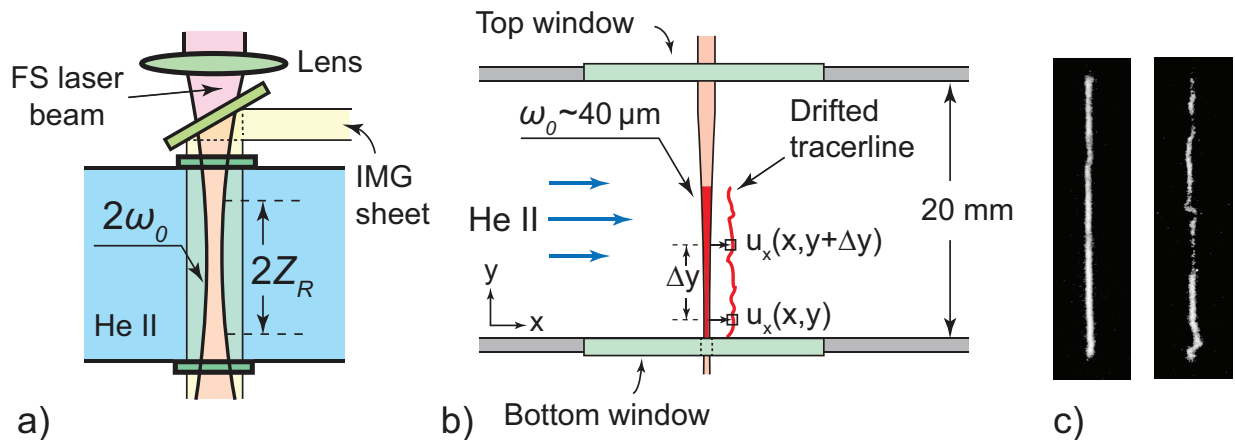


Fig. 5.4: (a) schematic diagram of the spatial and focal coincidence of the FS and IMG lasers to create a desired arbitrary Rayleigh range within the flow pipe. (b) A schematic showing a tracerline inside the flow pipe where the tracerline drifts with He II flow and then will be imaged. Flow field can be obtained by measuring the displacement of the drifted tracerline at any y location from the bottom wall. The average thickness of the beam in the Rayleigh range is typically about $80 \mu\text{m}$. (c) Test fluorescence images of the He_2^* tracerline generated in LHFVF He II flow pipe at 1.9 K (left:baseline, right: driftline). The width of the tracerlines is about $80 \mu\text{m}$ and the length is about 20 mm.

flow field measurements and subsequent uncertainty analysis [80]. Upon acquiring the drifted tracerline image after a drift time Δt , flow field information can be extracted by analyzing the image. Obviously, the flow in the normal fluid carries the tracerline and hence leads to deformation of the line. To extract the velocity information, the deformed tracerline is divided into small segments and their center positions are determined via Gaussian fits of their intensity profiles. When Δt is small, the streamwise velocity $u_x(y)$ can be calculated as the displacement of the segment at y divided by Δt . This process is schematically shown in Fig. 5.4 (b) and is calculated using:

$$u_x(y) = \frac{x_d(y) - x_b(y)}{\Delta t} \quad (5.3)$$

where subscript b and d denote baseline and drifted tracerline, respectively. We optimize the FS-laser power such that the He_2^* tracers are only created within the two Rayleigh ranges of the FS-beam. As we increase the FS-laser pulse energy, field ionization indeed occurs in helium when the pulse energy is higher than about $60 \mu\text{J}$ which leads to the generation of He_2^* tracers. As long as the FS-laser intensity is below the threshold of the dielectric breakdown in helium (about $5 \times 10^{13} \text{ W/cm}^2$), a thin line of He_2^* tracers can be reliably produced within the width of the flow pipe as a consequence of a controlled electron avalanche ionization [78]. In Fig. 5.4 (c), test fluorescence images of the He_2^* tracerline are shown upon their creation in He II at 1.9 K in the flow pipe. The width of the tracerline is about $2\omega_0 = 80 \mu\text{m}$ and its length is about $2Z_R = 16 \text{ mm}$ as expected. The heating in the fluid accompanying the generation of the tracerline is negligible since no abnormal diffusion of the molecules or line stretching in static helium following the tracer-line creation was ever observed [20].

5.1.5 Preventing Breakdown Near the Solid Wall

Our early tests showed that a strong He_2^* molecular deposition can occur close to solid walls as a consequence of a local dielectric breakdown in He II, in particular on the bottom window. This localized breakdown is caused because the local fluid density is lower than the bulk fluid due to the surface tension forces. As a result, the dielectric breakdown optical intensity threshold can reduce significantly. The high concentration of molecules on the bottom window produces plenty of unwanted fluorescence light and basically acts as an optical contamination. The molecules cover around the thin tracerline and make the interpretation of its displacement impossible. An example of these breakdowns are shown in Fig. 5.5 (a) in an image of two parallel tracerlines in the flow

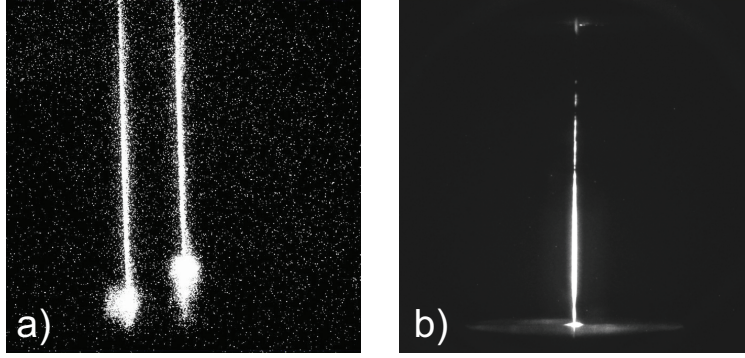


Fig. 5.5: (a) Dielectric breakdown near the bottom wall and consequent molecular deposition in He II at 1.8 K inside the flow pipe (b) Complete elimination of the breakdown near the bottom wall by a precise tune of the FS-beam through the hole.

pipe at 1.8 K. Although the breakdown can be partially mitigated by optimizing the position of the Rayleigh range in the flow pipe, it will never be completely eliminated. It turns out the only practical solution to eliminate the breakdown is to drill an infinitesimal hole of radius $r = 250 \mu\text{m}$ in the bottom window. We used a transparent smooth acrylic sheet with a thickness of 1.2 mm for this purpose because of the machinability, good low temperature properties and the rigid surface properties. In Section 4.2.1, we explained why the effect of such a hole on the scaling of the law of the wall in turbulent pipe flow is insignificant. The current configuration of the system used in the experiments is schematically shown in Fig. 5.6.

We use the beam profiler WinCamD IR camera for tuning the Fs-beam in the hole. The beam

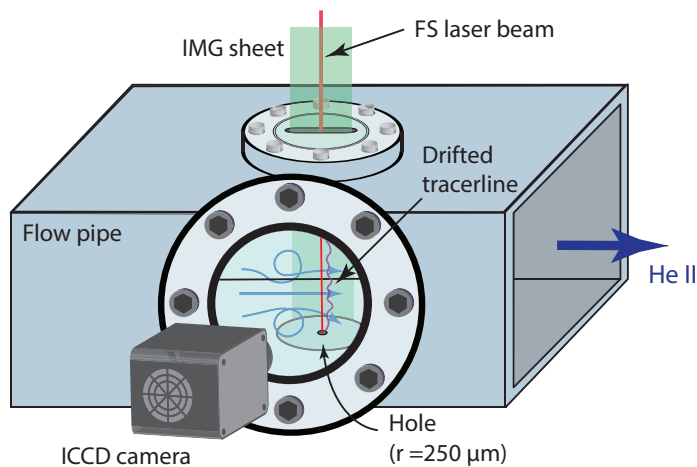


Fig. 5.6: Schematic diagram of the configuration of the flow pipe and the lasers

is slightly blurred when it passed through the acrylic bottom window and is strongly refracted when it intersects with the edges. But only when the beam is guided through the hole, a clean profile can be imaged. Using the micrometer translation stages in the $x - z$ plane on the optical breadboard, the distance between the diagonal edges of the hole can be calibrated and the beam can be precisely positioned closer to the upstream edge. Later, after pumping the flow pipe to below the λ transition, we re-tune the laser position to account for small thermal contractions. A representative tracerline image with a successful elimination of the breakdown near the wall using the described procedure is shown in Fig. 5.5 (b).

5.2 Measurements in High-velocity He II Pipe Flows using MTV

Conducting MTV measurements in relatively high-velocity He II pipe flows need a precise synchronization of the FS-beam, the IMG beam and the camera. The measurement procedure can be described as follows: we first send an FS-beam into the flow pipe. The temporal delay between the FS-beam and the IMG-beam sets the drift time $0 < \delta t < 2000$ ms. After the delay for the drift time, we send the imaging pulse with a width of 7 ns to excite the molecules and visualize them. The camera is triggered to capture light $1.5 \mu\text{s}$ before sending the IMG-laser and has an exposure time of $8 \mu\text{s}$. If one designs the laser system timing such that the subsequent pulses of the FS and IMG beams are introduced at the exact same intervals, the newly created molecules each time are bound to drift to the relatively same location. Although each pulse creates a limited number of molecules and an insufficient amount of fluorescence light, nonetheless we can show that superimposing 500-1000 of these exposures can indeed generate a high quality ensemble-averaged

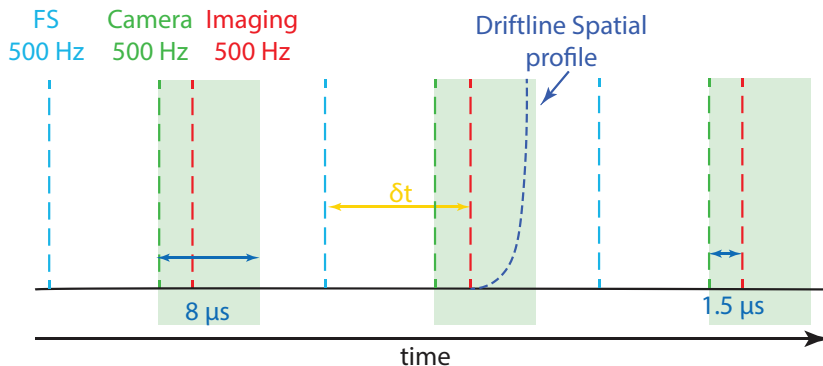


Fig. 5.7: The femtosecond, camera signal, and imaging laser pulses at 500 Hz. The green highlights depicts the camera exposure time which starts $1.5 \mu\text{s}$ before the IMG-beam radiation. When timed properly, all driftline profiles spatially collapse.

image of the drifted lines. This indeed results in the visualization of the mean flow due to averaging out the turbulence fluctuations. This procedure is schematically shown in Fig. 5.7.

5.2.1 Resolution of Our Flow Field Measurement Technique

In turbulence research, it is desired to have a probe resolution smaller than the smallest scales of turbulence which are usually found near the wall [81]. In reality and in extremely high Re flows, achieving this is usually impossible to the finite size of the probes and extremely small turbulence length scales. Therefore, there are always averaging effects in the measurements. The averaging effects are typically evaluated using the dimensionless spatial resolution l^+ , defined as the ratio of the probe size l to the wall unit as $l^+ = lu_\tau/\nu$ [81]. (?? the Kolmogorov length scale defined as $\eta = (v^3/\varepsilon)^{0.25} \approx D_h Re_D^{-0.75}$ where). In the Superpipe experiment, the smallest hot-wire probe has an active length of $l = 30 \mu m$, and the wall unit at the highest Re_D is about 1 micron [82]. Therefore, l^+ is about 30 in their experiments which is sufficient to allow them to study the NVP.

In flow field measurements using MTV, typically a half of the tracerline thickness (about ω_0) largely sets the spatial resolution [83]. This is usually the minimum distance over which the displacement of the tracerline can be resolved. ω_0 is related to the focal length f and the incident beam radius ω_f as $\omega_0 = \lambda f/\pi\omega_L$ [79]. Therefore, by using a lens with an appropriate f and by adjusting ω_f , a desired thickness of the tracerline is achieved. In the current experiments, it is feasible to reduce the probe size l via focusing the FS-laser beam to about $l = 40 \mu m$ while maintaining the laser intensity at a sufficient level. In Chapter 6 we will show that the wall unit in a typical LHFVF experiment is about $0.5 \mu m$. Consequently, the dimensionless resolution in this experiment is of the same order in comparison to that in the state-of-art Superpipe experiments at a similar Re_D . It must be noted that the law of the wall was observed at $y^+ > 600$ in the Superpipe experiments. The current resolution $l^+ \approx 80$ is sufficient to resolve the details of the NVP in He II.

CHAPTER 6

DATA ANALYSIS

In this chapter, we present our image processing algorithm together with our data fitting method. We explain how we obtain quantitative data of NVP in He II from the raw data contained in the MTV images. The quality of the images in our experiments strongly depends on the experimental conditions that include: the flow velocity, drift time, number of superimposed snapshots, FS laser frequency, and spatial, temporal, focal and power optimization of the laser beams. To resolve the subtle region near the wall, high quality MTV images with unprecedented optical accuracy are needed. Therefore, we first conducted a set of preliminary experiments to determine the optimal experimental/optical conditions and parameters. For instance, we determine the optimal/allowed values for the flow velocity, maximum drift distance of the tracerlines, and the number of superimposed exposures equal to $0.45 \leq U \leq 0.6$ m/s, $230 - 280 \mu m$, and 500-600 snapshots, respectively. These values typically produce the highest quality images and correspond to pipe flows with $9.7 \times 10^5 < Re_D < 1.3 \times 10^6$. The data was obtained in He II at 1.9 K where the normal fluid and superfluid component exist in close portions.

6.1 Obtaining NVP Data By Developing A Robust Image Processing Algorithm

The baseline images simply show the position of the molecules right after their creation in still He II. On the other hand, the driftline images show the location of the molecules after being drifted with the flow field with a drift time δt . Drift time is very accurately controlled via the laser timing settings and can be measured using an ultra-fast oscilloscope. The combination of a baseline-driftline pair contains the mean flow velocity field information perpendicular to the bottom wall approximately up to the half width of the flow pipe. Such quantitative information can be extracted from the MTV images using an image processing algorithms. Typical baseline and driftline images in our NVP experiment are shown in Fig. 6.1 (a,b). As it can be seen in Fig. 6.1 (b), the same tracerline shows itself multiple times over time. The reason is that the molecules do not simply disappear after being imaged in downstream. They continue to drift with the flow and will be

imaged in the subsequent snapshots. We later show how we extract valuable flow field information from the second exposure of the driftline.

A set of background images are also taken at the same experimental temperature, temporally before the tracerline images. The solid boundaries (bottom and top windows) are illuminated using visible light. These images contain information about the position of the solid boundaries. Since the width of the flow pipe is known, we can also determine the scaling of the flow pipe in our images using the background images. They can also be used to measure the relative angle between the camera principle axes and the flow pipe streamwise direction. We use this information to zero the camera angle in-situ.

We developed the image processing algorithm particularly to analyze the high frequency MTV images in our NVP experiment. First, we convert the images taken using the ANDOR ICCD camera to raw data files. The raw data files contain the location and the intensity of all the image pixels. Thus, an algorithm can be developed such that the position of the tracerline is extracted from the intensity and location data. The tracerlines have a finite thickness, therefore, the pixel intensity data indicate a finite width line rather than an actual line which cannot be immediately used in flow analysis. Therefore, to find the quantitative position of the tracerlines, the following steps in our data analysis algorithms are taken:

1. We define the frame of analysis starting from the bottom solid boundary to the half width of the flow pipe. This region approximately matches the extents of the tracerlines. The frame of analysis is cut into thin horizontal strips which are called the binning bars. The binning bar width w_b is an important parameter in image processing techniques. The goal of optimizing

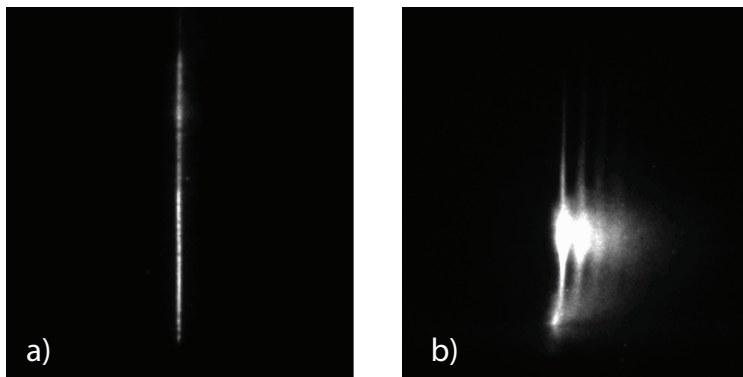


Fig. 6.1: (a) Baseline image in still He II at 1.9 K $50 \mu\text{s}$ after the creation. (b) Subsequent driftline image with $\delta t = 600 \mu\text{s}$ and 600 snapshot superimposition at FS-1 kHz when $U = 0.468 \text{ m/s}$ and $Re_D = 1.01 \times 10^6$.

this width is to achieve the smallest resolution before introducing artificial instability in the algorithm due to computational smearing. It was previously shown [83] that the thickness of the tracerlines roughly determines the minimum binning bar width in the MTV technique. Our analysis again shows that w_b equal to the tracerline thickness yields the best results. The binning bar half width sets the minimum spatial resolution.

2. The images light intensity data is integrated vertically in each binning bars such that each segment represents an intensity function with respect to streamwise direction, x .
3. The location of the tracerlines can be determined based on the intensity functions. In order to do so, in each binning bar, a Gaussian curve is first fit to the intensity function at the first and second intensity peaks. The peak of the Gaussian beam determines the location of the tracerline in the corresponding binning bar where the standard error of the peak determines the uncertainty of this location. The curve fit is performed using the least squares method (LSM).
4. This process is compiled vertically for the entire frame of analysis so that the extents of the baseline and driftline images are swept. As a consequence, the position of the tracerlines and the uncertainty associated with it at different distances from the bottom wall y are acquired.
5. The scaling of the camera pixels in the flow pipe is determined using the background images. The pipe width of 20 mm is divided by the number of pixels between the bottom and top solid boundaries. This determines the actual size of each pixel Ω in-situ.
6. The drift distance is calculated as the distance between the location of the baseline and driftline multiplied by the pixel size. The mean velocity profile is calculated as the drift distance divided by the drift time δt . The calculations are performed for each binning bar, therefore, the entire velocity profile as a function of y close to the half width of the pipe is determined.
7. Secondary analyses such as obtaining the scaling of mean velocity profile and the associated uncertainties can be performed.

In the rest of this chapter, we expand upon each of these steps.

6.1.1 Analysis of Background Images

The Background images must be taken right before the flow field measurements. This is to ensure that the flow pipe conditions will not change from taking the background images to the experiments. Otherwise, small environmental vibrations or thermal contractions can slightly change the result of the pixel size calculations and these inaccuracy would propagate in all the measurements. A typical background image in He II at 1.9 K is shown in Fig. 6.2(a) where the reflection from the hole and the top window can be clearly seen.

It is important that the camera is focused exactly on a plane parallel to x where the FS-beam is emitted. This is essentially the plane we study the flow on it. To achieve this camera tune, we first use the bottom window reflection to focus the camera on this unique plane. Later during the experiments, the tracerlines themselves are used to fine focus the camera lens on this plane. A set of background images are taken. The light reflection off of the solid boundaries is captured with a high contrast on the camera focal plane. We use this reflection to determine the accurate position of the solid boundaries. We divide the high intensity region in the center of each solid boundary into several vertical segments. The light intensity is integrated in the streamwise direction in each segment. We determine the location of the solid boundary as the location of the maximum light intensity in each segment. Subsequently, we fit a linear function to the maximum points at the lower and upper solid boundaries as $y_{1,2} = (m)x + b_{1,2}$, respectively, where the origin of the coordinate system is at the center of the hole. This procedure is shown in Fig. 6.2(b). The linear function is fit using LSM.

Since the flow pipe and the camera are carefully leveled, the slope of the linear functions is close to zero and must be equal since the walls are parallel. We rely on the bottom wall to determine m since it has a very precise physical signature (the hole) and is easier to illuminate in the experiments. If needed, we adjust camera positioning in-situ to minimize the slope. The typical slope m in our experiments is less than 0.004. Such slope causes less than 10 μm tilt in the entire fitting range which is 0.05% of the pipe width and thus negligible. The uncertainty in the intercepts of the fitting lines can be determined using the python `Scipy.optimize.curve_fit` package as a result of the

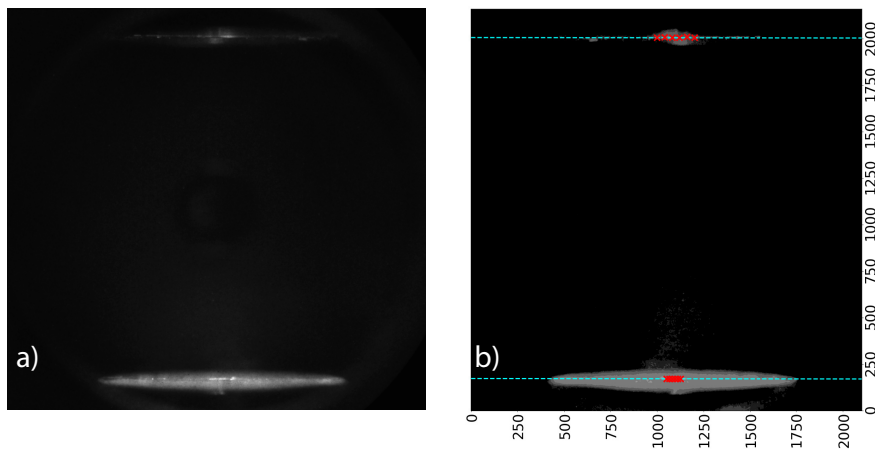


Fig. 6.2: (a) A typical background image in He II at 1.9 K (b) Determination of the pixel size in the flow pipe by fitting horizontal lines to the light intensity on the bottom and the top windows

LSM. The distance between these two parallel lines is calculated using $|b_2 - b_1|/\sqrt{1 - m^2}$ where the second order term m^2 is negligible. This distance is equal to the width of the pipe. Therefore, the size of a single pixel together with the position of the solid boundaries can be determined. The pixel size is defined as:

$$\Omega = \frac{D}{b_2 - b_1} \quad (6.1)$$

The pixel size in our experiments is typically $10.935 \mu\text{m}/\text{pixel}$. Note that we use a lens with a suitable focal length to maximize the camera solid angle which was previously shown as an important factor in this type of measurements [73].

6.1.2 Analysis of Tracerline Images

After acquiring the pixel size, the thickness of the tracerlines can be determined. In each binning bar, the light intensity as a function of streamwise direction shows a Gaussian-like distribution where the thickness is defined as the full width half maximum. Since FS-beam intensity in the experiment is optimized such that the tracerline is only created within the two Rayleigh range, the tracerline width remains fairly constant in the entire length of it in our experiment. We examine the thickness versus the calculated FS-beam waist to ensure the expected performance of the system. In our experiments, the baseline and driftline thickness are typically 80 and $110 \mu\text{m}$, respectively. We set the width of the binning bars $w_b = n\Omega$ approximately equal to the driftline thickness. Then, we fit Gaussian functions to the baseline and driftline images in each binning bar as shown in Fig. 6.3(a,b).

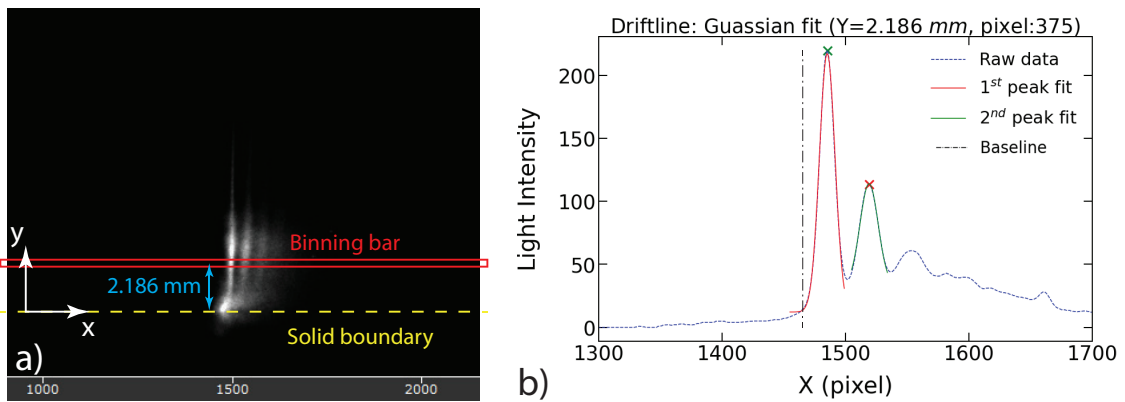


Fig. 6.3: (a) Sweeping the entire frame of analysis in each binning bar parallel to the bottom solid boundary (b) The light intensity in binning bar at $y = 2.186 \text{ mm}$ as a function of streamwise pixel number, X , and the Gaussian functions fit to the intensity data at the first and second peak. The absolute maximum is denoted with \times and \times , respectively.

The entire length of the tracerlines is swept where the binning bar each time moves by half of its thickness to the next y location. This sets the minimum spatial resolution of our experiments to $w_b/2$. The true spatial resolution in each measurement is the mean drift distance below which the velocity field information is averaged. The mean drift distance in the near-wall region is typically about $110 \mu\text{m}$ in our experiments which is again similar to $w_b/2$. As a result of this treatment, the location of a tracerline at each wall coordinate y can be accurately determined. The accuracy of similar procedures have been already shown elsewhere [83]. The results of such treatment for a typical baseline and driftline pair are schematically shown in Fig. 6.4(a,b), respectively.

The baselines have a unique situation. We create each baseline using a straight laser beam in undistributed He II and image it right after with practically no drift time. This efficiently mitigates the molecular diffusion. Therefore, we expect the baseline images to exhibit a straight line perpendicular to the bottom wall. During the optical tuning, we ensure this perpendicularity. We first examine whether the perpendicularity is achieved in the experiments because it is important to analyze the velocity profile exactly perpendicular to the wall. The tilt Θ_b of the tracerline with the wall normal direction can be calculated as:

$$\Theta_b = \text{Arctan} \left(\frac{2}{D} \frac{1}{n} \sum_{i=1}^n (X_i - X_b) \right) \quad (6.2)$$

where X_b is taken as the pixel location of the baseline on the bottom solid boundary. Typically Θ_b is calculated less than 0.06° tilt in the streamwise direction in our experiments. This clearly shows the good precision of our laser tuning.

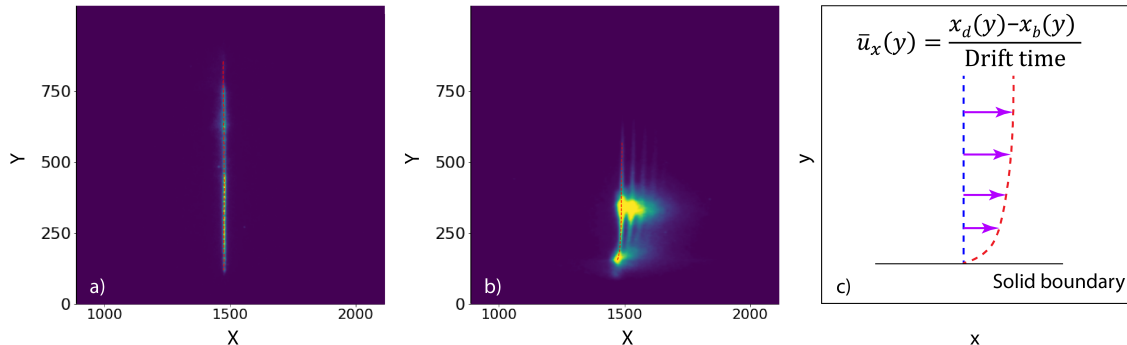


Fig. 6.4: (a) A representative result of the image processing algorithm used to determine the baseline. (b) Determination of the subsequent driftline. (c) A schematic diagram showing the procedure for determining the mean velocity profile based on the drift distance and the drift time. Subscripts b and d denote baseline and driftline, respectively

The y location of the tracerline is defined with respect to the bottom wall as $\Omega Y - \Omega Y_0$, where Y_0 is the pixel location of the solid boundary and Y is the pixel location of an arbitrary y location.

6.1.3 Obtaining the Mean Flow Velocity Field

The streamwise mean velocity profile is calculated as:

$$\bar{u}_x(y) = \frac{[X_d(y) - X_b(y)]\Omega}{\delta t} \quad (6.3)$$

where X is the pixel axis and the turbulent fluctuations, $\delta u_x(y)$, is averaged out due to the superimposition of 500-600 instantaneous velocity profiles. This results of this treatment is schematically shown in Fig. 6.4 (c) by analyzing a immediate pair of baseline and driftline images.

It must be noted that there is no guarantees that the molecules at an arbitrary y location created along the baseline drift exactly horizontally. Due to this, there is an inherent error in determining the streamwise velocity which is a known issue of the MTV technique. Guo [84] proposes a double-exposure-delay approach to solve this issue. In essence, this method relies on imaging the same tracerline at two different drift times. As a consequence, there would be a finite distance between the baseline, the first and the second drift driftline. It can be shown [85] that if the drift times are small, the actual streamwise velocity can be calculated by solving a system of equations as:

$$\begin{aligned} u_y &= u_{y,1}^{(p)} + a \cdot \delta t_1, \\ u_y &= u_{y,2}^{(p)} + a \cdot \delta t_2. \end{aligned} \quad (6.4)$$

where u_y is the true streamwise velocity, $u_y^{(p)}$ is the perceived streamwise velocity (what we measure in MTV), subscripts 1,2 denotes the first and second image, and $a = u_x \cdot (\partial u_y / \partial x)$.

As it can be seen in Fig. 6.1(b), besides the first strong driftline exposure, there exist a second, third, and fourth downstream exposures. The molecules diffuse while drifting further downstream but they relatively keep their coherent structure. The imaging beam is a sheet that is long enough to cover this far drifted molecules (the drift distance of these old molecules is still in the order of 500 μm which lays within the focal width of the imaging sheet). The far drifted molecules are imaged for every subsequent pulse, therefore, a series of 2-5 minor driftline exposures can be seen in the images. Nevertheless, the main beam intensity is much stronger such that we can conveniently distinguish it in our image processing algorithm and the minor tracerlines do not affect the accuracy of the data analysis.

On the other hand, the second tracerline is sufficiently distinguishable at larger y , so we can analyze it individually. Analyzing the second peak indeed offers unique opportunities in our experiments. For instance, one can use the data obtained from the second peak to construct a second independent mean velocity profile. This can be used as a validation of the image processing algorithm. The second peak is dominated by the strength of the main peak intensity in the near-wall region, nonetheless, the situation is different in the bulk region. In the bulk, the second peak is fully distinguishable and can be reliably analyzed. More importantly, we can further investigate the second peak data in the bulk region to develop the double-exposure-delay analysis. Solving the system of equations in Eq. 6.4 for $3 < y < 5.5$ mm in the bulk region and taking an average, $a = 4.2 \pm 0.1$ m/s² and $u_y - u_{y,1}^{(p)} = 2.92 \times 10^{-3}$ (0.6%) are obtained. As it can be seen, the difference between the actual velocity and the calculated velocity is totally negligible, thus this proves the robustness of our developed MTV technique in studying the flow fields. Consistent results are obtained by repeating the same analysis upon different experimental trials. Note that we expect the deviation to be even smaller in the near-wall region because the deviation scales with the mean velocity [85].

6.1.4 Constructing the Mean Flow Velocity Profile

The mean velocity profile is calculated based on Eq. 6.3. The results of a representative experiment in He II at 1.9 K, where $U=0.468$ m/s and $Re_D = 1.01 \times 10^6$, is coherently drawn versus the real wall coordinate in Fig. 6.5(a). The spatial resolution is $55 \mu\text{m}$. Therefore, no meaningful information for wall coordinates smaller than that can be obtained in our experiments. In classical fluids and in this range of Re_D , one would expect the viscous sublayer to lay within this region where a linear velocity profile is already established [86]. In He II, it is not yet known how this region is scaled or whether the no-slip condition truly stands. However, very limited numerical data at much lower Re_D assumes that the no-slip condition should still hold for the normal component whereas the superfluid component can slip [87]. The main difference in the case of superfluid component is that any velocity gradient can only exist as a result of a unique vortex line density gradient and polarization near the wall [53]. We simply assume a linear profile for the normal fluid from the solid boundary to the first available experimental data in our flows. Starting at $55 \mu\text{m}$ above the bottom wall, a strong shear region near the wall is evident. The shear region seemingly ceases at about 1.2-1.5 mm away from the wall where the velocity profile starts flattening which can be interpreted as the distinguish between an inner and an outer layer. Further analyzing these

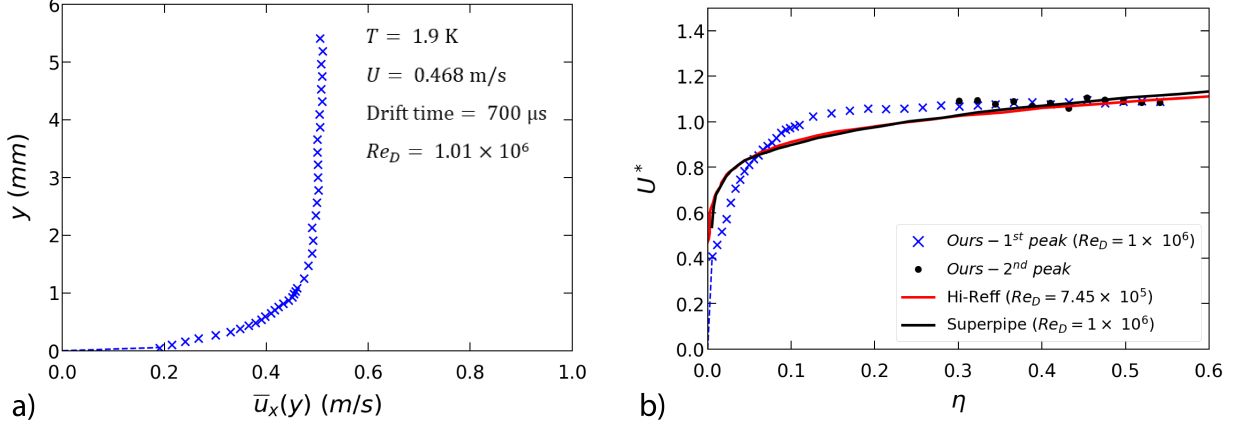


Fig. 6.5: (a) A representative mean velocity profile in He II at 1.9 K, where $U=0.468$ m/s and $Re_D = 1.01 \times 10^6$. The scaling of the near-wall region is clearly captured. The spatial resolution is $55 \mu m$. (b) The $U^*(\eta)$ velocity profile for recent experiments, both for the main and the second peak, and data from literature including Superpipe [46] and Hi-Reff [4]

velocity profiles will indeed have provided an unprecedented insight into the existence of a unique law of the wall in He II.

Fig. 6.5(b) shows the $U^*(\eta)$ velocity profile for the same measurement where $U^* = \bar{u}/U$ and $\eta = 2y/D_h$. The data can be compared against the data from literature including Superpipe [46], and Hi-Reff [4] at approximately similar Re_D . We can estimate the average velocity U using the one dimensional integration of the mean velocity profile. The result is in good agreement with the exact average velocity U calculated from bellows geometry. This integration is defined as:

$$U = \frac{1}{A} \iint_A \bar{u} \cdot dA \approx \frac{1}{D} \int_0^D \bar{u} \cdot dy \quad (6.5)$$

Additionally, a solid agreement between the mean velocity obtained by the first peak (blue crosses) and the second peak (solid black circles) is evident in Fig. 6.5(b). This is of great significance for showing the fact that our MTV method has a sufficiently small spatial resolution to capture the coherence structure of turbulence in these Reynolds numbers. The agreement between profiles acquired from two completely different drift times ($700 \mu m$ and $1700 \mu m$) show the averaging effect in our measurements is negligible and the turbulence fine scale is sufficiently captured. In turbulence research, $\Lambda = \bar{u}_{max}/U$ is also a useful coefficient that implies how close a turbulent velocity profile is to that of a potential flow. We calculate $\Lambda \approx 1.07$ at ($Re_D = 10^6$) which is in good agreement with the value of 1.05-1.14 in literature [88].

6.2 Friction Factor in He II pipe Flows

Friction velocity as an important constitute of the law of the wall region is directly related to friction factor through Eq. 3.2. In our analysis, we determine the friction factor based on the most relevant experimental data in literature. The uncertainty associated with the friction factor is evaluated and propagated into the subsequent analysis.

6.2.1 Classical and Non-classical Friction Factor Data

In classical turbulent pipe flow research, some of the most reliable friction factor correlations in a wide range of $10^4 \lesssim Re_D \lesssim 10^7$ for smooth pipes are given by Japan HI-Reff (equation(16) in [10]) and a collaboration between Princeton Superpipe and Oregon High Re facility (equation(1) in [89]). The mathematical form of these correlations is directly derived based on the the law of the wall equation. We have compiled the major body of friction factor data in classical turbulent pipe flow research which is shown in Fig. 6.6. The data can be compared versus the given friction factor correlations including the Superpipe correlation, Hi-Reff correlation and Kármán-Nikuradse equation. Although the difference between the major datasets suggest some slight differences, it would be safe to claim that the data collapses reasonably for classical fluids. In Fig. 6.6, we have

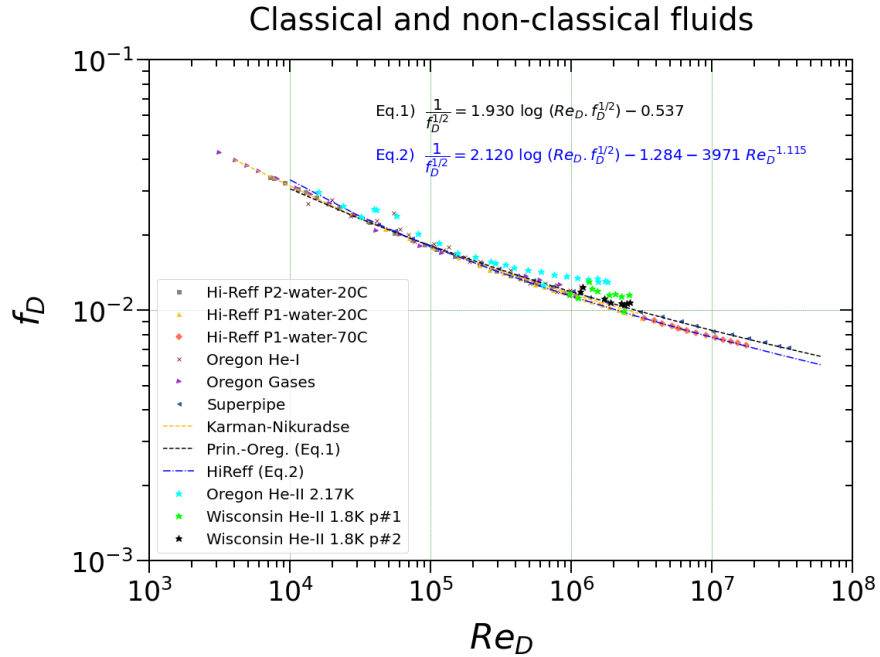


Fig. 6.6: The major body of friction factor data in literature in both classical and non-classical pipe flow [3, 4, 46, 89–91]. The Princeton-Oregon and Hi-Reff correlations are given.

also included the He II friction factor data shown by star data points so a comparison can be made. The He II data will be explained further in the following discussion.

On the other hand, there are very limited friction factor datasets in He II pipe flow [53, 90, 91]. The data obtained in the Oregon High Re facility in He II was measured using the same facility as they measured the classical data with a wide range of classical fluids. Since the classical data was obtained using the same analysis technique and perfectly matches the Superpipe data, we expect their He II data to be of the same quality. Note that the relative roughness of Oregon pipe and our flow pipe is in the order of 10^{-6} to 10^{-5} . Therefore, the Oregon data should be one of the most reliable datasets to be used for our experiments. The data obtained by Wisconsin Group [91] is also in the same Re_D range and has similar wall relative roughness. They use a similar measuring technique as the Oregon facility and the measurements are systematically done for different pipes lengths. Their results collapse closely on the Oregon data. Therefore, we use these 3 datasets as our major sources in evaluating the friction factor in our flow pipe. The exact same datasets were also emphasized in an earlier experimental pipe flow experiment using LHFVF [44]. This data is redrawn in Fig. 6.7. The Oregon measurements were reproduce within experimental error [90]. The Wisconsin group also carefully calibrated their flow rate measurements and avoided bellows speeds that exceed the gear drive torque limits all in order to minimize the experimental errors [91]. Note that our flow pipe is smooth, isothermal, and free of entrance effects, so assuming friction

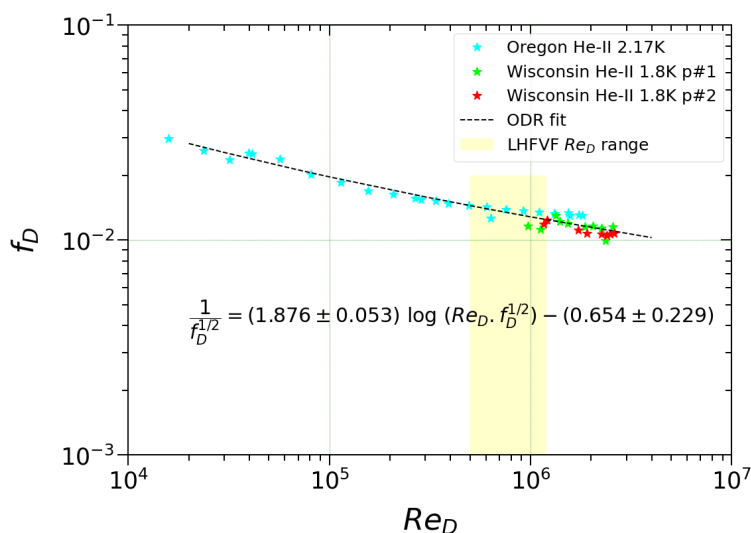


Fig. 6.7: Friction factor data for non-classical pipe flow [90, 91] at similar conditions to those of our flow pipe. He II correlation fitted on the data using ODR with a similar format to that of the Prandtl global relationship.

factor only as a function of Reynolds number is valid [28]. In Fig. 6.7, the range of Re_D in our experiments are highlighted in yellow.

We do note that the temperature at which the source data is acquired is different from our experiments. Since the superfluid properties varies significantly with temperature, a question is the validity of the data applied to our temperature. However, one should note that the source datasets are obtained at different temperatures but they show a good agreement and suggest the same behavior. Therefore, using the friction factor obtained at other temperatures (1.8 and 2.17 K) applied to our experimental temperature (1.9 K) which lays within the source temperature range should be a valid procedure.

6.2.2 He II Friction Factor Correlation

To use the He II friction factor data in our experiments, a reliable curve fit to the data is needed. The data falls close to the classical correlations, thus we use the same mathematical form. Since these correlations are in an implicit form, we optimize the fitting coefficients using the orthogonal distance regression (ODR) method via Python Scipy.odr package. The algorithm essentially optimizes the orthogonal distances between the data points and the fit to minimize the summation of the square of the random error associated with the independent and dependent variables. This method is thoroughly compared versus the ordinary least square and quite often shows supremacy [92]. The obtained fit and the uncertainty of the fitting coefficients are computed and shown versus the datasets in Fig. 6.7 and is given in Eq. 6.6.

$$\frac{1}{\sqrt{f_D}} = (1.876 \pm 0.053) \log \left(Re_D \sqrt{f_D} \right) - (0.654 \pm 0.229), \quad (6.6)$$

6.2.3 Effects of the Non-circular Flow Pipe

Since the cross-section area of the flow pipe is a square, naturally a question may be raised about the induced effects of such geometry in comparison to the conventional circular pipe and its governing equations, and the validity of the hydraulic diameter. Several studies [93, 94] show that the law of the wall in rectangular pipes should be very close to circular pipes and it only slightly varies when the height to width ratio is larger than 7-12. Even in the highly anisotropic cases, the classical von Kármán constant approaches to $\kappa \simeq 0.37$ for infinite channels, versus the well-established value of $\kappa = 0.384$ for turbulent boundary layer, and $\kappa = 0.37$ -0.42 for circular pipes [37]. The corner effects of our flow pipe must be also negligible since the flow pipe width is much larger than the log region thickness as we show later $D_h \simeq 20\delta$ in this chapter. There are

also limited studies that suggest the friction factor in He II in non-circular passages may also be correlated by pipe correlations based on the Reynolds number [53].

However, we would like to correct the use of hydraulic diameter to the second order. Studies [95] show that simply using hydraulic diameter or any arbitrary length scale might not be an accurate way to represent non-circular passages. Indeed many of the proposed approaches do not entail a concrete physical basis or only rely on the laminar region hoping that the same treatment is still applicable to the turbulent region [95]. A more sophisticated approach for reducing the non-circular data has been proposed by Obot [96]. This approach is particularly useful because it reviews the majority of the previous approaches and considers their strengths. Then it successfully applies its method to collapse the non-circular data in literature on the pipe correlations. More importantly, this method provides a relevant physical basis which is derived from the laminar to turbulent transition. To use this correction, we first define reduced Reynolds number Re_r and reduced friction factor f_r as:

$$Re_r = \psi_{Re} \cdot Re_n, \quad (6.7)$$

$$f_r = \psi_f \cdot f_n, \quad (6.8)$$

where the reduction coefficients are defined as:

$$\psi_{Re} = \frac{Re_{c,cr}}{Re_{n,cr}}, \quad (6.9)$$

$$\psi_f = \frac{f_{c,cr}}{f_{n,cr}}, \quad (6.10)$$

The subscripts f , r , c , n , and cr denote Darcy friction factor, reduced, circular, non-circular, and critical (transition from laminar to turbulent), respectively. The critical values, $Re_{n,cr}$ and $f_{n,cr}$ of square flow passages are given by [97] which were experimentally measured equal to 2147 and 0.00798, respectively. On the other hand, the well-established critical values of $Re_{c,cr}$ and $f_{c,cr}$ for circular pipes in literature [96] are equal to 2100 and 0.008, respectively. Therefore, the reduction coefficients for the LHFVF 20×20 mm² square flow pipe are calculated as $\psi_{Re} = 0.9781$ and $\psi_f = 1.0025$. These values suggest negligible deviations of the reduced Reynolds number and reduced friction factor for our square flow flow. We use these values to correct our data for the effect of a non-circular pipe. The Friction factor datasets were obtained in experiments using circular pipes. We first use the Reynolds reduction coefficient ψ_{Re} to find the Reduced (equivalent circular) Re_D . The typical reduced Reynolds numbers in our experiments are calculated as 9.88×10^5 and

1.18×10^6 . We substitute these values in our He II friction factor correlation where the reduced friction factor can be determined. Eventually, we convert the reduced friction factor back to the real non-circular value using ψ_f^{-1} . The friction factor of 0.0128 and 0.0124 are calculated for the associated Reynolds numbers, respectively.

6.3 Obtaining Law of the Wall in Superfluid Helium

The friction velocity in our He II turbulent flows can be obtained via combining Eq. 3.2 and Eq. 6.6 at each Re_D . On the other hand, the mean velocity profile and real wall coordinate were obtained in Section 7.1.2, and the kinematic viscosity of helium is known as a function of temperature. Thus all the key components for dimensional analysis of our He II mean flow velocity profile as a function of the wall normal coordinate are present.

Using the dimensionless variable, the velocity profiles acquired in Section 7.1.2 can be reconstructed to obtain the the wall velocity profile. Such profile is shown in Fig. 6.8 for a typical experiment at 1.9 K, $U=0.468$ m/s and $Re_D = 1.01 \times 10^6$. The real wall coordinate on the top

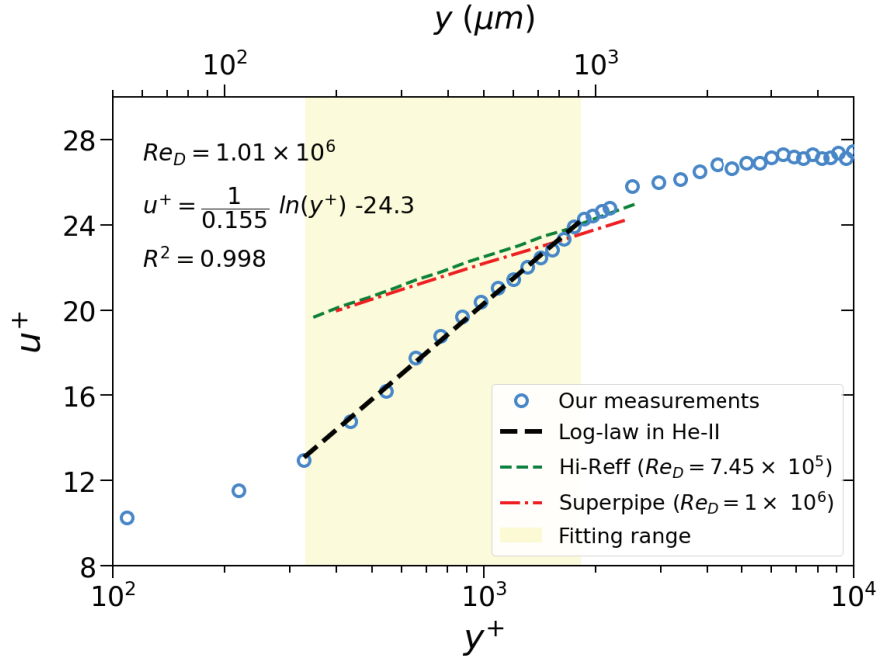


Fig. 6.8: Representative results for wall velocity u^+ as a function of dimensionless wall coordinate y^+ in He II at 1.9 K where $U=0.468$ m/s and $Re_D = 1.01 \times 10^6$. A strong logarithmic scaling exists from $y^+ = 330$ to $y^+ = 1800$ which shows a good agreement with the classical turbulence range. Least squares method is used for the fit to determine the von Kármán and additive constants. Superpipe [46] and Hi-Reff [4] classical data is shown for comparison.

axis and the dimensionless wall coordinate on the bottom axis are shown. The friction factor is calculated $f_D = 0.0128$ thus, the friction velocity is calculated $u_\tau = 0.0188$ m/s. Interestingly, it can be seen that after the first few data points, a logarithmic region is evident in all the carried out experiments. This region typically starts from around $y^+ = 400$ and extends to about $y^+ = 2000$, where it finally deviates rapidly from the log scaling. Our experiments show the independence of the log scaling from the average velocity and the drift time. These findings shed the first light on the existence of the law of the wall in He II turbulent pipe flow.

The classical results are also shown in Fig. 6.8 for a comparison with our He II results. As it can be seen, the slope of the He II law of the wall is steeper than the classical law of the wall data [4, 46]. This also causes the He II profile to have a much lower intercept with the vertical axis, i.e., the additive constant B . In Section 3, we mentioned that the law of the wall starts at $y^+ = 400 - 600$, for Hi-Reff and Superpipe, respectively. The upper limit in the Superpipe experiment is given by $y^+ = 0.12Re_\tau$, which translate to $y^+ = 2396$ at $Re_D = 10^6$. If we use these classical calculations for our flow pipe, an upper limit of about 1.2 mm at $Re_D = 10^6$ is achieved. These calculations for our flow pipe are summarized in Table 3.1 at different average velocities. It turns out our lower and upper limits are in a good agreement with the classical data.

Table 6.1: Flow parameters and calculated log-law range based on classical relationships

Flow parameters					Wall coordinate		Real coordinate	
U	Re_D	f_D	u_τ	Re_τ	y_{min}^+ [10]	y_{max}^+ [30]	y_{min}	y_{max}
(m/s)	(-)	(10^{-2})	(10^{-2} m/s)	(-)	(-)	(-)	(μ m)	(mm)
0.3	6.48×10^5	1.383	1.247	13465	400	1600	297	1.2
0.4	8.64×10^5	1.316	1.622	17512	400	2100	228	1.2
0.5	1.08×10^6	1.267	1.990	21480	400	2600	186	1.2
0.6	1.30×10^6	1.229	2.352	25387	400	3100	158	1.2

6.3.1 Quantitative Determination of Law of the Wall Fitting Range

To quantitatively determine the limits of the logarithmic region in superfluid He II, we define the Φ function as was proposed by Hi-Reff group [10] which is given by:

$$\Phi = u^+ - \frac{\ln(y^+)}{\kappa} - B, \quad (6.11)$$

We expect the Φ function to approach to zero in the log region. we first preform the fit in an initial range and find the constants. These constants are used to construct the Φ function where we

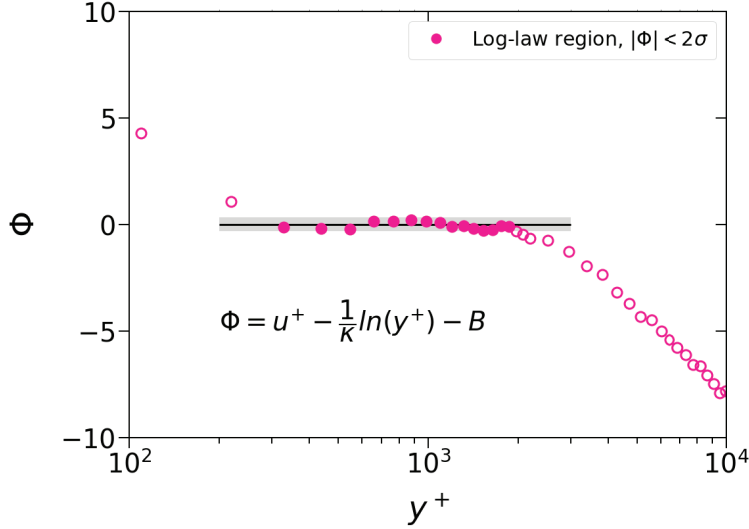


Fig. 6.9: Quantitative determination of the linear region using Φ function where the lower and upper limits of about $y^+ = 400$ and $y^+ = 2000$ are consistent throughout the experiments.

use a searching algorithm to find a region where all data points lay within the 2-standard deviation band. If 3 data points in sequence fall outside the 2-standard deviation band, the boundary is determined to be the last valid point. The new range is used to update the fit and the fitting coefficients. As a consequence, through this iterative process the fitting range is converged. The results of this procedure is shown in in Fig. 6.9. The logarithmic fit to our experimental data in Fig. 6.8 using LSM is performed in the range acquired with this method and is shown in a yellow highlight.

6.3.2 Law of the Wall Fitting Parameters in He II

As it can be seen in Fig. 6.8, the von Kármán constant in He II as our first fitting coefficient of the log region is determined 0.155. The von Kármán constant shows a remarkable consistency through the experiments and in 2 different Re_D around the typical values of 0.15-0.16. The value falls much below the conventional classical value of 0.37-0.42. The significant difference between the classical and superfluid data is of great fundamental and engineering significance which will was discussed in Chapter 3 and will be commented further in Section 6.4.

The additive constant in He II as the second fitting coefficient of the log region is determined -24.3. Clearly, the additive constant is very sensitive to the choice of von Kármán constant. When we determine B with a corresponding fixed value of κ , the results show a great coherence. This procedure was previously used on the Princeton Superpipe data [28]. The negative value for B

comes from the fact that the additive constant is simply a fitting coefficient and since the slope of the law of the wall in superfluid is much sharper, the intercept of the wall velocity coordinate falls in the negative domain (see Fig. 6.8).

6.4 Discussion

The mutual friction tends to couple the two fluids in He II flows [53]. The greater the relative motion of the two fluids is, a greater mutual friction will be resulted. Due to the extremely high velocity gradient in NVP in He II, the mutual friction might not be able to fully couple the fluids near the wall. Therefore, the mismatch in velocity profile results in a finite mutual friction force that can affect the velocity profile of the normal fluid. This is the origin of the observed difference between the classical and He II law of the wall.

Law of the wall is one of the most researched topics in turbulent pipe flow. One can argue that the law of the wall alone can give a good estimation of the entire velocity profile in turbulent pipe flow [28]. That is also why friction factor correlations based on the law of the wall are astonishingly accurate in comparison to their simplicity. The future design of He II pipe systems including the transfer lines and the turbomachinery systems can be optimized by knowing such velocity profile in He II. Furthermore, κ value is a critical parameter in computational simulation of turbulence. It can be argued that the complexity of the numerical studies in He II is partially due to the lack of experimental data. Such data can help the design of the future numerical research in He II. We hope that our results encourage further theoretical and experimental investigations in this field that can expand our knowledge of turbulent pipe flow and the quantum turbulence as a whole.

CHAPTER 7

RESULTS AND UNCERTAINTY ANALYSIS

In this chapter, we apply the data analysis procedure discussed in the previous chapter to all of the datasets acquired in our experiments. We are interested to evaluate the repeatability of our results in various experimental trials. In the previous chapter, we showed that the law of the wall fitting coefficient in He II are completely different from those of the classical fluids. These results are the first of their kind, thus there is no experimental or numerical data to compare with them. Naturally, we would need to analyze the error associated with our measurements and results to answer whether this difference is due to the experimental errors or new physics. For this purpose, we have carefully identified all of the uncertainty sources in our experiments. Then we calculate the error in each relevant physical parameter and propagated the error to the final results methodically.

7.1 Uncertainty Analysis of the Law of the Wall in He II

The first step in an uncertainty analysis is to identify the source of uncertainty. The goal of our experiments is to fit the law of the wall given in Eq. 3.1 and determine the two fitting coefficients. Therefore, any physical parameter involved in the calculation of this fit is a relevant parameter and any uncertainty in measuring or calculating a relevant parameter is a source of uncertainty. To fit

Eq. 3.1, we need to determine the relevant physical parameters as follows:

$$y = \Omega (Y - Y_0), \quad (7.1)$$

$$\bar{u}_x(y) = \frac{[X_d(y) - X_b(y)] \Omega}{\delta t}, \quad (7.2)$$

$$\Omega = \frac{D}{b_2 - b_1}, \quad (7.3)$$

$$u_\tau = U \sqrt{\frac{f_D}{8}}, \quad (7.4)$$

$$U = \frac{v \times A_{\text{bel}}}{A_{\text{ch}}}, \quad (7.5)$$

$$v = \frac{dh(t)}{dt}, \quad (7.6)$$

$$\frac{1}{\sqrt{f_D}} = (1.876 \pm 0.053) \log \left(Re_D \sqrt{f_D} \right) - (0.654 \pm 0.229), \quad (7.7)$$

$$Re_D = \frac{UD_h}{\nu}. \quad (7.8)$$

Eq. 7.1-8 contain all of the involved measurements in our experiment. Any error in these measurements is a source of uncertainty and will propagate in the final results of the law of the wall coefficients. These measurements include:

1. The location of the tracerline in pixel plane (x, y)
2. The location of the solid boundaries
3. The bellows pump velocity, v

We also calculate the friction factor f_D based on the He II friction factor correlation which is subject to uncertainty. Note that in our experiments, the drift time is set by the internal settings of the laser systems and the uncertainty is negligible (less than 0.001%). Additionally, the temperature variations in our experiments is less than 1 mK and therefore, the uncertainty in the kinematic viscosity of He II is also negligible.

7.1.1 Evaluation of the Uncertainties

Step-by-step, we carefully propagate the error in each measurement into the next relevant parameter. In most cases, we derive the propagation formula analytically based on the relevant equations. If needed, we also use the Monte-Carlo perturbation method [98] or programming packages to calculate the uncertainty. In the end, we calculate the error in the determination of the law of the wall coefficients. These analyses have indeed resulted in introducing the von Kármán and additive constants in He II, κ_s and B_s , respectively.

In these analyses, we evaluated the error equal to one standard deviations σ around the arithmetic mean μ where σ is defined as:

$$\sigma = \frac{\left[\sum_{i=1}^n (\mu - x_i)^2 \right]^{0.5}}{\sqrt{n-1}}, \quad (7.9)$$

such that x_i denotes each measurement and n is the total number of measurements. μ is defined as:

$$\mu = \frac{1}{n} \sum_{i=1}^n x_i, \quad (7.10)$$

Based on the rules of propagation for standard deviation, the variation of function $f(\sigma_1, \sigma_2, \dots, \sigma_k)$ is calculated using:

$$\langle \Delta f^2 \rangle = \sum_{n=1}^k \left| \frac{\partial f}{\partial \sigma_n} \right|^2 \langle \Delta \sigma_n^2 \rangle \quad (7.11)$$

where the variables are all independent and the variation in them is their associated standard deviation.

7.1.2 Uncertainty in Location of Tracerline

The general methodology in analyzing the uncertainty of MTV images is explained by Hill and Klewicki [80] which is the base of our analysis. The uncertainty in the image processing techniques arise due to assigning a mathematical coordinate to the image pixels that have finite dimensions. The Gaussian fit to the tracerline light intensity function in each binning bar is calculated using Python Scipy.optimize.curve_fit package where the standard error in the fitting coefficients including the mean and standard deviation can be calculated. The Gaussian fits are give by:

$$G = (a \pm \Delta a) e^{-\frac{(x-(m \pm \Delta m))^2}{2(\sigma \pm \Delta \sigma)^2}} \quad (7.12)$$

where a is the height of the curve's peak, m is the position of the center of the peak i.e., the mean, and σ is the standard deviation (34.1% probability width). We fit these Gaussian functions at evenly spaced y locations as was described in Section 7.1.2. The standard error of the mean values of the Gaussian fit Δm is the uncertainty of the tracerline location in the streamwise direction. The uncertainty in the wall normal direction is also of the same order [80]. We methodically determine the fitting range of the Gaussian fit in each binning bar by minimizing Δm . Therefore, by analyzing each baseline or driftline image, we obtain the x location of the tracerline at each y location and their associated uncertainties.

The baselines are straight lines in undisturbed He II (see Chapter 6). Therefore, we fit a line to the pixel locations of each baseline (i.e., the peak point of Gaussian fits) using LSM as $X_b = ay + b$ where a and b are linear fitting coefficients. For this treatment, we can define the overall error in the baseline location which depends on the scattering of the peak points around the fit as well as the error in each individual peak point. For this purpose, we can derive a general formula for calculating the overall error of a function fit to a set of data points with the associated uncertainties based on the definition of the standard deviation. Assuming a set of data points as $\bar{x}_i + \Delta x$, where Δx can be a negative or positive value and the mean of the data points is given as $\bar{\bar{x}}$, the overall error of the mean can be calculated as:

$$\Delta\bar{\bar{x}} = \sqrt{\frac{1}{n} \sum_{i=1}^n (\bar{x}_i + \Delta x - \bar{\bar{x}})^2} = \sqrt{\bar{\sigma}^2 + \frac{1}{n} \sum_{i=1}^n (\Delta x)^2}, \quad (7.13)$$

where $\bar{\sigma}$ is the standard deviation of the data points around the mean $\bar{\bar{x}}$. Using Eq. 7.13, the overall error in the baseline location can be calculated as:

$$\Delta X_b = \sqrt{\bar{\sigma}^2 + \frac{1}{n} \sum_{i=1}^n (\Delta m_{b,i})^2} = \sqrt{\frac{1}{n} \sum_{i=1}^n \{(m_{b,i} - ay_i - b)^2 + (\Delta m_{b,i})^2\}} \quad (7.14)$$

where n is the total number of binning bars, and $m_{b,i}$ are the peak of the Gaussian fits. ΔX_b for a typical baseline image is calculated about 1.3 pixels.

Uncertainty in pixel size:

Calculating the pixel size depends on the determination of the solid boundaries which was explained in Section . The error in the intercept (second fitting coefficient) of the linear fits is the uncertainty in the pixel location of the solid boundaries. We use Python Scipy.optimize.curve_fit package to calculate the fit errors which uses nonlinear LSM. The uncertainty in the intercept for the bottom and top fits is typically in the range of (0.03-0.06) and (0.45-0.70) pixels, respectively. The top window is usually harder to illuminate because of its location and has a highly transparent surface so the uncertainty in its location is larger. Applying Eq. 7.11 to Eq. 7.3, one can calculate the uncertainty in pixel size as:

$$\frac{\Delta\Omega}{\Omega} = \sqrt{\left(\frac{\Delta b_2}{b_2 - b_1}\right)^2 + \left(\frac{\Delta b_1}{b_2 - b_1}\right)^2} \quad (7.15)$$

As a result, the uncertainty in the pixel size for a typical background image is calculated as $\Omega = 10.935 \mu\text{m}/\text{pixel} \pm 0.004$ (0.04%).

Uncertainty in y location and streamwise mean flow velocity:

Applying Eq. 7.11 to Eq. 7.1, the error in the y location is calculated using:

$$\Delta y = \sqrt{(Y\Delta\Omega)^2 + (\Omega\Delta Y_0)^2 + (Y_0\Delta\Omega)^2}, \quad (7.16)$$

On the other hand, the uncertainty in the streamwise mean velocity can be calculated by applying Eq. 7.11 to Eq. 7.2 which yields:

$$\frac{\Delta\bar{u}_x(y)}{\bar{u}_x(y)} = \sqrt{\left(\frac{\Delta X_d}{X_d - X_b}\right)^2 + \left(\frac{\Delta X_b}{X_d - X_b}\right)^2 + \left(\frac{\Delta\Omega}{\Omega}\right)^2} \quad (7.17)$$

Where $X_d - X_b = \delta X$ is the drift distance in pixel unit. As a consequence of the above derivations, we can associate each (y, \bar{u}_x) pair with its uncertainty. We scan the tracerlines along the wall normal direction up to 3 mm to cover beyond the near-wall region. The velocity profile and the associated uncertainty is shown in Fig. 7.1(b) for a typical experiment where $U = 0.468$ m/s and $Re_D = 1.01 \times 10^6$. Note that the error bars are 2D bars containing error information in both mean velocity and the y location (the vertical bars are small and harder to see).

We double-check our derivations using the Monte-Carlo perturbation simulation and indeed obtain similar results. In the Monte-Carlo simulation, we randomly perturb all the involved independent variables including y location, pixel size, baseline location and driftline location within their uncertainty range using a Gaussian random generator. As an instance, the results of a representative Monte-Carlo simulation with 10^4 random perturbations for the mean velocity at $y = 0.49$

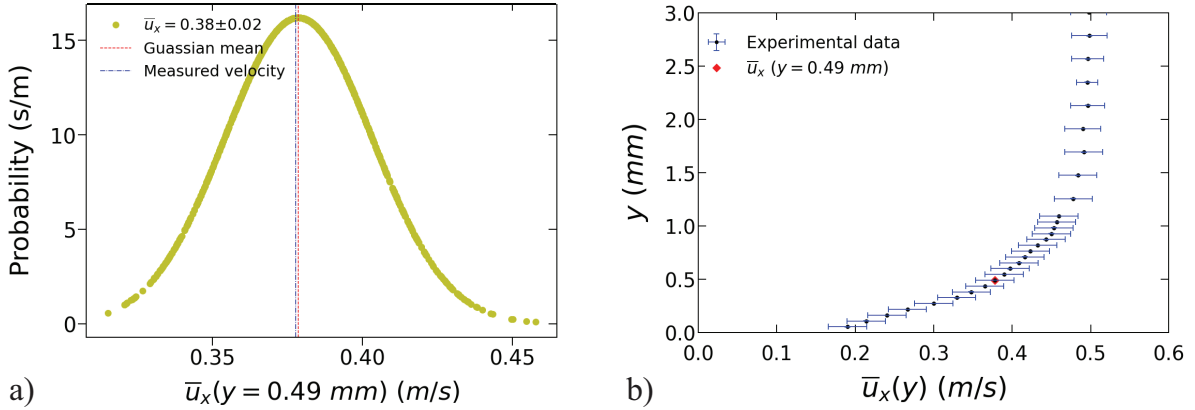


Fig. 7.1: (a) Mean velocity PDF at $y = 0.49$ mm when involved parameters are perturbed within their error using a Monte-Carlo simulation with 10^4 perturbations. (b) Scanning the y location extending to 3 mm to acquire the velocity profile and associated uncertainty for a representative experiment where $U=0.468$ m/s and $Re_D = 1.01 \times 10^6$. The error calculated using derivations and the Monte-Carlo method are similar and can be compared at $y = 0.49$ mm as a representative.

mm away from the bottom wall is shown in Fig. 7.1(a). We calculate the error in the mean velocity at $y = 0.49$ mm as the standard deviation of the probability density function (PDF) of the 10^4 perturbed values. The PDF has a Gaussian-like behavior and the mean is in agreement with the measured value for the mean velocity at that location. The computations were repeated with 10^3 or 10^5 random perturbed values and the results were self-consistent.

Bellows velocity:

Typical bellows movements in He II experiments were shown in Fig. 4.6. The error in the bellows velocity as a fitting coefficient of the displacement data is calculated for the constant velocity region Δt_C during the experimental time as $h(t) = (-v \pm \Delta v)t + (H_0 + \Delta H_0)$. We calculate the bellows velocity in a typical compression as $v = 5.0845$ mm/s \pm 0.0002 (0.004%) where the magnitude of the relative error remains constant in different trials.

Average velocity:

We derived an exact expression for the bellows instantaneous volumetric flow rate in Section 4.2.3. Therefore, by applying Eq. 7.11 to Eq. 7.5, the average velocity U and its associated uncertainty for any given bellows velocity and any bellow vertical location can be calculated using:

$$\Delta U = \sqrt{\left(\frac{A_{\text{bel}}}{A_{\text{ch}}}\right)^2 \Delta v^2} \quad (7.18)$$

For instance, we calculate the average velocity for representative tracerline images acquired while the bellows was 5 cm compressed equal to $U = 0.46843$ m/s \pm 0.00002 (0.004%) at $Re_D = 1.01 \times 10^6$ and $U = 0.56156$ m/s \pm 0.00002 (0.004%) at $Re_D = 1.21 \times 10^6$. Note that the error at other bellows velocities and locations is calculated similarly.

Reynolds number:

Applying Eq. 7.11 to Eq. 7.8, the error in Re_D is calculated using:

$$\Delta Re_D = \sqrt{\left(\frac{D_h}{\nu}\right)^2 \Delta U^2} \quad (7.19)$$

The error is analyzed as $Re_D = 1,011,400 \pm 40$ (0.004%) for $U = 0.468$ m/s and $Re_D = 1,212,500 \pm 50$ (0.004%) for $U = 0.562$ m/s.

Friction factor:

The uncertainty of the friction factor data is not published in the sources [90, 91]. We calculate the uncertainty in the friction factor by applying Eq. 7.11 to Eq. 7.7 which gives:

$$\langle \Delta f_D \rangle = \sqrt{\left|\frac{\partial f_D}{\partial a}\right|^2 \langle \Delta a^2 \rangle + \left|\frac{\partial f_D}{\partial b}\right|^2 \langle \Delta b^2 \rangle + \left|\frac{\partial f_D}{\partial Re_D}\right|^2 \langle \Delta Re_D^2 \rangle} \quad (7.20)$$

where a and b are the fitting coefficients and their uncertainty was previously calculated in Section 6.2. Since the source data is obtained in circular pipes, we also use the discussion provided in Section 6.2.3 to apply the circular data reduction and the uncertainty is accordingly calculated. The derivatives in Eq. 7.20 are calculated implicitly at the mean values (a^* , b^* , $\psi_{Re} \cdot Re_D^*$, and $\psi_f \cdot f_D^*$). The friction factor and the associated uncertainty after converting them back to square data is calculated as $f_D = 0.0128 \pm 0.0009$ (7.03%) for $Re_D = 1.01 \times 10^6$ and $f_D = 0.0124 \pm 0.0009$ (7.26%) for $Re_D = 1.21 \times 10^6$.

Friction velocity:

applying Eq. 7.11 to Eq. 7.4, we can calculate the uncertainty in the friction factor using:

$$\frac{\Delta u_\tau}{u_\tau} = \sqrt{\left(\frac{\Delta U}{U}\right)^2 + \left(0.5 \frac{\Delta f_D}{f_D}\right)^2} \quad (7.21)$$

Therefore, the friction velocity is calculated as $u_\tau = 0.0187 \pm 0.0007$ (3.74%) for $Re_D = 1.01 \times 10^6$ and $u_\tau = 0.0221 \pm 0.0008$ (3.62%) for $Re_D = 1.21 \times 10^6$.

7.1.3 Uncertainty of wall velocity profile and the logarithmic fitting

In the above analysis, we calculated the uncertainty in the key components of the dimensionless wall velocity profile. As a consequence, we can apply Eq. 7.11 to Eq. 3.1 to calculate the uncertainty in the wall velocity using:

$$\frac{\Delta u^+}{u^+} = \sqrt{\left(\frac{\Delta \bar{u}_x(y)}{\bar{u}_x(y)}\right)^2 + \left(\frac{\Delta u_\tau}{u_\tau}\right)^2} \quad (7.22)$$

and the uncertainty in the wall normal coordinate using:

$$\frac{\Delta y^+}{y^+} = \sqrt{\left(\frac{\Delta y}{y}\right)^2 + \left(\frac{\Delta u_\tau}{u_\tau}\right)^2} \quad (7.23)$$

The results of wall velocity profile uncertainty analysis for a typical experiment of $U = 0.468$ m/s and $Re_D = 1.01 \times 10^6$ are shown in Fig. 7.2(a) where the errors are shown using the error bars.

At this stage, we have calculated the uncertainty in the involved components of Eq. 3.1. Therefore, we can calculate the uncertainty in the fitting coefficients of the law of the wall region. To Establish a comprehensive analysis of the uncertainty in the von Kármán constant κ_s and the additive constant B_s in He II, we use a Monte-Carlo perturbation simulation. With a similar procedure as described in Section 7.1.2, we generate 10^3 randomly perturbed wall velocity profiles within the error ranges using Python Numpy.random.normal package. Next, we can fit the log law formula to each individual perturbed wall velocity profile. The results of the 10^3 fits are shown in Fig. 7.2(b)

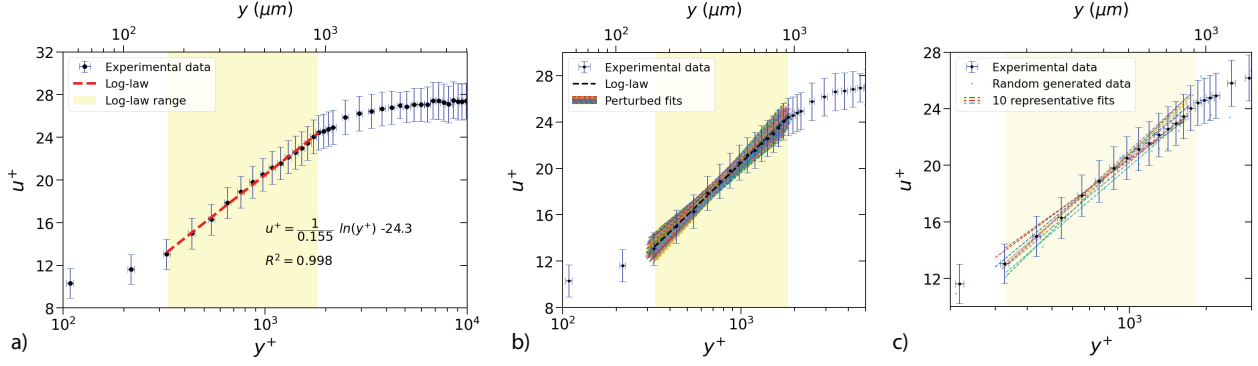


Fig. 7.2: (a) Scaling of the overlap region for a representative flow of $U = 0.468$ m/s and $Re_D = 1.01 \times 10^6$. Experimental data, the calculated error, and the linear fit to the experimental data are shown. (b) Monte-Carlo simulation of 1000 linear regressions within the log-law range from $y^+ = 330$ to $y^+ = 1800$, fit to the random data generated within the standard error of the wall velocity profile. The fits are achieved using least squares method. (c) 10 representative linear fits around the experimental data for a closer look at individual perturbations.

where the coherence of the fits around the mean fit (black dashed line) is evident. For a closer look, 10 randomly chosen fits are also shown in Fig. 7.2(c).

The fits essentially contain 10^3 values for κ_s and B_s for each experimental trial. We show the distribution of the values on a PDF where the mean value and the error for κ_s and B_s can be obtained. The results are shown in Fig. 7.3(a) and (b), respectively. The distribution is Gaussian-like and the mean and the error are calculated as $\kappa = 0.154 \pm 0.010$ (6.49%) and $B = -23.3 \pm .2$ (0.95%). Note that the mean values acquired as a result of this treatment are in good agreement with the values acquired from the mean fit.

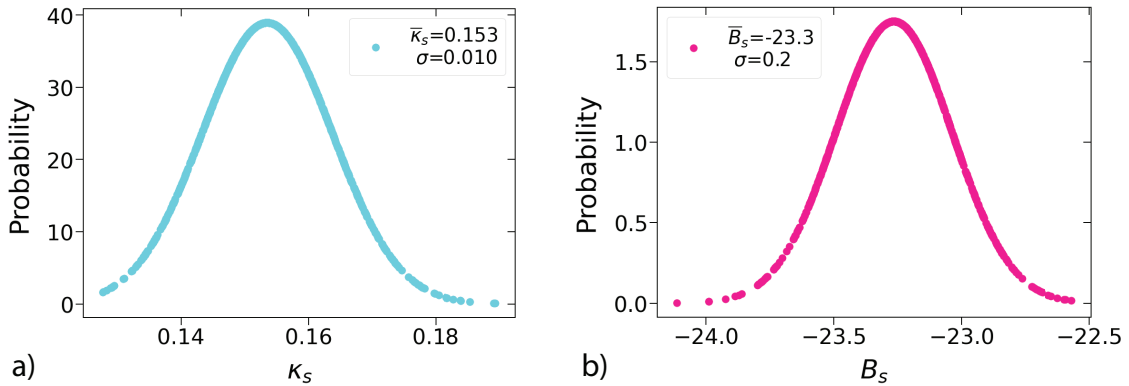


Fig. 7.3: Representative PDF of (a) von Kármán constant and (b) additive constant as results of the 1000 fits to the perturbed wall velocity profiles as a result of the Monte-Carlo simulation. The means and the errors are shown.

7.1.4 Fitting constants of the law of the wall in He II

It is desirable to make a comparison between different experimental trials in identical conditions. We compile the data acquired from experimental trails at $U=0.47$ m/s and 0.56 m/s ($Re_D = 1.01 \times 10^6$ and $Re_D = 1.21 \times 10^6$, respectively) in separate frames. The results are shown in Fig. 7.4 and Fig. 7.5 and indicate a remarkable coherence of the constants. Additionally, the difference between the mean values at different velocities remain within the overall error of the mean values. As the final results of our pioneering experiments, $\kappa_s = 0.160 \pm 0.015$ and $B_s = -23.2 \pm 0.4$ for $Re_D = 1.01 \times 10^6$ and $\kappa_s = 0.154 \pm 0.010$ and $B_s = -24.0 \pm 0.4$ for $Re_D = 1.21 \times 10^6$ are reported.

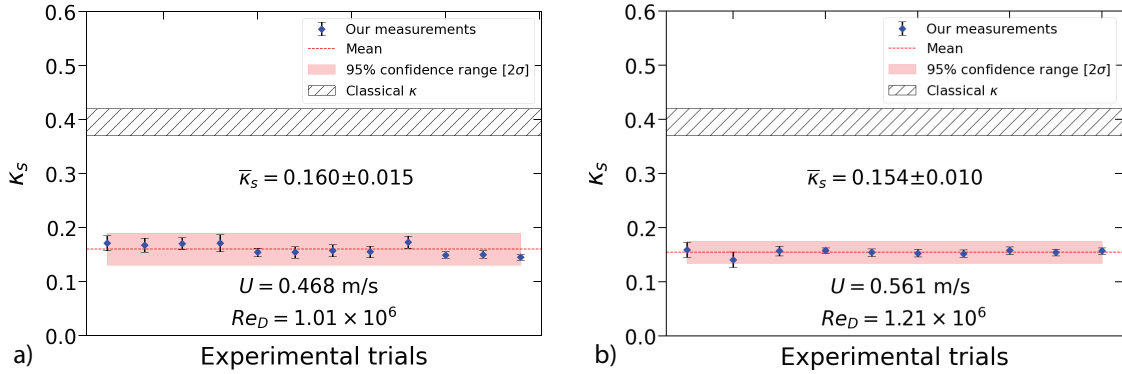


Fig. 7.4: Results of the law of the wall experiment in He II at 1.9 k and the overall error of the von Kármán constant for identical-condition experiments. Classical value is shown for comparison. (a) $U=0.47$ m/s and $Re_D = 1.01 \times 10^6$. (b) $U=0.56$ m/s and $Re_D = 1.21 \times 10^6$.

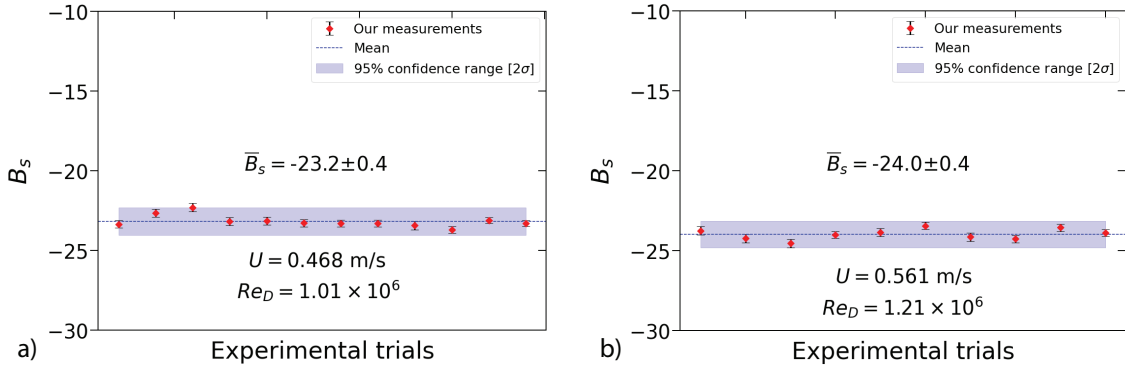


Fig. 7.5: Results of the law of the wall experiment in He II at 1.9 k and the overall error of the additive constant for identical-condition experiments. (a) $U=0.47$ m/s and $Re_D = 1.01 \times 10^6$. (b) $U=0.56$ m/s and $Re_D = 1.21 \times 10^6$.

7.1.5 Discussion

The tracerline quality near the wall was one of the sources of uncertainty in our measurements. During the testing experiments, we successfully showed that optimizing the FS beam key parameters, drift time, number of superimposed snapshots, and the MTV acquisition frequency can strongly affect and improve the elimination of the breakdown on the bottom window. However, a systematic optimization of the MTV acquisition frequency and the position of the laser Rayleigh range close to the bottom wall can further mitigate the noise and improve image quality to acquire state-of-the-art quality data. For instance, reducing the FS beam frequency can further apart the adjacent exposures such that the minor tracerlines would wash away and diffuse outside the laser field domain before they have much chance to be cascaded or imaged. We have performed testing visualization experiments in He II at 1.9 K with an optimized FS beam frequency of 500 Hz to eliminate the molecular deposition near the bottom wall. A representative image is shown in Fig. 7.6. Such image quality can be analyzed easier with a reduced uncertainty.

There is a meaningful difference between the constants in classical fluids and He II. The magnitude of this difference is much greater than the overall 95% confidence error. This difference suggests that the interaction between the normal fluid and the entanglement of the quantized vortices near the wall can significantly affect the flow and cause the mean velocity profile to adjust accordingly. Therefore, our results suggest that the quasi-classical turbulent does not hold in high Re flows near the solid boundary where the velocity gradient is extremely high and the mutual friction can no longer couple the fluids.

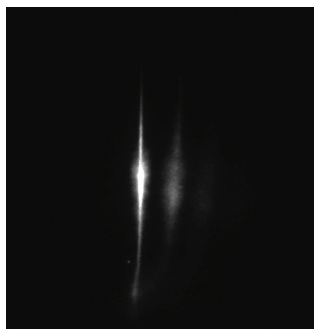


Fig. 7.6: Elimination of the molecular deposition near the bottom wall using 500 Hz FS laser in a driftline image obtained with the superimposition of 500 snapshots in a test He II flow.

CHAPTER 8

SUMMARY AND FUTURE WORK

Wall-bounded turbulent flows usually exhibit very different velocity scalings in an inner region near the solid boundary in comparison to an outer region far from the wall. In classical turbulent pipe flow, the velocity profile very close to the wall scales linearly whereas close to the centerline, the velocity approaches a uniform profile. Between the inner and outer layer, it is accepted that there exists an overlap region where a logarithmic mean velocity profile exists. When the velocity profile is nondimensionalized using appropriate wall parameters, a universal velocity profile is resulted which has been subject to intense research. Such knowledge in non-classical He II turbulent pipe flow does not exist. We designed and conducted a pioneering experiment to visualize and study the NVP in He II. This resulted in exploring the possible existence and properties of a log law velocity profile in He II turbulent pipe flow.

In our experiments, high Re_D He II flows exceeding a million were generated using a flow facility called Liquid Helium Flow Visualization Facility. We utilize a bellows pump system to push He II into a square $2 \times 2 \text{ cm}^2$ pipe which can be optically accessed. A powerful visualization technique in He II called the molecular tagging velocimetry was used which uses metastable helium molecules He_2^* as tracers. We developed a robust image processing algorithm to analyze the acquired images and extract the mean velocity profile. By analyzing and nondimensionalizing this velocity profile, we indeed observed a law of the wall in He II turbulent pipe flows for the first time. The non-classical law of the wall shows a noticeable deviation from the classical form. In particular, the von Kármán coefficient in He II was determined in the range 0.154 to 0.160 versus the classical value, 0.37-0.42. The additive constant is also determined in the range of -23.2 to -24 in comparison to the classical range of 4 to 6. The origin of the difference from the classical form was recognized and explained to be due to the non-classical force of mutual friction which exerts on the normal fluid in the highly gradient region near the wall and changes the velocity profile.

To analyze the error in the measurements, we developed a comprehensive computational uncertainty analysis. As the final conclusion of our experiments, we report $\kappa_s = 0.160 \pm 0.015$ and $B_s = -23.2 \pm 0.4$ for $Re_D = 1.01 \times 10^6$ and $\kappa_s = 0.154 \pm 0.010$ and $B_s = -24.0 \pm 0.4$ for $Re_D = 1.21 \times 10^6$.

There are interesting experimental studies that can follow what the recent work has started.

1. Law of the Wall in Classical He I or close to lambda point

We hypothesize that the difference between the classical law of the wall and the one in He II arises due to the effects of the mutual friction. Therefore, recovering the classical law of the wall using He I flows in our flow pipe can serve as a strong validation of our measurement technique. Such measurements can also help addressing the discrepancies in the classical law of the wall research field concerning the universality of it.

2. Double-line Molecular Tagging Velocimetry

By tracking a single tracerline in the flow pipe, one can only correlate the streamwise velocities along the tracerline and obtain the streamwise velocity structure function S_n^\perp . However, no information about the longitudinal velocity structure function S_n^\parallel can be obtained. We have previously shown [1] the design of a novel optical system called the “Double-line Molecular Tagging Velocimetry (DL-MTV)”. Our DL-MTV design is capable of producing both structure functions in He II. The preliminary measurements with the DL-MTV design are shown in Fig. 8.1. These structure function are defined as (refer to Fig. 5.4):

$$S_n^\perp(\Delta y) = \overline{|u_x(x, y + \Delta y) - u_x(x, y)|^n}, \quad (8.1)$$

$$S_n^\parallel(\Delta x) = \overline{|u_x(x + \Delta x, y) - u_x(x, y)|^n}. \quad (8.2)$$

In the case that the flows to be examined are boundary flows (anisotropic turbulent flows), the scalings of these structure functions can be very different in the near-wall region. Thus measuring both structure functions can be very valuable [99, 100]. Such measurements in classical ultra-high Re pipe flow are rare and do not exist in the case of non-classical fluids [99, 100].

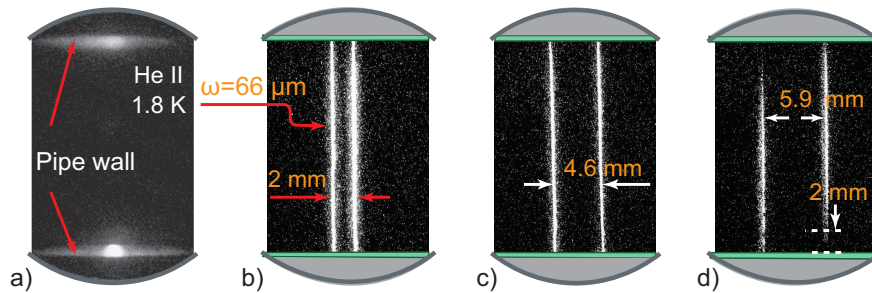


Fig. 8.1: (a) Background Image at 1.8 K (b,c) Images showing two tracerlines created at different streamwise separation distances (d) Tunability of the vertical positions of the two tracerlines

Part II

Design Work: A magnetic levitation based low-gravity simulator

CHAPTER 1

INTRODUCTION

Reduced gravity is known to have profound effects on various biological and physical systems. For instance, a weightless environment may prohibit cell culture growth [101] and may cause cellular stressor and bone loss that can negatively impact astronauts' health [102–104], but it can be advantageous for growing tissues [105]. In fluid systems, reduced gravity can significantly affect the surface oscillation of liquid drops [106], the sloshing dynamics of cryogenic propellants in spacecrafts [107], boiling heat transfer [108, 109], and bubble cavitation [110]. In biological and material science, the potential of reduced gravity for materials processing [111], growing crystals [112] and growing tissues [105] has been recognized. Conducting systematic research to understand the effects of gravity on these diverse systems will undoubtedly advance our knowledge. Furthermore, various programs initiated recently by public space agencies and private organizations [113–115] aiming at long-term human habitation of the Moon and Mars have further raised the needs of experimental research in low-gravity environment (LGE).

The best low-gravity condition can be achieved in spaceflight experiments conducted during space-shuttle missions [116] and at space stations [117]. However, these experiments are extremely cost-intensive and limited by the small payload size [118]. The fact that the astronauts have to conduct the experiments instead of the trained scientists also put constraints on the design of the experiments. As a consequence, researchers have devoted great efforts in developing ground-based low-gravity simulators. A major group of these simulators use free fall to achieve near-zero gravity, including parabolic aircraft [119, 120], drop towers [121, 122], sounding rockets [123], and suborbital rocketry [124]. Despite their usefulness, a known limitation of these facilities is the relatively short low-gravity duration (i.e., from several seconds to a few minutes [125]), which makes them unsuitable for wide range of experiments [126] that require a long duration data acquisition. In biological and medical research, rotational facilities such as clinostat machines [127, 128], rotating wall vessels [129], and random positioning machines [130] are also adopted to achieve a small time-averaged gravity vector [131, 132]. Although these simulators are convenient, they do not produce a genuine low-gravity environment and can generate unwanted centrifugal forces and circulating flows in the samples [131–133].

On the other hand, magnetic field gradient based levitation of various diamagnetic materials has been demonstrated [134–136]. Even living organisms have been successfully levitated [137–141], and there is no evidence of any cumulative harmful effects due to the field exposure [140–142]. Compared to other low-gravity simulator systems, a magnetic levitation based simulator offers unique advantages, including low cost, easy accessibility, adjustable gravity, and practically unlimited operation time [137, 138, 143]. However, a known issue with MLSs is their highly non-uniform force field around the levitation point. If we define a 0.01- g functional volume $V_{0.01g}$ where the net force results in an acceleration less than 1% of the Earth’s gravity g , $V_{0.01g}$ is typically less than a few microlitres (μL) for conventional solenoid MLSs. Although diamagnetic samples with sizes larger than $V_{0.01g}$ can be levitated, a stress field caused by the residue force inside the samples can compromise the measurement results. Despite some limited efforts in designing MLSs for improved functional volumes [144–146], a major progress is still lacking. Furthermore, the high energy consumption rate of conventional resistive solenoid MLSs is also concerning. For instance, 4 MW electric power is required to levitate a frog using a resistive solenoid MLS [137].

In this part, we report an innovative MLS design which consists of a gradient-field Maxwell coil placed in the bore of a superconducting (SC) magnet. By optimizing the SC magnet’s field strength and the current in the Maxwell coil, we show that an unprecedented $V_{0.01g}$ of over 4,000 μL can be achieved in a compact coil of 8 cm in diameter. This optimum $V_{0.01g}$ increases with the size and the field strength of the MLS. We then discuss how such a MLS can be made using existing high- T_c superconducting materials so that long-time operation with minimal energy consumption can be achieved. To further demonstrate the usefulness of this MLS, we also consider reducing its current and the field strength to emulate the gravity on Mars ($g_M = 0.38g$). It turns out that a functional volume over 20,000 μL can be produced, in which the gravity only varies within a few percent of g_M . Our design concept may break new ground for exciting applications of MLSs in future low-gravity research. The recent advancements may open new horizons for the future of low-gravity research. The contents of Part II are peer reviewed and published in “npj Microgravity” [147].

CHAPTER 2

FUNDAMENTALS OF MAGNETIC FIELD CALCULATIONS

In this chapter, we introduce the expressions that we use to calculate magnetic field, potential energy field, force field, and all the quantities needed in our later analysis.

2.1 Magnetic Field Calculation

The magnetic field $\mathbf{B}(\mathbf{r})$ generated at \mathbf{r} by a single current loop in three-dimensional space (3D) is given by the Biot-Savart law [148]:

$$\mathbf{B}(\mathbf{r}) = \frac{\mu_0 I}{4\pi} \oint \frac{d\mathbf{l} \times (\mathbf{r} - \mathbf{l})}{|\mathbf{r}|^3}, \quad (2.1)$$

where $d\mathbf{l}$ is the an infinitesimal length vector (elementary vector) along the current loop. A key component in our design is a gradient Maxwell coil. The geometry of this coil is given in Fig. 2.1 (a). It consists of two identical coaxial loops with a diameter D of 8 cm when the loops are vertically separated by a distance of $L = \sqrt{3}D/2$. The current in the top loop is clockwise (viewed from the top) while the current in the bottom loop is counterclockwise. It was first demonstrated by

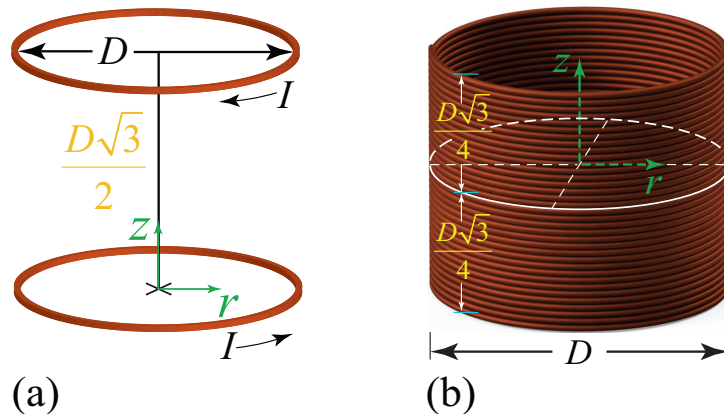


Fig. 2.1: (a) Schematic and dimensions of a gradient-field Maxwell coil with a diameter $D = 8$ cm. The origin of the coordinate system is at the center of the bottom Maxwell loop. (b) Schematic and dimensions of a solenoid magnet with a diameter of $D = 8$ cm and a height of $\sqrt{3}D/2$. The center of the solenoid is the coordinate system origin.

Maxwell that such a coil configuration could produce a highly uniform field gradient in the region between the two loops [149].

For our gradient Maxwell coil, we can make a use of Eq. 2.1 to calculate its magnetic field $\mathbf{B}_1(\mathbf{r})$ in 3D. $\mathbf{B}_1(\mathbf{r})$ can be decomposed into an axial component along z and a radial component along r due to the axial symmetry. If the coordinate origin is placed at the center of the lower loop, these two components are derived as:

$$\begin{aligned} B_1^{(r)}(r, z) &= \frac{\mu_0 I}{4\pi} \int_0^{2\pi} \left[\frac{Rz \cos(\phi)}{D_1^3} + \frac{R(L-z) \cos(\phi)}{D_2^3} \right] d\phi, \\ B_1^{(z)}(r, z) &= \frac{\mu_0 I}{4\pi} \int_0^{2\pi} \left[\frac{R^2 - Rr \cos(\phi)}{D_1^3} + \frac{Rr \cos(\phi) - R^2}{D_2^3} \right] d\phi, \end{aligned} \quad (2.2)$$

where spacial coefficients D_1 and D_2 are given by:

$$\begin{aligned} D_1 &= \sqrt{[r - R \cos(\phi)]^2 + [R \sin(\phi)]^2 + z^2}, \\ D_2 &= \sqrt{[r - R \cos(\phi)]^2 + [R \sin(\phi)]^2 + (z - L)^2}. \end{aligned} \quad (2.3)$$

where $R = D/2$.

Another conventional magnet configuration is a solenoid. We assume a solenoid in our later analysis which its geometry is shown in Fig. 2.1 (b). Our solenoid has a diameter D of 8 cm and a length of $L = \sqrt{3}D/2$ to match the gradient Maxwell coil dimensions. If we assume the coordinate system is at the center of the solenoid and the wire used to fabricate the solenoid is thin such that the solenoid turn number N is large but the total turn-current NI remains finite, an exact expression for the generated magnetic field can be derived based on Eq. 2.1 [150, 151]:

$$\begin{aligned} B^{(r)}(r, z) &= \frac{\mu_0 NI}{4\pi} \frac{2}{L} \sqrt{\frac{R}{r}} \left[\frac{k^2 - 2}{k} K(k^2) + \frac{2}{k} E(k^2) \right]_{\zeta_-}^{\zeta_+}, \\ B^{(z)}(r, z) &= \frac{\mu_0 NI}{4\pi} \frac{1}{L\sqrt{Rr}} \left[\zeta k \left(K(k^2) + \frac{R-r}{R+r} \Pi(h^2, k^2) \right) \right]_{\zeta_-}^{\zeta_+}, \end{aligned} \quad (2.4)$$

where where $R = D/2$ and spacial coefficients k^2 , h^2 and ζ_{\pm} are given by:

$$\begin{aligned} k^2 &= \frac{4Rr}{(R+r)^2 + \zeta^2}, \\ h^2 &= \frac{4Rr}{(R+r)^2}, \\ \zeta_{\pm} &= z \pm L/2, \end{aligned} \quad (2.5)$$

and functions $K(k^2)$, $E(k^2)$, and $\Pi(h^2, k^2)$ are calculated by:

$$\begin{aligned} K(k^2) &= \int_0^{\pi/2} \frac{d\theta}{\sqrt{1 - k^2 \sin^2 \theta}}, \\ E(k^2) &= \int_0^{\pi/2} d\theta \sqrt{1 - k^2 \sin^2 \theta}, \\ \Pi(h^2, k^2) &= \int_0^{\pi/2} \frac{d\theta}{(1 - h^2 \sin^2 \theta) \sqrt{1 - k^2 \sin^2 \theta}} \end{aligned} \quad (2.6)$$

2.2 Potential Energy and Gradient Force Calculation

If a small sample with a volume of ΔV is inserted in a static magnetic field $\mathbf{B}(\mathbf{r})$, the energy of the magnetic field increases due to the magnetization of the sample material which is given by [148]:

$$\Delta E_B = \frac{-\chi B^2(\mathbf{r})}{2\mu_0(1 + \chi)} \Delta V, \quad (2.7)$$

where χ is the magnetic susceptibility of the sample material and μ_0 is the vacuum permeability. For diamagnetic materials with negative χ , ΔE_B is positive and therefore it requires energy to insert a diamagnetic sample into the $\mathbf{B}(\mathbf{r})$ field. Counting in the gravity effect, the total potential energy $E(\mathbf{r})$ associated with the sample per unit volume (specific energy) can be written as:

$$E(\mathbf{r}) = \frac{-\chi B^2(\mathbf{r})}{2\mu_0(1 + \chi)} + \rho g z, \quad (2.8)$$

where ρ is the material density. This energy leads to a force per unit volume \mathbf{F} acting on the sample as:

$$\mathbf{F} = -\nabla E(\mathbf{r}) = \frac{\chi}{\mu_0(1 + \chi)} \mathbf{B} \cdot \nabla \mathbf{B} - \rho g \hat{e}_z. \quad (2.9)$$

For an appropriate non-uniform magnetic field, the vertical component of the field-gradient force (i.e., the first term on the right side in Eq. (2.9)) may balance the gravitational force at a particular location, i.e., the levitation point. Sample suspension can therefore be achieved at this point.

We have developed a computer code to calculate these physical quantities based on the above expressions. We only calculate the quantities in the r - z plane due to the axial symmetry. Typically we use a uniform square grid with spatial resolutions of $\Delta r = 10 \mu\text{m}$ and $\Delta z = 10 \mu\text{m}$ to discretize the computational domain. Convergence analysis is performed to assure such spatial resolution yields reliable convergence of the numerical results.

CHAPTER 3

MAGNETIC LEVITATION-BASED LOW-GRAVITY SIMULATORS

In this chapter, we first discuss the concept of the magnetic levitation using a solenoid magnet as an example. After that, we present our innovative MLS design concept.

3.1 Levitation by a solenoid magnet

It can be mathematically shown [137] that in order to attain a stable levitation, the specific potential energy E must have a local minimum at the levitation point so the sample cannot stray away. Since $E(\mathbf{r})$ depends on the material properties besides the $\mathbf{B}(\mathbf{r})$ field, we need to specify the sample material. Considering the fact that water has been utilized in a wide range of low-gravity researches [152–154] and is also the main constituent of living cells and organisms [155], we adopt the water properties at ambient temperature [156] (i.e., $\chi = -9.1 \times 10^{-6}$ and $\rho = 10^3 \text{ kg/m}^3$) in all subsequent analyses.

The magnetic field calculations of the solenoid shown in Fig. 2.1 (b) including the specific potential energy and the gradient force can be done using Eq. 2.8 and Eq. 2.9, respectively. In Fig. 3.1 (a), we show the calculated $E(\mathbf{r})$ near the top section of the solenoid when a turn-current of $NI = 607.5 \text{ kA}$ is applied. As it can be seen, E is higher near the solenoid wall due to the strong \mathbf{B} field. Slightly above the solenoid geometry, there is a trapping region where $E(r)$ depicts a local minimum enclosed by the dashed contour. Such a local minimum results in an inward force field towards the region center. When a water sample is placed in this region, it moves towards the center of the region where the net force is zero, . In other word, the samples settles where the net force is zero, i.e., the levitation point. Based on the energy field, the specific gradient force can be calculated. The solid black line contour in Fig. 3.1 (a) depicts a low-force region in which the net force exerting on the sample causes an acceleration less than $0.01g$. The overlapping volume of $0.01g$ force region and the trapping region is defined as the functional volume $V_{0.01g}$ where the sample not only experiences a weak residue force but also remains trapped. In Fig. 3.1 (b), the calculated $V_{0.01g}$ as a function of NI is shown for the solenoid. Since the magnetic force is directly

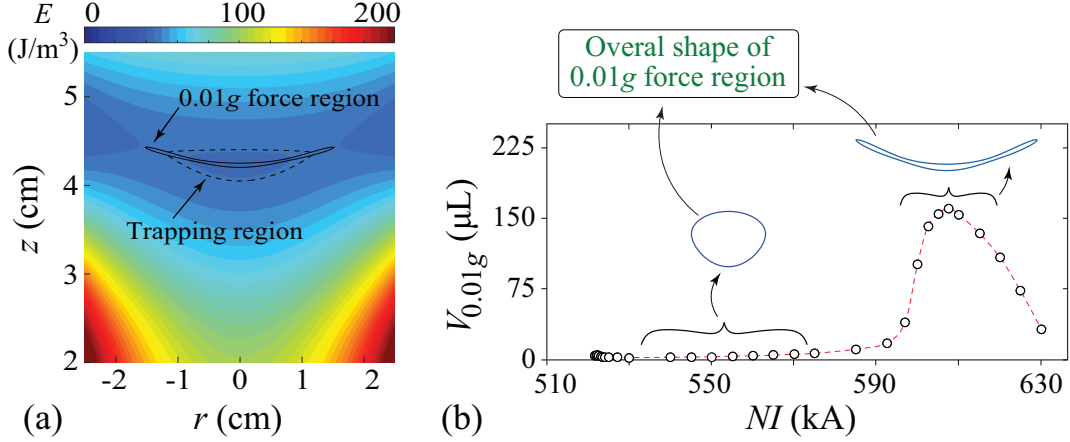


Fig. 3.1: (a) Calculated specific potential energy $E(\mathbf{r})$ of a small water sample placed in the magnetic field. The turn-current NI of the solenoid is 607.5 kA. The origin of the coordinates is at the center of the solenoid. The dashed contour denotes the boundary of the trapping region, and the solid contour shows the low-force region. (b) The functional volume $V_{0.01g}$ (i.e., overlapping volume of the two contours) versus the turn-current NI . Representative shapes of the low-force region are shown.

proportional to the magnetic field strength, the trapping region emerges only above a threshold total turn-current of about $NI = 520$ kA. As NI increases, $V_{0.01g}$ first remains very small (i.e., a few μL) and has a shape like a inverted raindrop. When NI is above about 600 kA, $V_{0.01g}$ grows rapidly and peaks at $NI = 607.5$ kA before it drops with further increasing NI . In the peak regime, $V_{0.01g}$ has a highly anisotropic shape of a bowl, due to the highly non-uniform force field. Even at its peak, the functional volume is still too small and anisotropic for most research applications. Moreover, the required total turn-current is extremely large and impractical.

3.2 Concept and Performance of our MLS

To increase $V_{0.01g}$, the key is to produce a more uniform field-gradient force to balance the gravitational force such that the net force remains low in a large volume. Base on Eq. (2.9), this can be achieved if we have a nearly uniform \mathbf{B} field and at the meanwhile the field gradient is almost constant in the same volume. These two seemingly irreconcilable conditions can be satisfied approximately. The idea is to combine a strong uniform field \mathbf{B}_0 and a weak field $\mathbf{B}_1(\mathbf{r})$ that has a fairly constant field gradient $\nabla\mathbf{B}_1$. In this way, the total field $\mathbf{B} = \mathbf{B}_0 + \mathbf{B}_1 \simeq \mathbf{B}_0$ is approximately uniform and its gradient $\nabla\mathbf{B} \simeq \nabla\mathbf{B}_1$ can also remain nearly constant.

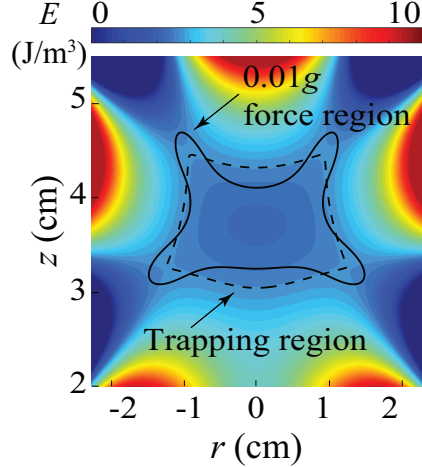


Fig. 3.2: Calculated specific potential energy $E(\mathbf{r})$ of a small water sample placed in the magnetic field for $I = 112.6$ kA and $B_0 = 24$ T. The origin of the coordinates is at the center of the bottom current loop. The black dashed contour denotes the boundary of the trapping region, and the black solid contour shows the low-force region (i.e., acceleration less than $0.01g$).

The uniform field \mathbf{B}_0 can be produced in the bore of a superconducting solenoid magnet. Indeed, for superconducting magnets used in magnetic resonance imaging applications, spatial homogeneity of the field better than a few parts per million (ppm) in a large space has become standard [157–159]. The recently built 32-T all-superconducting magnet at the National High Magnetic Field Laboratory (NHMFL) further proves the feasibility of producing strong uniform fields using cutting-edge superconducting technology [160]. As for the \mathbf{B}_1 field, we propose to produce it using the gradient Maxwell coil.

The results of the magnetic field calculations for the gradient Maxwell coil in the presence of a uniform field $B_0 = 24$ T are shown in Fig. 3.2 when a current of $I = 112.6$ kA is applied. Again, we use the dashed contour and the solid contour to show, respectively, the trapping region and the $0.01g$ low-force region. By evaluating the overlapping volume of the two regions, we obtain $V_{0.01g} = 4,004 \mu L$. More importantly, this functional volume is much more isotropic as compared to that in Fig. 3.1 (b), which makes it highly desirable in practical applications.

To optimize the coil current I and the base field B_0 , we have conducted further analyses. First, for a fixed B_0 , we vary the coil current I . Representative results at $B_0 = 24$ T are shown in Fig. 3.3 (a). It is clear that $V_{0.01g}$ peaks at about $I = 112.6$. We denote this peak value as V_{peak} . The decrease of $V_{0.01g}$ at large I is caused by the fact that the field \mathbf{B}_1 generated by the coil is no longer much smaller than the base field \mathbf{B}_0 , which impairs the uniformity of the field-gradient force. Next, we

vary the base field strength B_0 and determine the corresponding V_{peak} at each B_0 . The result is shown in Fig. 3.3 (b). It turns out that there exists an optimum base field strength of about 24.7 T (denoted as $B_{0,\text{max}}$), where an overall maximum functional volume (denoted as V_{max}) of about 4,050 μL can be achieved. This volume is comparable to those of the largest water drops adopted in the past spaceflight experiments [154, 161]. The above analyses assumed a fixed coil diameter

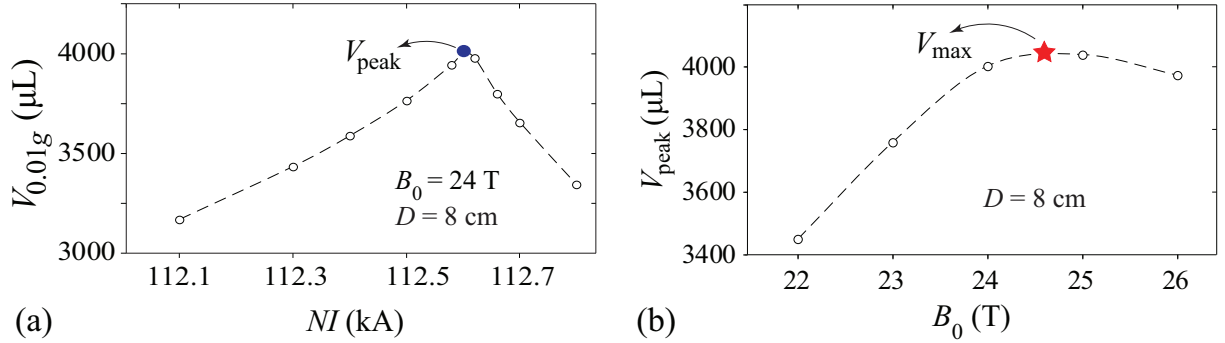


Fig. 3.3: (a) Calculated $V_{0.01g}$ as a function of the coil current I for the Maxwell coil shown in Fig. 2.1(a) with $B_0 = 24 \text{ T}$. The largest $V_{0.01g}$ is denoted as V_{peak} . (b) The optimal V_{peak} versus B_0 is shown. The absolute maximum of V_{peak} is shown as V_{max} .

$D = 8 \text{ cm}$. When D varies, the maximum functional volume V_{max} and the corresponding MLS parameters (i.e., I_{max} and $B_{0,\text{max}}$) should also change. To examine the coil size effect, we have repeated the aforementioned analyses with a number of coil diameters. The results are collected in Fig. ???. As D increases from 6 cm to 14 cm, the maximum functional volume V_{max} increases from

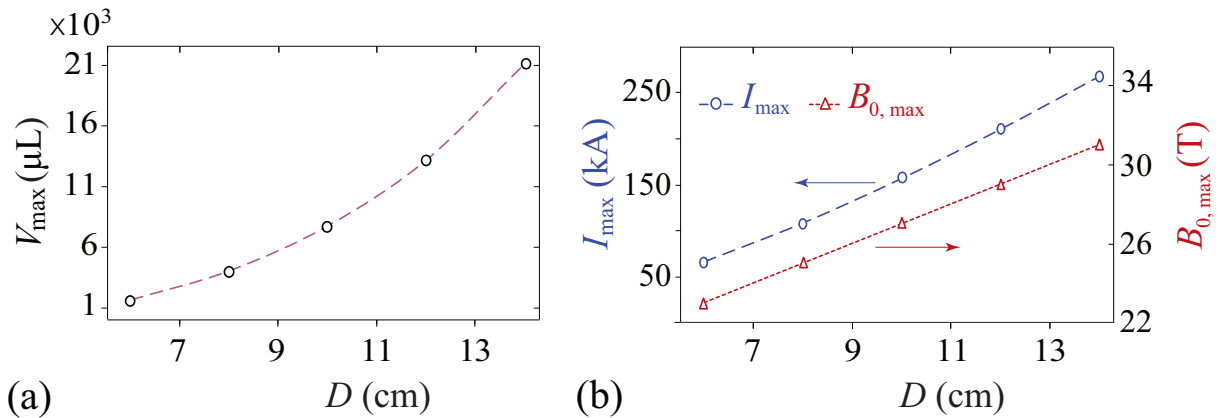


Fig. 3.4: (a) Maximum functional volume V_{max} for the Maxwell coil as a function of diameters D . (b) The optimal I_{max} and $B_{0,\text{max}}$ in order to acquire the maximum volume are shown as a function of the coil diameter D .

about $1,500 \mu\text{L}$ to over $21,000 \mu\text{L}$, i.e., over 14 times. At the meanwhile, the required coil current I_{max} and the base field strength $B_{0,max}$ increase almost linearly with D by factors of about 4 and 1.3, respectively. This analysis suggests that it is advantageous to have a larger coil provided that the desired I_{max} and $B_{0,max}$ can be achieved.

3.3 A Practical Design for our MLS

The MLS concept that we presented requires an applied current of the order 10^2 kA in both loops of the gradient-field Maxwell coil. A natural question is whether this is practical. One may consider to make the loop using a thin copper wire with 10^3 turns so that a current of the order 10^2 A in the wire is sufficient. However, simple estimation reveals that the Joule heating in the resistive wire can become so large such that the wire could melt. To solve this issue, we propose to fabricate the Maxwell coil using REBCO (i.e., rare-earth barium copper oxide) superconducting tapes similar

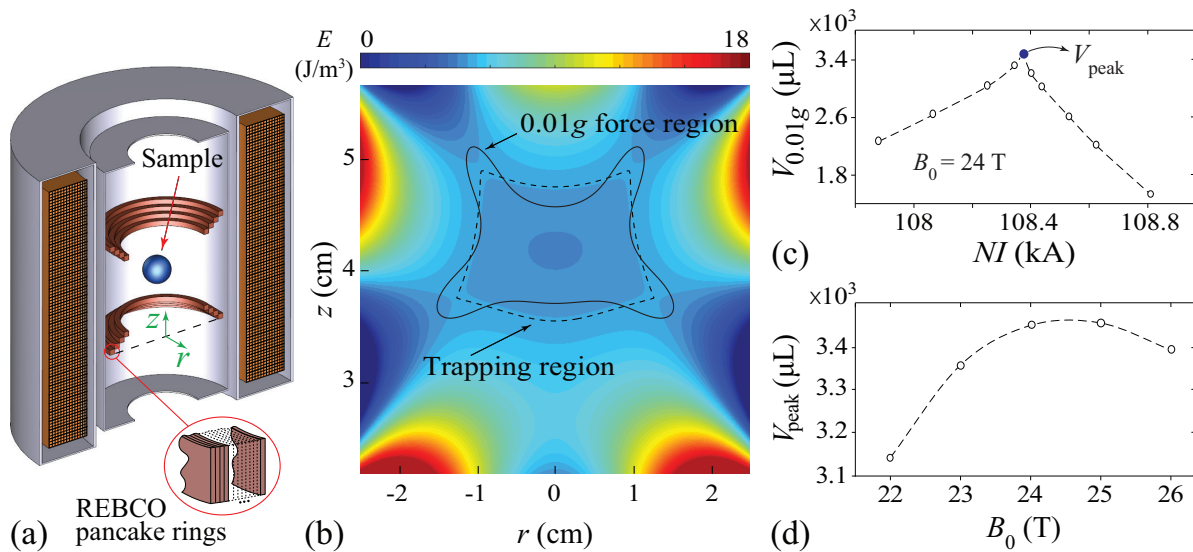


Fig. 3.5: (a) Schematic of the practical MLS configuration composed of a 24-T outer superconducting magnet and four sets of inner gradient-field Maxwell coils. Coils are made of REBCO pancake rings. The bore of the superconducting magnet is 12 cm and the average diameter of the pancake rings is 8 cm, same as the ideal design. The origin of the coordinate system is at the center of the lowest pancake ring. (b) Computed contour map of the specific potential energy $E(\mathbf{r})$ for a small water sample inserted slightly above the center of the practical MLS while a total current-turn of $NI = 108.37$ kA is applied. The dashed contour depicts the magnetic trap whereas the solid contour shows the $0.01g$ force region. (c) Computed $V_{0.01g}$ as a function of the total current-turn, NI , at $B_0 = 24$ T. The maximum $V_{0.01g}$ is denoted as V_{peak} . (d) Peak functional volume, V_{peak} , is computed versus B_0 . The maximum V_{peak} is again achieved at $B_0=24$ T.

to those used in the work by Hahn *et al.* [162]. A schematic of the proposed MLS setup is shown in Fig. 3.5 (a). A 24-T superconducting magnet with a bore diameter of 120 mm (existing at the NHMFL [163, 164]) is assumed for producing the \mathbf{B}_0 field. Four sets of gradient-field Maxwell coils made of REBCO pancake rings are placed in the bore of the superconducting magnet. Each pancake ring is made of 94 turns of the REBCO tape (width: 4 mm; thickness: 0.043 mm) so its cross section is nearly a square (i.e., 4 mm by 4 mm). The pancake rings are arranged along the diagonal lines of a standard gradient Maxwell coil and the averaged diameter of the pancake rings is about 8 cm. This coil configuration is found to produce a \mathbf{B}_1 field with minimal deviations from that of an ideal gradient Maxwell coil. While the superconducting magnet at the NHMFL is cooled by immersion in a liquid helium bath, the compact REBCO coils could be cooled conveniently by a 4-K pulse-tube cryocooler inside a shielded vacuum housing. A room-temperature center bore with a diameter as large as 6 cm can be used for sample loading and optical access. When a current of about 290 A is applied in the REBCO tapes, a total turn-current $NI = 4 \times 94 \times 290 \text{ A} \simeq 109 \text{ kA}$ can be achieved. Note that the quenching critical current of the REBCO tape can reach 700 A even under an external magnetic field of 30 T [165]. Therefore, operating our REBCO coils with a tape current of 290 A should be safe and reliable.

To prove the performance of our practical MLS design, we have repeated the previously presented optimization analyses. A representative plot of the specific potential energy $E(\mathbf{r})$ at a total turn-current $NI = 108.37 \text{ kA}$ and $B_0 = 24 \text{ T}$ is shown in Fig. 3.5 (b). The overall shapes of the trapping region and the low-force region are nearly identical to those of the ideal gradient Maxwell coil. The dependence of $V_{0.01g}$ on the turn-current NI at $B_0 = 24 \text{ T}$ is shown in Fig. 3.5 (c). A peak functional volume V_{peak} about $3,450 \mu\text{L}$ is achieved. In Fig. 3.5 (d), the peak volume V_{peak} obtained at various base field strength B_0 is shown. Again, the trend is similar to that in Fig. 3.3. Therefore, despite the change in the coil geometry as compared to the ideal gradient-field Maxwell coil, the performance of our practical design does not exhibit any significant degradation.

3.3.1 Emulating Reduced Gravity in Extraterrestrial Environment

Beside levitating samples for near-zero gravity research, our MLS can also be tuned to partially cancel the Earth's gravity so that ground-based emulation of reduced gravities in extraterrestrial environment (such as on the Moon or the Mars) can be achieved. To demonstrate this potential, we present further analyses of the practical MLS with lower applied currents for simulating the Martian gravity $g_M = 0.38g$ [143]. In Fig. 3.6 (a), we show contour plots of the specific potential

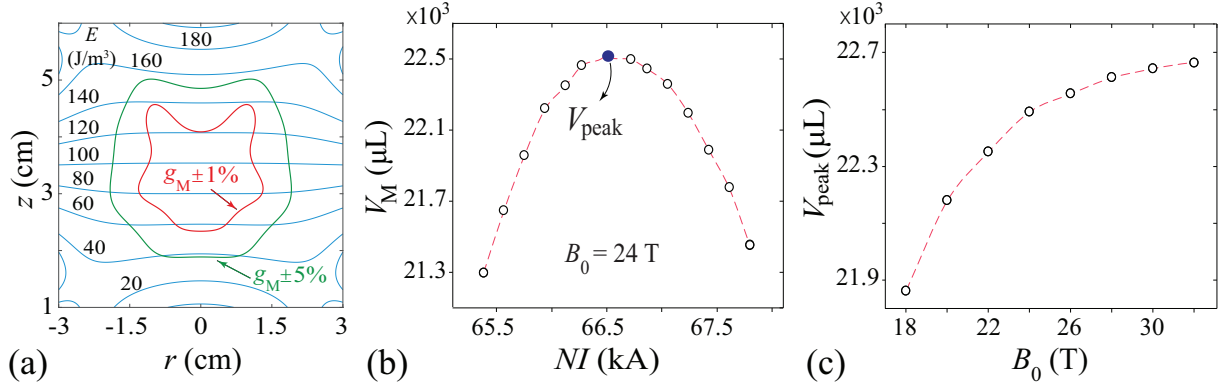


Fig. 3.6: (a) Contour plot of calculated specific potential energy $E(\mathbf{r})$ of a water sample inserted in the practical MLS at $NI = 66.55$ kA and $B_0 = 24$ T. The black solid contours depicts functional volumes at 1% and 5% g_M , respectively. (b) The functional volume V_M in which the gravity varies within 5% of g_M as a function of the total current-turn NI . The optimal value is denoted as V_{peak} (c) The peak functional volume V_{peak} as a function of the base magnetic field B_0 .

energy $E(\mathbf{r})$ for water samples in the practical MLS when a turn-current of $NI = 66.55$ kA is applied at $B_0 = 24$ T. It is clear that the energy contour lines (blue curves) are evenly spaced in the center region of the MLS, suggesting a fairly uniform and downward-pointing force in this region. We then calculate the magnitude of the force using Eq. 2.9. The two black contours in Fig. 3.6 (a) represent the boundaries of the regions in which the total force leads to an effective gravitational acceleration within 1% and 5% of g_M , respectively. If we define the volume of the contour in which the gravity varies within 5% of g_M as our functional volume V_M , its dependence on the turn-current at $B_0 = 24$ T is shown in Fig. 3.6 (b). This functional volume has a peak value V_{peak} of about $22.5 \times 10^3 \mu\text{L}$ at $NI = 66.55$ kA. This peak volume is so large such that even small animals or plants can be accommodated inside. We have also calculated the peak volume V_{peak} at different base field strength B_0 . As shown in Fig. 3.6 (c), initially the peak volume V_{peak} increases sharply with B_0 , and then it gradually saturates when B_0 is greater than about 24 T. Operating the MLS at higher B_0 gives marginal gain in the functional volume.

CHAPTER 4

SUMMARY AND FUTURE WORK

The discussions provided in Part II clearly demonstrated the potential of magnetic levitation, in particular our practical MLS design in LGE research and science. The provided analyses show the operational enhancements of our design in comparison with conventional solenoid MLS systems. An unprecedentedly large and isotropic functional volume, approximately three orders of magnitude larger than that of most previous efforts (i.e. $4000 \mu L$) can be achieved using this novel configuration. In near future and with anticipated advancements in magnet technology, functional volumes as large as $25000 \mu L$ can be obtained using the proposed practical design. This configuration is designed flexibly such that the simulation of extraterrestrial gravity e.g. on planet Mars can be achieved by simply adjusting the current. The implementation of the superconducting magnets in our design ensures a stable operation of this MLS with a minimal energy consumption rate. This rises an opportunity for a low running cost prospective low-gravity research and technology. These advancements might also stimulate more enthusiasm towards other physics and areas of fluid dynamics that can be studied using magnetic levitation.

There is an interesting design work that can continue what our work has started. One can finalize the design and manufacture the practical MLS at the NHMFL in order to validate the concept and performance, and eventually conduct real low-gravity experiment using water drops or small living organisms and biological specimens. Such project is not only a great interdisciplinary combination of fundamental physics, engineering, biology and design, but also can truly demonstrate the superiority of the our MLS concept to previous low-gravity simulation methods.

Part III

Computational work: Transient Heat Transfer and Boiling in Superfluid Helium

CHAPTER 1

INTRODUCTION

He II has been widely utilized as a coolant in various scientific and engineering applications due to its superior heat transfer capability. An important parameter required in the design of many He II based cooling systems is the peak heat flux q^* , which refers to the threshold heat flux above which boiling spontaneously occurs in He II. Past experimental and numerical studies showed that q^* increases when the heating time t_h is reduced, which leads to an intuitive expectation that very high q^* may be achievable at sufficiently small t_h . Knowledge on how q^* actually behaves at small t_h is important for applications such as laser ablation in He II. Here we present a numerical study on the evolution of the thermodynamic state of the He II in front of a planar heater by solving the He II two-fluid equations of motion. For an applied heat flux, we determine the heating time beyond which the He II near the heater transits to the vapor phase. As such, a curve correlating q^* and t_h can be obtained, which nicely reproduces some relevant experimental data. Surprisingly, we find that there exists a critical peak heat flux q_c^* , above which boiling occurs nearly instantaneously regardless of t_h . We reveal that the boiling in this regime is essentially cavitation caused by the combined effects of the first-sound and the second-sound waves in He II. Based on this physical picture, an analytical model for q_c^* is developed, which reproduces the simulated q_c^* values at various He II bath temperatures and hydrostatic head pressures. This work represents a major progress in our understanding of transient heat transfer in He II. The contents of Part III have been peer reviewed and published in “Physical Review B” [166].

CHAPTER 2

FUNDAMENTALS OF TRANSIENT HEAT TRANSFER IN HE II

He II exhibit several non-classical thermo-mechanical properties due to its unique two-fluid system [167]. For instance, there exists an ultra-efficient heat transfer mode in He II so-called thermal counterflow. The effective thermal conductivity in this mode exceeds that of pure metals [53]. In He II in the presence of a heat flux q , the normal fluid carries the heat away from the heater with a fluid velocity that is governed by $v_n=q/\rho sT$ where ρ is He II total density, s is specific entropy, and T is temperature. Due to the conservation of mass, the superfluid moves in the opposite direction towards the heater. This phenomena is schematically shown in Fig. 2.1. It is straightforward to derive the superfluid velocity as $v_s=-v_n\rho_n/\rho_s$ where ρ_n and ρ_s are the normal and superfluid component density, respectively. Thermal counterflow is also always associated with the generation of mutual friction that fundamentally impacts the fluid dynamics and heat transfer processes in He II [168–174]. Another unique property of He II is the existence of two sound modes. One is the classical pressure-density sound waves, known as the first sound within which the two fluids experience co-flow. The other mode is a non-classical temperature-entropy wave, known as the sec-

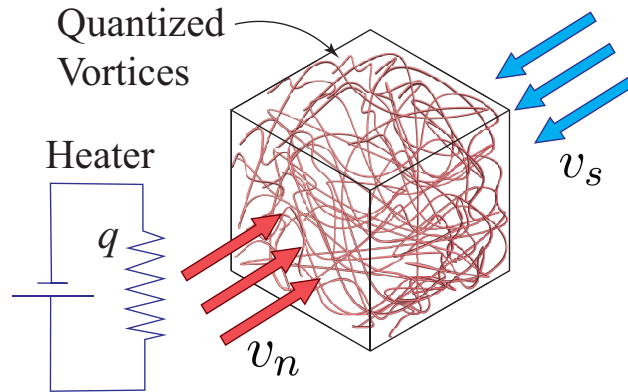


Fig. 2.1: In He II in the presence of a heat flux q , the normal fluid carries the heat away from the heat source with a velocity v_n whereas the superfluid moves in the opposite direction towards the heat source with a velocity v_s to satisfy the conservation of mass.

ond sound within which the two components travel in opposite directions, for instance, in thermal counterflow.

Due to this extraordinary heat transfer mode, He II has been widely used in thermal engineering applications such as cooling superconducting magnets, particle accelerator cavities and colliders [53]. Due to the rapid nature of heat deposition and dissipation, such systems always involve transient heat transfer in He II. Transient heat transfer in He II is a complex process largely due to the emergence of several sub-processes including the thermal counterflow, propagation of second-sound waves, nucleation of quantized vortices, and the interplay of them. Naturally, the simplicity yet usefulness of investigating transient heat transfer in He II in a one-dimensional (1D) geometry, i.e., a planar heater in a uniform channel, has attracted numerous experimental and numerical studies. Early studies suggested that applying heat flux generates a second sound pulse that propagates in He II and a counterflow establishes within the pulse. Later, some studies reported a strong deviation between the theoretical calculations [175] for the second sound velocity as a function of heat flux and the experimental results [176]. Further examinations [177–181] revealed that if the relative velocity of the two fluids exceeds a small critical value, this can lead to complex dynamics of vortex lines, the so-called entanglement of quantized vortices. In this case, the interaction between the thermal excitations and the entanglement can attenuate of second-sound pulse which results in conversion of the energy carried by the pulse to the internal energy of He II.

The second sound attenuation can have further consequences. Gradually, a heated region in front of the heating source can form that is usually called the thermal layer. When the heat flux is relatively high, the chaotically-growing entanglement eventually suppress the second sound pulse to a limiting profile [182] such that the thermal energy is largely deposited in the thermal layer. As a result, eventually a temperature spike near the heater can occur which can be much larger than the second-sound amplitude [177, 178]. The examination of the thermodynamic state curve of He II in the presence of transient heat transfer in He II [183] shows that if the heat flux is sufficiently large, i.e., above a peak heat flux q^* , the temperature spike can reach the saturation temperature after a certain amount of time. This phenomena can be assumed as the creation of two-phase fluid or simply boiling in He II. This physical picture suggests a relationship between the peak heat flux and the time that takes until boiling occurs in He II, i.e, the onset time of boiling t_h .

There have been numerous experimental and numerical studies examining the dependence between time and heat flux in He II, i.e., the q^* - t_h relationship [184–190]. A power-law dependence $q^* \propto t_h^{-n}$ of q^* on the heating time t_h was reported in literature, where the power index n varies in

the range of 0.25 to 0.5 depending on the magnitude of the applied heat flux and other experimental conditions such as the He II bath temperature T_b and the hydrostatic head pressure $P_h = \rho g H$ (where H is the He II depth and g is the gravitational acceleration) [184, 185, 187, 189, 190]. These results may give an intuitive expectation that very high q^* may be achievable at sufficiently small t_h . However, knowledge on how q^* actually behaves in the high heat flux and short heating time regime is limited. Such knowledge could benefit various research fields such as nano-material fabrication via laser ablation in He II [191, 192]. Boiling in He II is a phenomena that can completely change the heat transfer mechanism and usually impact the system negatively [187], e.g., sudden cessation of the heat removal from superconducting surfaces. Therefore, systems involving high energy applications such as superconducting magnets can significantly benefit from this study.

CHAPTER 3

NUMERICAL METHODS

There has been a huge body of research to formalize the complex processes of fluid dynamics and heat transfer in He II, particularly as a mathematical model that incorporate the significant effects of quantized vortices [193, 194]. Here a standard fluid dynamics and heat transfer system of equations for the two-fluid model is used where mass, total momentum, superfluid momentum, and energy (written based on the entropy of the system) are conserved. Although the equations have similarities to classical Navier-Stokes equations in parts, this system of equation, developed for non-classical He II, can be written as:

$$\frac{\partial \rho}{\partial t} + \nabla \cdot (\rho \mathbf{v}) = 0, \quad (3.1)$$

$$\frac{\partial(\rho \mathbf{v})}{\partial t} + \nabla(\rho_s v_s^2 + \rho_n v_n^2) + \nabla P = 0, \quad (3.2)$$

$$\frac{\partial \mathbf{v}_s}{\partial t} + \mathbf{v}_s \cdot \nabla \mathbf{v}_s + \nabla \mu = \frac{\mathbf{F}_{ns}}{\rho_s}, \quad (3.3)$$

$$\frac{\partial(\rho s)}{\partial t} + \nabla \cdot (\rho s \mathbf{v}_n) = \frac{\mathbf{F}_{ns} \cdot \mathbf{v}_{ns}}{T}. \quad (3.4)$$

where the total momentum density is given by $\rho \mathbf{v} = \rho_s \mathbf{v}_s + \rho_n \mathbf{v}_n$ with subscripted s and n denoting the property of superfluid and normal fluid component, respectively, P is pressure, and T is temperature. The above system of equations consists of 4 fundamental equations and 5 unknowns, including \mathbf{v}_n , \mathbf{v}_s , P , T , \mathbf{F}_{ns} . Considering the large relative velocity (i.e., counterflow velocity) $v_{ns} = |\mathbf{v}_{ns}| = |\mathbf{v}_n - \mathbf{v}_s|$ of the two fluids at high heat fluxes, we also include the corrections to the thermodynamic properties of He II as proposed by Landau [167, 195]:

$$\mu(P, T, v_{ns}) = \mu^{(s)}(P, T) - \frac{1}{2} \frac{\rho_n}{\rho} v_{ns}^2, \quad (3.5)$$

$$s(P, T, v_{ns}) = s^{(s)}(P, T) + \frac{1}{2} v_{ns}^2 \partial(\rho_n/\rho)/\partial T, \quad (3.6)$$

$$\rho(P, T, v_{ns}) = \rho^{(s)}(P, T) + \frac{1}{2} \rho^2 v_{ns}^2 \partial(\rho_n/\rho)/\partial P. \quad (3.7)$$

where all the static properties (i.e., with superscribe $^{(s)}$) are extracted from the Hepak dynamic library [196]. Typically, the corrections amount to no more than a few percent of the property values in static He II. Gorter-Mellink mutual friction (per unit fluid volume) term \mathbf{F}_{ns} depends on

the relative velocity v_{ns} between the two fluid components and can be related to the vortex line density L which would be a new unknown. This relationship can be expressed as[197, 198]:

$$\mathbf{F}_{\mathbf{ns}} = \frac{\Gamma\rho_s\rho_n}{3\rho}LB_L\mathbf{v}_{\mathbf{ns}}, \quad (3.8)$$

where B_L is a known temperature-dependent coefficient[199]. Our system of equations can be finally solved by introducing a fifth equation that involves the vortex line density $L(\mathbf{r}, t)$. The spatial and temporal variations of L is given by Vinen's phenomenological equation as below:

$$\frac{\partial L}{\partial t} + \nabla \cdot (L\mathbf{v}_L) = \alpha_V|\mathbf{v}_{\mathbf{ns}}|L^{\frac{3}{2}} - \beta_V L^2 + \gamma_V|\mathbf{v}_{\mathbf{ns}}|^{\frac{5}{2}}. \quad (3.9)$$

where α_V , β_V , and γ_V are temperature-dependent Vinen's phenomenological coefficients [197]. Quantize vortices are not stationary in He II after nucleation, therefore, $\nabla \cdot (L\mathbf{v}_L)$ accounts for the drifting of the vortices [200, 201]. The vortex mean velocity \mathbf{v}_L is assumed to be the local superfluid velocity \mathbf{v}_s , and was originally proposed by Vinen [197, 198] and is well-accepted [202, 203]. It should be acknowledged that there are other treatments for \mathbf{v}_L proposed in literature different from the treatment incorporated here. For instance, \mathbf{v}_L being in the direction of \mathbf{v}_n with its amplitude proportional to v_{ns} is proposed elsewhere [177, 193, 204]. However, in the time scales of the present problem, the effects of such driftings is negligible and the selection of \mathbf{v}_L treatment does not affect the model [183]. Ultimately, the material derivative of the vortex line density, as expected for any physical property, must be equal to changes, i.e., generation and decay of quantized vortices. The terms on the right-hand side of Eq. 3.9 incorporate the generation, the decay, and the trigger of the initial growth of the line density [197], respectively.

It must be noted that the viscous terms [195] in Eqs. 3.1- 3.4 have been neglected as a consequence of the dominating effect of mutual friction on the heat transfer processes in He II. By linearizing Eqs. 3.1- 3.4, ignoring the effect of individual vortices (it is an accurate assumption for non-isothermal He II flows when vortex line density is relatively high[205, 206]), and assuming small-amplitude wave-form variations of $\mathbf{v}_{\mathbf{ns}}$ and s , a temperature-entropy wave mode (i.e., the second sound) can be derived [167]. Therefore, applying a heat flux pulse from a heater in He II generates a second-sound pulse where its amplitude ΔT is related to the heat flux.

Here, the process of transient heat transfer applied by a planar heater in He II is considered with regards to the system of governing equations (i.e., Eqs. 3.1- 3.9). The overall geometry of the problem is schematically shown in Fig. 3.1(a). A one-dimensional flow perpendicular to the heater surface is examined and small turbulent fluctuations are ignored [183]. The applied heat flux, q_h ,

generates a heat pulse of duration t_h , which propagates down stream in the channel. The coupled system entailed 5 equations and 5 unknowns, including 2 thermodynamic properties of He II state, 2 velocities of He II components, and vortex line density. Since all 5 equations contain first order spatial and temporal derivatives, in order to numerically solve the system in a discretized lattice, 5 initial and boundary conditions are needed. The initial conditions include the initial pressure and temperature, vortex line density and velocities are zero everywhere. A set the boundary conditions at the heater surface for the superfluid and normal fluid velocity are imposed, respectively, while the no-penetration condition is also satisfied:

$$\begin{cases} \mathbf{v}_s = -\mathbf{v}_n \rho_n / \rho_s, \\ \mathbf{v}_n = q_h / \rho_s T, \end{cases} \quad (3.10)$$

during $0 < t \leq t_h$; and $\mathbf{v}_n = \mathbf{v}_s = 0$ at $t > t_h$. An initial vortex-line density of $L_0 = 10^2 \text{ cm}^{-2}$ is also assumed, which is comparable to typical densities of remnant vortices in He II containers [207]. Indeed, the exact value of L_0 does not affect the simulation results for the range of q_h considered in our work [183]. The dynamic library HEPAK is used to calculate all of the thermodynamic properties of He II [196]. The values of the coefficients α_V and β_V as recommended here [208] are used in Eq. 3.9, which produces simulation results in good agreement with experimental observations.

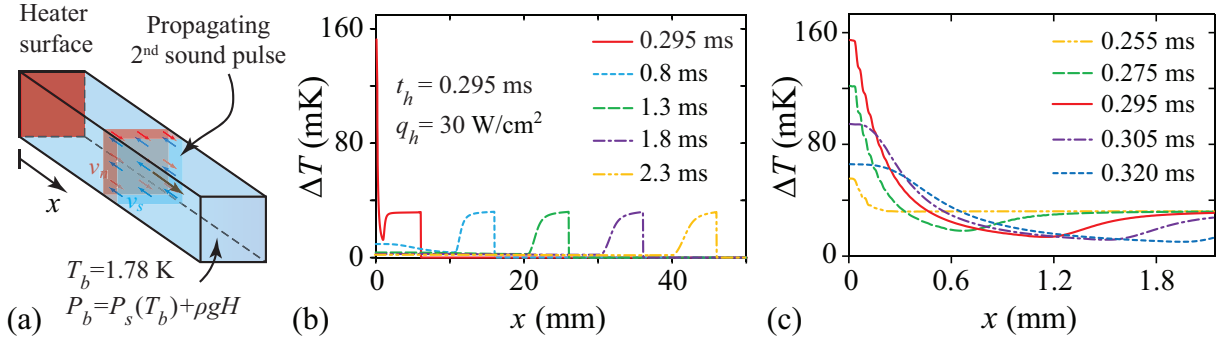


Fig. 3.1: (a) A schematic diagram of the planar heater placed in a He II channel where the bath temperature is $T_B = 1.78 \text{ K}$. A second sound generates and propagates downstream as a results of the applied heat flux. (b) Second sound propagation in space by time after applying a heat flux of $q_h = 30 \text{ W/cm}^2$ for a duration t_h . A temperature spike occurs at the heater surface as a result of the thermal layer development. (c) The spatial development of the thermal layer by time near the heater surface region where the temperature spike eventually reaches the saturation temperature.

The system of equations are numerically evolved with respect to the boundary conditions. The MacCormack's predictor-corrector scheme [209] is used which yields an accurate second order spatial

and temporal terms. To suppress numerical oscillations as a product of discontinuities arising at the second sound shock front, a flux-corrected transport method as described in [209] is incorporated. A reliable convergence of numerical results are achieved when the temporal step $\Delta t < 10^{-8}$ and the spatial step $\Delta x < 10^{-5}$. Considering our available computational power and in order to minimize computational costs without sacrificing accuracy (certain computational runs still take a week or more to complete), $\Delta t = 10^{-8}$ and $\Delta x = 10^{-5}$ are used. However, the study of critical phenomena reported in Part III have been subjected to extensive convergence check, and finer resolutions are frequently used in those cases to ensure the results remain independently unchanged. Furthermore, it must be noted that the mentioned resolutions are purposefully chosen to achieve a logical ration between spacial and temporal resolution.

The generated second-sound pulse and its subsequent propagation at later times, represented by the spatial profile of the temperature change, ΔT , as a consequence of an applied constant heat flux of $q_h = 30 \text{ W/cm}^2$ over a duration of $t_h = 0.295 \text{ ms}$ where a head pressure, $H = 1 \text{ m}$ and a bath temperature, $T_b = 1.78 \text{ K}$ are assumed, is shown in Fig. 3.1(b). ΔT near the heater surface for $t < t_h$ is shown in Fig. 3.1(c). As it can be seen, a rapid change of temperature is started at about $t = 250 \text{ ms}$ where the thermal layer starts building up locally as a response to the deposited heat near the heater surface. This accumulation of thermal energy is a consequence of the attenuation of second sound pulse due to the high density of vortex lines [183].

At each step of the evolving algorithm, $T_h + \delta T$ is compared to T_s , where T_h is the temperature of He II at the heater surface, δT is a sufficiently small specified temperature resolution, and T_s is saturation temperature for $1.25 \leq T \leq 2.17$, calculated using:

$$T_s = \sum_{i=0}^9 A_i \left[\frac{\ln P - B}{C} \right]^i, \quad (3.11)$$

where A_i , B , and C are known constants [199].

This numerical model was originally developed by Shiran Bao [183] in our lab, and has been used and modified where needed to study the recent problem.

CHAPTER 4

PEAK HEAT FLUX AND MODEL VALIDATION

For a given helium bath condition (i.e., T_b and H), the peak heat flux q^* depends on the heat-pulse duration t_h . To determine the correlation between q^* and t_h , we adopt a method by scanning t_h as illustrated in Fig. 4.1 (a). This figure shows the evolution of the thermodynamic state (P, T) of the He II at the first grid point $x = \Delta x$ for heat pulses with the same flux $q_h = 30 \text{ W/cm}^2$ but different duration t_h . All the curves start from the same initial state marked by the black open circle, i.e., $T|_{t=0} = T_b = 1.78 \text{ K}$ and $P|_{t=0} = P_b = P_s(T_b) + \rho g H$ where $P_s(T_b)$ is the saturation pressure at T_b and $H = 1 \text{ m}$. The He II states at the end of the heat pulses are marked by the filled circles of the respective colors. It is clear that when the heater turns on, there is a pressure drop followed by an increase of the He II temperature. As the heat pulse ends, the pressure spikes up in all the cases and the state curves evolve back to the starting point. Obviously, the He II state at the end of the heat pulse gets closer to the saturation line at larger t_h . We consider the boiling occurs when the state curve reaches the saturation line. For the example shown in Fig. 4.1 (a), the boiling occurs at $t_h = 0.297 \text{ ms}$.

By repeating the above analysis at various applied heat fluxes, we can determine the corresponding pulse durations beyond which boiling occurs. The results for $T_b = 1.78 \text{ K}$ and $H = 1 \text{ m}$ are collected in Fig. 4.1 (b). We see that when t_h is greater than about 10^{-4} s , q^* increases with decreasing t_h , which agrees with the trend reported in literature [184, 185, 187, 189, 190]. However, when the applied heat flux reaches a critical value $q_c^* \simeq 55 \text{ W/cm}^2$, we find surprisingly that the onset time of boiling suddenly jumps from about 10^{-4} s to an extremely small value. This value is found to be of the order $\Delta x/c_2$, i.e., the traveling time of the second-sound pulse to reach the first grid point. At heat fluxes higher than q_c^* , boiling always occurs on a similar time scale. This time scale $\Delta x/c_2$ suggests that the onset time for boiling would become arbitrarily small as one approaches the heater surface. However, in practice, the onset time will be limited by various factors such as the time takes for vapor bubbles to grow on the heater surface, which is about a few microseconds for the bubbles to reach a radius of about $10 \mu\text{m}$ [210, 211]. The appearance of the critical peak heat flux q_c^* and the associated sudden drop of the onset time of boiling to the

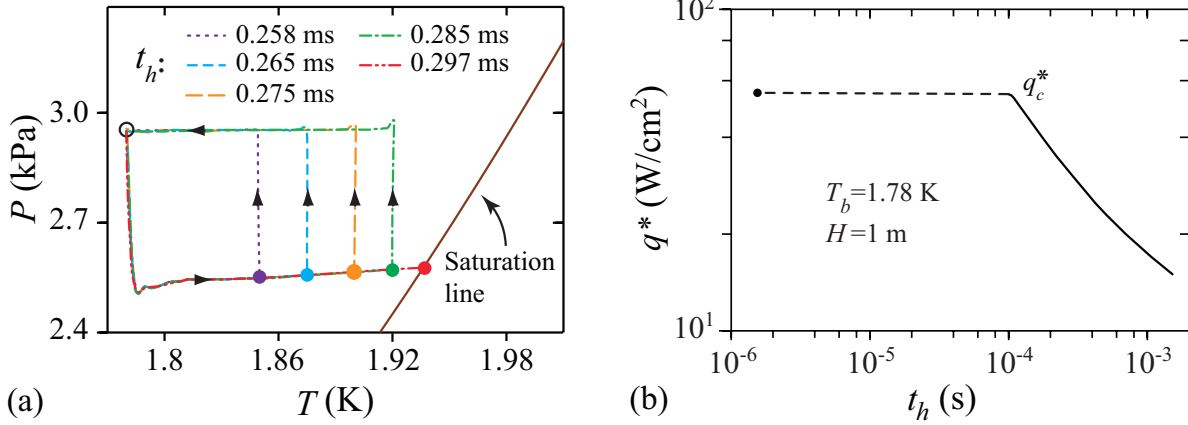


Fig. 4.1: (a) Evolution of the He II thermodynamics state at $x = \Delta x$ when heat pulses of $q = 30 \text{ W/cm}^2$ with different duration t_h are applied. The filled circles indicate the He II states at the end of the heat pulses. (b) The simulated curve showing the dependance of the peak heat flux q^* and the pulse duration t_h . The dashed line denotes that above a critical peak heat flux q_c^* (marked by the red diamond), the onset time of boiling suddenly drops to the order of $\Delta x/c_2$.

order of $\Delta x/c_2$ are previously unreported phenomena, which indicates the existence of an unusual mechanism of boiling in He II.

Before moving to the next section to present our systematic study of q_c^* , we would like to compare our model simulations with some available experimental data. In Fig. 4.2, we show the experimental data of q^* versus t_h obtained by Tsoi and Lutset [190] and by Shimazaki *et al* [189]. The work of Tsoi and Lutset adopted a thin-film nichrome heater (surface area: $3 \times 3 \text{ cm}^2$) immersed in He II at 1.794 K, and the boiling was detected by monitoring the pressure change in He II using a piezosensor. The experiment of Shimazaki *et al.* was conducted at $T_b = 2 \text{ K}$ and utilized a slightly smaller heater (area: $2.7 \times 2.7 \text{ cm}^2$), where the boiling was detected by measuring thermal shockwaves using a superconducting temperature sensor. The exact hydrostatic head pressures in these experiments were not reported. Nonetheless, we can perform simulations at the corresponding T_b with a range of H compatible with the expected He II depths estimated based on their setup schematics. The simulated q^* - t_h curves are shown in Fig. 4.2, which agree well with these experimental data. This agreement validates our model calculations. Note that due to the limited sensor response times, the sudden drop of the onset time of boiling at heat fluxes above q_c^* was not resolvable in these experiments.

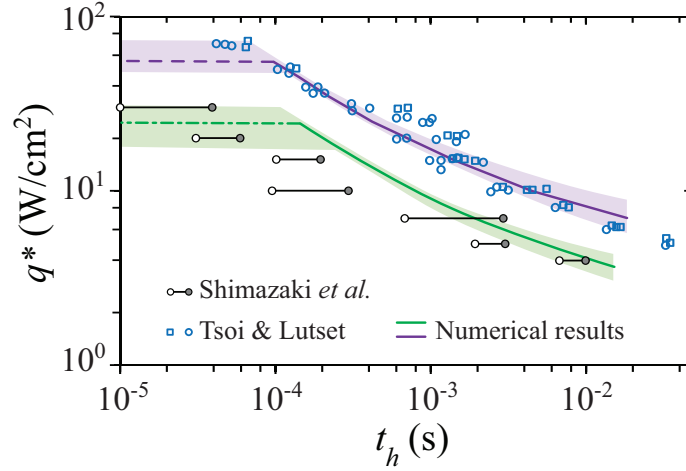


Fig. 4.2: Comparison of the simulated peak heat flux q^* and some relevant experimental data. The blue circles and squares are data obtained by Tsoi and Lutset at 1.794 K [190]. The open and filled circles are data obtained by Shimazaki *et al.* at 2 K [189], where the open circles indicate possible onset of the boiling while the filled circles denote firm observation of the boiling. The purple and the green curves are our simulation at $T_b = 1.794$ K with $H = 1$ m and $T_b = 2$ K with $H = 0.3$ m, respectively. The purple band indicates the span of the curve when H is varied in the range of 0.8 – 1.5 m, while the green band is for H in the range of 0.2 – 0.4 m.

CHAPTER 5

CRITICAL PEAK HEAT FLUX

In order to understand the physical mechanism underlying the critical peak heat flux q_c^* , we need to first conduct a systematic study on its dependance on the helium bath condition. For this purpose, we have repeated the afore-mentioned analysis at various T_b and H . In Fig. 5.1 (a), we show the calculated q^*-t_h curves for T_b in the range of 1.3 – 2.1 K with a fixed He II depth of $H = 0.5$ m. The critical peak heat flux q_c^* at each T_b is identified and marked by the filled circle. From this study, the dependance of q_c^* on T_b is obtained, which is shown in Fig. 5.1 (b). q_c^* first increases with increasing T_b before reaching a maximum at $T_b \simeq 1.95$ K. Then, q_c^* decreases as T_b further increases. The maximum value of q_c^* appears to be achieved at the bath temperature where the two fluids have about same densities. It is interesting to notice that He II has the highest effective thermal conductivity at this temperature as well.

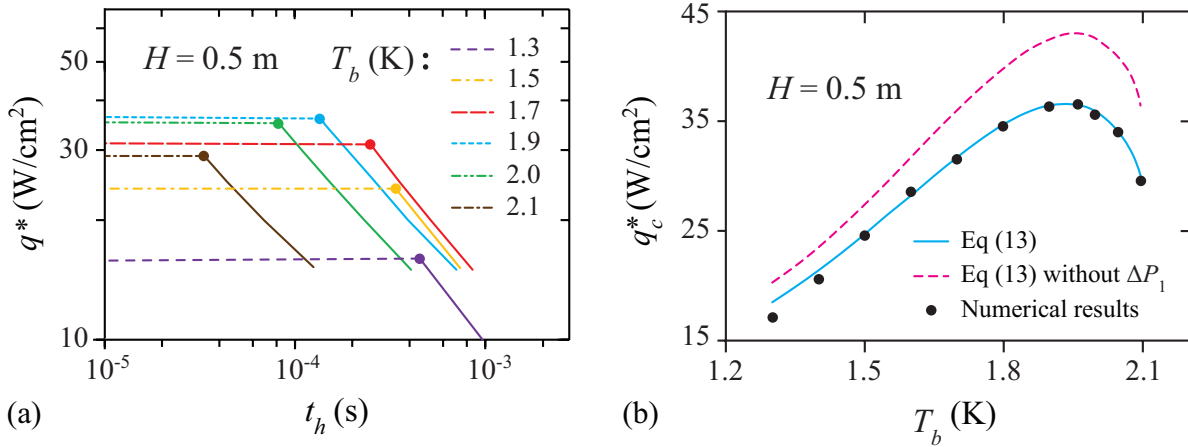


Fig. 5.1: (a) Calculated q^*-t_h curves at various T_b with a fixed He II depth $H = 0.5$ m. The critical peak heat flux q_c^* for each curve is marked by the filled circle of the respective color. (b) The obtained critical peak heat flux q_c^* as a function of T_b . The black dots are simulation data. The solid and the dashed curves are calculated using Eq. (5.6) with and without the ΔP_1 term, respectively.

When the He II depth H is changed, the dependance of q_c^* on T_b remains similar to that presented in Fig. 5.1 (b) but naturally the values change. To illustrate how q_c^* varies with H quantitatively, we fix the bath temperature at $T_b = 1.78$ K and calculate the q^*-t_h curves at various He II depth

H . Representative results for H in the range of 0.3 – 2 m are shown in Fig. 5.2 (a), where q_c^* can be determined (marked by the filled circles). The obtained q_c^* is then plotted as a function of H in Fig. 5.2 (b). It is clear that q_c^* increases monotonically with increasing H .

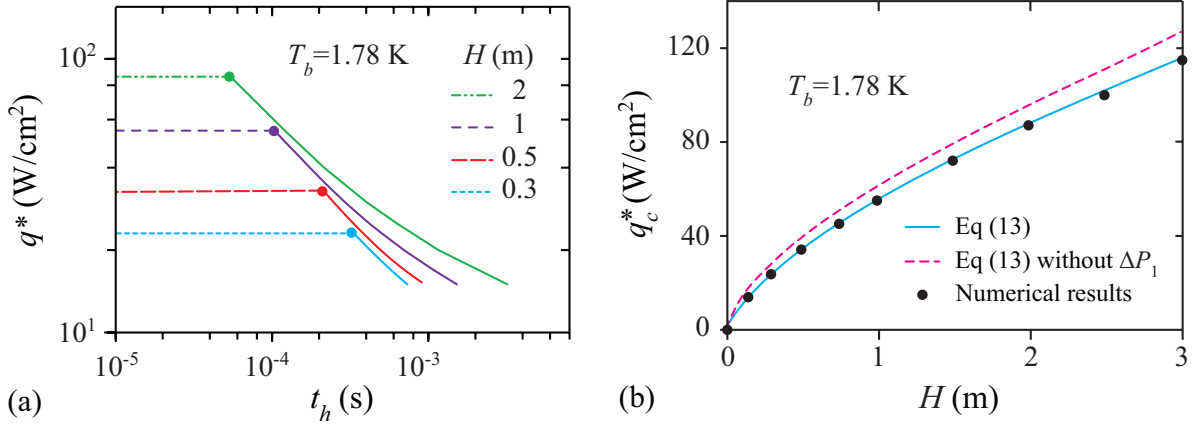


Fig. 5.2: (a) Calculated q^* - t_h curves at various H with a fixed bath temperature $T_b = 1.78$ K. The critical peak heat flux q_c^* for each curve is marked by the filled circle of the respective color. (b) The obtained critical peak heat flux q_c^* as a function of H . The black dots are simulation data. The solid and the dashed curves are calculated using Eq. (5.6) with and without the ΔP_1 term, respectively.

5.1 Explanation and theoretical model of critical peak heat flux

The studies presented in the previous sections show that the critical peak heat flux q_c^* depends on both T_b and H and is likely associated with the propagation of the second-sound pulse since the corresponding boiling time is on the order of $\Delta x/c_2$. To better understand the physical processes that controls q_c^* , we show in Fig. 5.3 (a) the evolution of the He II state adjacent to the heater (i.e., $x = \Delta x$) when the applied heat flux gradually increases. All the cases start from the same initial state as in Fig. 4.1 (a), i.e., $T = T_b = 1.78$ K and $P = P_s(T_b) + \rho g H$ with $H = 1$ m. In what follows, we present a few important features observed in this study.

First, when the heater turns on, there is a fast process during which the pressure drops by ΔP and the temperature increases by ΔT . This process occurs on a time scale of $\Delta x/c_2$. The end state of this fast process is marked by the asterisk for each curve in Fig. 5.3 (a). It is clear that the magnitudes of both ΔP and ΔT increase with increasing the heat flux q . To provide a more direct view of the fast process, we show the time evolution of the He II pressure, temperature, and the vortex-line density at $x = \Delta x$, 1 mm, and 2 mm for a representative case with $q_h = 50$ W/cm² in

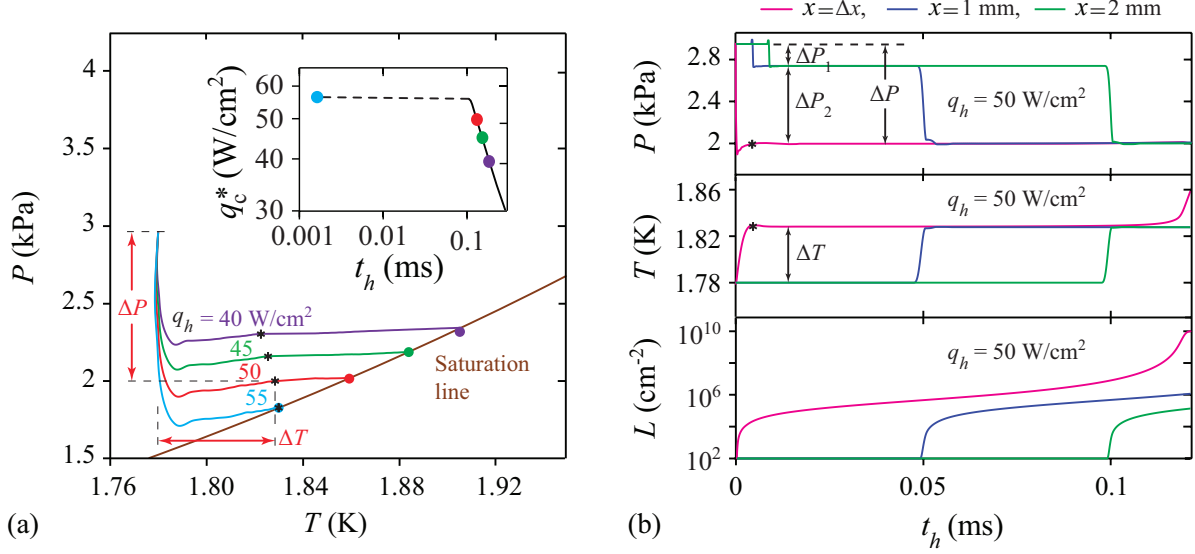


Fig. 5.3: (a) Evolution of the He II state at $x = \Delta x$ when heat pulses of different q_h are applied. The asterisk in each curve denotes the end state of the fast process, and the filled circle marks where the state curve reaches the saturation line. The inset shows the obtained correlation between q_c^* and t_h . (b) Time evolution of the He II pressure P , temperature T , and the vortex-line density L at $x = \Delta x$, 1 mm, and 2 mm for the case with $q_h = 50 \text{ W/cm}^2$. All the simulations are conducted at $T_b = 1.78 \text{ K}$ and $H = 1 \text{ m}$.

Fig. 5.3 (b). Following the fast process, the He II temperature and pressure remain nearly constant while the vortex-line density L gradually grows after an initial rapid increase. This initial increase of L is largely due to the generation term (i.e., the last term) in Eq. (3.9), which is also the reason why the exact value of the initial line density L_0 does not affect the simulation result. When L builds up to a sufficient level (i.e., of the order 10^8 cm^{-2}), the thermal layer starts to form and the He II temperature rapidly increases, which drives the He II state towards the saturation line. Interestingly, at the critical peak heat flux $q_c^* \simeq 55 \text{ W/cm}^2$, the state curve of the He II adjacent to the heater reaches the saturation line during the fast process without involving any subsequent slower heating process. Therefore, the onset time for boiling suddenly drops to the order of $\Delta x/c_2$ (see the inset in Fig. 5.3 (a)). At heat fluxes higher than q_c^* , the boiling is largely controlled by the sudden drop in pressure across the saturation line, a phenomenon that is known as cavitation [212].

Based on the physical picture presented above, we can indeed develop an analytical model to evaluate q_c^* . When the heater turns on, a second-sound pulse emerges from the heater surface. At short times when the vortex-line density near the heater is relatively low, the temperature increment

ΔT within the second-sound pulse zone is related to the applied heat flux q_h as [167]:

$$q_h = c_2 T (\rho_s|_{2nd} - \rho_s|_{bath}) \simeq c_2 \rho C_p \Delta T + \frac{1}{2} v_{ns}^2 c_2 T \left(\frac{\partial \rho_n}{\partial T} \right) \Big|_{T_b + \Delta T, P_b}, \quad (5.1)$$

where the subscripts “2nd” and “bath” denote the parameters evaluated in the second-sound pulse zone and in the He II bath, respectively. $C_p = T(\partial s/\partial T)_P$ is the specific heat of He II, and the second term in the above equation comes from the correction term in Eq. (3.6). Within the second-sound pulse zone, a counterflow of the two fluids establishes as shown schematically in Fig. 5.4. The velocities of the two fluids are given by $v_n = q_h/(\rho_s T)|_{T_b + \Delta T}$ and $v_s = -v_n \rho_n/\rho_s$. Accordingly to Eq. (3.2), the finite v_n and v_s lead to a pressure change ΔP_2 in the second-sound pulse zone as given by:

$$\Delta P_2 = -(\rho_s v_s^2 + \rho_n v_n^2) \simeq -\frac{q_h^2 \rho_n}{s^2 T^2 \rho \rho_s} \Big|_{T_b + \Delta T, P_b}, \quad (5.2)$$

This pressure drop is essentially a manifestation of the Bernoulli effect due to the motion of the two fluids in the second-sound zone.

Besides the effects due to the second-sound pulse, there is another subtle effect. Note that He II has a negative thermal expansion coefficient at temperatures above about 1.1 K [199]. Therefore, the He II density ρ in the second-sound zone must increase due to the temperature rise ΔT , which requires a mass flow towards this region. To supply the mass, a first-sound pulse is generated where the two fluids move in phase at a velocity \mathbf{v} towards the second-sound wavefront, as shown in Fig. 5.4. The mass flux $\rho|\mathbf{v}|$ should balance the needed mass associated with the expansion of the second-sound pulse zone, i.e., $\rho|\mathbf{v}| = c_2(\rho|_{2nd} - \rho|_{1st})$. This finite $\rho|\mathbf{v}|$ leads to a pressure drop ΔP_1 in the first-sound pulse zone. To the lowest order in \mathbf{v} , one can derive ΔP_1 from Eq. (3.2) as:

$$\Delta P_1 \simeq -\rho c_1 |\mathbf{v}| = -c_1 c_2 (\rho|_{2nd} - \rho|_{1st}) \simeq -c_1 c_2 \left[(\rho|_{2nd}^{(s)} - \rho|_{1st}^{(s)}) + \frac{\rho^2 v_{ns}^2}{2} \left(\frac{\partial \rho_n / \rho}{\partial P} \right) \Big|_{2nd} \right], \quad (5.3)$$

where c_1 is the speed of the first sound in He II (i.e., about 231 m/s at 1.78 K). The interaction of these pressure drops in the second sound region can be directly derived from the governing equations (Eq. 3.3). At the first sound wavefront, the fluid is at rest in front of the wave and has a finite co-flow velocity inside the wave. Therefore, Eq. 3.2 can be simplified as:

$$\frac{0 - \rho|\mathbf{v}|}{\delta t} + \nabla(\rho_s v_s^2 + \rho_n v_n^2) + \frac{P_b - (P_b + \Delta P_1)}{\delta x_1} = 0, \quad (5.4)$$

which yields $\Delta P_1 = -c_1 \rho |\mathbf{v}|$ where δx_1 is a small distance the first sound propagates during a small time δt . At the second sound wavefront, there is co-flow in front of the wave and counterflow inside

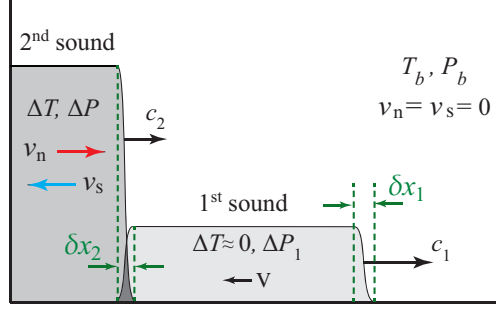


Fig. 5.4: A schematic diagram showing the temperature and pressure changes as well as the motion of the two fluids in the first-sound and the second-sound pulse zones.

the wave. Therefore, Eq. 3.2 can be simplified as:

$$\frac{\rho|\mathbf{v}|-0}{\delta t} + \nabla(\rho_s v_s^2 + \rho_n v_n^2) \frac{\Delta P_2 / \delta x_2}{\delta x_2} + \frac{(P_b + \Delta P_1) - (P_b + \Delta P)}{\delta x_2} = 0, \quad (5.5)$$

where δx_2 is a small distance the second sound propagates during δt . Substituting ΔP_1 , $\Delta P = (1 - c_2/c_1)\Delta P_1 + \Delta P_2$ is yielded. Since $c_1 \gg c_2$, hence the ΔP_1 prefactor is close to 1 at temperature above 0.8 K. This can be clearly observed in Fig. 5.3 (b) at $x = 1$ mm (and $x = 2$ mm), where the first-sound pulse and the second-sound pulse arrive at different times.

At the critical peak heat flux q_c^* , the temperature increment ΔT and the total pressure drop ΔP associated with the second-sound pulse would drive the He II from the initial state (T_b, P_b) to the saturation line upon its arrival at the first grid point. Therefore, the following equation must hold:

$$P_s(T_b) + \rho g H + \Delta P = P_s(T_b + \Delta T). \quad (5.6)$$

where q_c^* enters the equation through ΔT , ΔP_1 , and ΔP_2 via Eqs. (5.1)-(5.3). Using this model, we have calculated q_c^* as a function T_b at $H = 0.5$ m and as a function of H at $T_b = 1.78$ K. The results are included in Fig. 5.1 (b) and Fig. 5.2 (b) as the solid curves. Excellent agreement between the model calculation and the simulated q_c^* values is observed, which proves that our understanding of the mechanism underlying the critical peak heat flux is correct. To see how large the first-sound effect is, we have also repeated the calculation using Eq. (5.6) but without the ΔP_1 term. The results are shown as the dashed curves in Fig. 5.1 (b) and Fig. 5.2 (b). Obviously, the first-sound effect is non-negligible at these large heat fluxes.

CHAPTER 6

SUMMARY AND FUTURE WORK

We have conducted a numerical study on 1D transient heat transfer in He II from a planar heater. The peak heat flux q^* for the onset of boiling in He II is determined as a function of the heat-pulse duration t_h . A major finding in our study is the observation of a critical peak heat flux q_c^* above which boiling occurs almost instantaneously. Our analysis shows that the boiling at heat fluxes lower than q_c^* is caused by a heating process, which is associated with the relatively slow buildup of the quantized vortices and the thermal layer in front of the heater. When the applied heat flux is higher than q_c^* , the boiling is essentially a cavitation on the heater surface due to the combined effects of the first-sound and the second-sound waves in He II. An analytical model for evaluating q_c^* was developed which accurately predicted the simulated q_c^* values at various He II T_b and P_h . Inspired by this work, a question to be addressed next is how the boiling physics may change in non-homogeneous heat transfer in He II. Understanding the behavior of the peak heat flux in these geometries could benefit research work such as quench-spot detection on He II cooled superconducting accelerator cavities [213] and the heat and mass transfer processes due to a vacuum failure in He II cooled accelerator beamline tubes [214].

There are also some other interesting studies that can follow what the recent work has started.

1. A numerical study of a minimum heat flux below which boiling would never happen. This study can be conducted in a 1D channel of He II with a finite length of L connected to a large He II bath can be conducted. There are experimental studies suggesting the existence of such minimum heat flux [53] that can be used to validate the model. Once the model is verified, a more interesting study of the minimum heat flux in nonhomogeneous geometries can be conducted. Any finding produced from such study would be a first, yet of great significance for nonhomogeneous applications.
2. A comprehensive review of high heat flux applications in He II may be conducted. Through such study, one can analyze the typical heat fluxes used in research or engineering applications, and subsequently compare them to the results obtained in recent work. The occurrence of boiling in He II can impact research studies or engineering applications negatively.

BIBLIOGRAPHY

- [1] Hamid Sanavandi et al. “A cryogenic-helium pipe flow facility with unique double-line molecular tagging velocimetry capability.” In: *Review of Scientific Instruments* 91.5 (2020), p. 053901.
- [2] D. R. Tilley and J. Tilley. *Superfluidity and Superconductivity*. Second. Graduate Student Series in Physics. Bristol: Adam Hilger Ltd, 1986.
- [3] Chris J Swanson et al. “Pipe flow measurements over a wide range of Reynolds numbers using liquid helium and various gases.” In: *Journal of Fluid Mechanics* 461 (2002), pp. 51–60.
- [4] N Furuichi et al. “Friction factor and mean velocity profile for pipe flow at high Reynolds numbers.” In: *Physics of Fluids* 27.9 (2015), p. 095108.
- [5] S Fuzier, B Baudouy, and SW Van Sciver. “Steady-state pressure drop and heat transfer in He II forced flow at high Reynolds number.” In: *Cryogenics* 41.5-6 (2001), pp. 453–458.
- [6] Robert A Kilgore. “Cryogenic wind tunnels-a brief review.” In: *Advances in cryogenic engineering* (1994), pp. 63–70.
- [7] Gregory P Bewley, Daniel P Lathrop, and Katepalli R Sreenivasan. “Visualization of quantized vortices.” In: *Nature* 441.7093 (2006), pp. 588–588.
- [8] MV Zagarola and AJ Smits. “Scaling of the mean velocity profile for turbulent pipe flow.” In: *Physical review letters* 78.2 (1997), p. 239.
- [9] Wei Guo et al. “Visualization of two-fluid flows of superfluid helium-4.” In: *Proceedings of the National Academy of Sciences* 111.Supplement 1 (2014), pp. 4653–4658.
- [10] N Furuichi et al. “Further experiments for mean velocity profile of pipe flow at high Reynolds number.” In: *Physics of Fluids* 30.5 (2018), p. 055101.
- [11] Russell J Donnelly. *Quantized vortices in helium II*. Vol. 2. Cambridge University Press, 1991.
- [12] William Frank Vinen. “Mutual friction in a heat current in liquid helium II I. Experiments on steady heat currents.” In: *Proceedings of the Royal Society of London. Series A. Mathematical and Physical Sciences* 240.1220 (1957), pp. 114–127.
- [13] WF Vinen and JJ Niemela. “Quantum turbulence.” In: *Journal of low temperature physics* 128.5 (2002), pp. 167–231.

- [14] WS Dennis et al. “Spectroscopic identification of excited atomic and molecular states in electron-bombarded liquid helium.” In: *Physical Review Letters* 23.19 (1969), p. 1083.
- [15] Tao Zhang and Steven W Van Sciver. “Large-scale turbulent flow around a cylinder in counterflow superfluid ^4He (He (II)).” In: *Nature Physics* 1.1 (2005), pp. 36–38.
- [16] Matthew S Paoletti et al. “Velocity statistics distinguish quantum turbulence from classical turbulence.” In: *Physical review letters* 101.15 (2008), p. 154501.
- [17] Matthew S Paoletti et al. “Visualization of superfluid helium flow.” In: *Journal of the physical Society of Japan* 77.11 (2008), pp. 111007–111007.
- [18] M La Mantia et al. “Lagrangian accelerations of particles in superfluid turbulence.” In: *Journal of Fluid Mechanics* 717 (2013).
- [19] Demosthenes Kivotides. “Motion of a spherical solid particle in thermal counterflow turbulence.” In: *Physical Review B* 77.17 (2008), p. 174508.
- [20] J Gao et al. “Producing and imaging a thin line of He_2^* molecular tracers in helium-4.” In: *Review of Scientific Instruments* 86.9 (2015), p. 093904.
- [21] Alex Marakov et al. “Visualization of the normal-fluid turbulence in counterflowing superfluid He 4.” In: *Physical Review B* 91.9 (2015), p. 094503.
- [22] J Gao, W Guo, and WF Vinen. “Determination of the effective kinematic viscosity for the decay of quasiclassical turbulence in superfluid He 4.” In: *Physical Review B* 94.9 (2016), p. 094502.
- [23] J Gao et al. “Challenging problem in quantum turbulence: Decay of counterflow in superfluid ^4He .” In: *JETP Lett* 103 (2016), p. 648.
- [24] J Gao et al. “Energy spectrum of thermal counterflow turbulence in superfluid helium-4.” In: *Physical Review B* 96.9 (2017), p. 094511.
- [25] Emil Varga et al. “Intermittency enhancement in quantum turbulence in superfluid He 4.” In: *Physical Review Fluids* 3.9 (2018), p. 094601.
- [26] J Gao et al. “Dissipation in quantum turbulence in superfluid He 4 above 1 K.” In: *Physical Review B* 97.18 (2018), p. 184518.
- [27] S Bao et al. “Statistics of turbulence and intermittency enhancement in superfluid He 4 counterflow.” In: *Physical Review B* 98.17 (2018), p. 174509.
- [28] M Zagarola et al. “Experiments in high Reynolds number turbulent pipe flow.” In: *34th Aerospace Sciences Meeting and Exhibit*. 1996, p. 654.

- [29] Lev Davidovich Landau and Evgenii Mikhailovich Lifshitz. *Fluid Mechanics: Landau and Lifshitz: Course of Theoretical Physics, Volume 6*. Vol. 6. Elsevier, 2013.
- [30] Beverley J Mckeen et al. “Further observations on the mean velocity distribution in fully developed pipe flow.” In: *Journal of Fluid Mechanics* 501 (2004), pp. 135–147.
- [31] Jens M Österlund et al. “A note on the overlap region in turbulent boundary layers.” In: *Physics of Fluids* 12.1 (2000), pp. 1–4.
- [32] Ramis Örlü et al. “Reynolds stress scaling in pipe flow turbulence—first results from CIC-LoPE.” In: *Philosophical Transactions of the Royal Society A: Mathematical, Physical and Engineering Sciences* 375.2089 (2017), p. 20160187.
- [33] Jason Patrick Monty. “Developments in smooth wall turbulent duct flows.” PhD thesis. Citeseer, 2005.
- [34] Xiaohua Wu and Parviz Moin. “A direct numerical simulation study on the mean velocity characteristics in turbulent pipe flow.” In: *Journal of Fluid Mechanics* 608 (2008), pp. 81–112.
- [35] Myoungkyu Lee and Robert D Moser. “Direct numerical simulation of turbulent channel flow up to.” In: *Journal of fluid mechanics* 774 (2015), pp. 395–415.
- [36] Yoshinobu Yamamoto and Yoshiyuki Tsuji. “Numerical evidence of logarithmic regions in channel flow at $Re\tau = 8000$.” In: *Physical Review Fluids* 3.1 (2018), p. 012602.
- [37] Hassan M Nagib and Kapil A Chauhan. “Variations of von Kármán coefficient in canonical flows.” In: *Physics of fluids* 20.10 (2008), p. 101518.
- [38] Martin Oberlack et al. “Turbulence Statistics of Arbitrary Moments of Wall-Bounded Shear Flows: A Symmetry Approach.” In: *Physical Review Letters* 128.2 (2022), p. 024502.
- [39] John Kim. “Progress in pipe and channel flow turbulence, 1961–2011.” In: *Journal of Turbulence* 13 (2012), N45.
- [40] J Maurer and P Tabeling. “Local investigation of superfluid turbulence.” In: *EPL (Europhysics Letters)* 43.1 (1998), p. 29.
- [41] WF Vinen. “An introduction to quantum turbulence.” In: *Journal of Low Temperature Physics* 145.1 (2006), pp. 7–24.
- [42] Carlo F Barenghi et al. “Superfluid vortex lines in a model of turbulent flow.” In: *Physics of fluids* 9.9 (1997), pp. 2631–2643.
- [43] GW Stagg, NG Parker, and CF Barenghi. “Superfluid boundary layer.” In: *Physical Review Letters* 118.13 (2017), p. 135301.

- [44] T Xu and SW Van Sciver. “Particle image velocimetry measurements of the velocity profile in He II forced flow.” In: *Physics of fluids* 19.7 (2007), p. 071703.
- [45] TV Chagovets and SW Van Sciver. “Visualization of He II forced flow around a cylinder.” In: *Physics of Fluids* 27.4 (2015), p. 045111.
- [46] Mark V Zagarola and Alexander J Smits. “Mean-flow scaling of turbulent pipe flow.” In: *Journal of Fluid Mechanics* 373 (1998), pp. 33–79.
- [47] MA Shockling, JJ Allen, and AJ Smits. “Roughness effects in turbulent pipe flow.” In: *Journal of Fluid Mechanics* 564 (2006), pp. 267–285.
- [48] Johann Nikuradse et al. “Laws of flow in rough pipes.” In: (1950).
- [49] F Kong and J Schetz. “Turbulent boundary layer over solid and porous surfaces with small roughness.” In: *19th Aerospace Sciences Meeting*. 1982, p. 418.
- [50] L Chan et al. “A systematic investigation of roughness height and wavelength in turbulent pipe flow in the transitionally rough regime.” In: *Journal of Fluid Mechanics* 771 (2015), pp. 743–777.
- [51] Manuj Awasthi et al. “Pressure fluctuations produced by forward steps immersed in a turbulent boundary layer.” In: *Journal of Fluid Mechanics* 756 (2014), pp. 384–421.
- [52] S Wilkinson. “Influence of wall permeability on turbulent boundary-layer properties.” In: *21st Aerospace Sciences Meeting*. 1983, p. 294.
- [53] Steven W. Van Sciver. *Helium Cryogenics*. Second. International Cryogenics Monograph Series. New York: Springer, 2012.
- [54] JC Hill, O Heybey, and GK Walters. “Evidence of metastable atomic and molecular bubble states in electron-bombarded superfluid liquid helium.” In: *Physical Review Letters* 26.20 (1971), p. 1213.
- [55] AV Benderskii et al. “A direct interrogation of superfluidity on molecular scales.” In: *The Journal of chemical physics* 117.3 (2002), pp. 1201–1213.
- [56] DN McKinsey et al. “Radiative decay of the metastable He 2 ($a\ 3\ \Sigma\ u+$) molecule in liquid helium.” In: *Physical Review A* 59.1 (1999), p. 200.
- [57] SG Kafanov, A Ya Parshin, and Igor A Todoshchenko. “Structure and dynamics of the He 2*($a\ 3\Sigma\ u+$) molecular complex in condensed phases of helium.” In: *Journal of Experimental and Theoretical Physics* 91.5 (2000), pp. 991–999.
- [58] Wei Guo and Andrei I Golov. “Shape fluctuations and optical transition of He 2* excimer tracers in superfluid He 4.” In: *Physical Review B* 101.6 (2020), p. 064515.

- [59] DE Zmeev et al. “Excimers He_2^* as Tracers of Quantum Turbulence in He 4 in the $T=0$ Limit.” In: *Physical review letters* 110.17 (2013), p. 175303.
- [60] DE Zmeev et al. “Observation of crossover from ballistic to diffusion regime for excimer molecules in superfluid 4He .” In: *Journal of Low Temperature Physics* 171.3 (2013), pp. 207–213.
- [61] Richard B Miles and and Walter R Lempert. “Quantitative flow visualization in unseeded flows.” In: *Annual review of fluid mechanics* 29.1 (1997), pp. 285–326.
- [62] Manoochehr M Koochesfahani and Daniel G Nocera. “Molecular tagging velocimetry maps fluid flows.” In: *Laser focus world* 37.6 (2001), pp. 103–109.
- [63] R Miles, W Lempert, and B Zhang. “Turbulent structure measurements by RELIEF flow tagging.” In: *Fluid Dynamics Research* 8.1-4 (1991), p. 9.
- [64] James B Michael et al. “Femtosecond laser electronic excitation tagging for quantitative velocity imaging in air.” In: *Applied optics* 50.26 (2011), pp. 5158–5162.
- [65] Andrea G Hsu et al. “Two-component molecular tagging velocimetry utilizing NO fluorescence lifetime and NO 2 photodissociation techniques in an underexpanded jet flowfield.” In: *Applied Optics* 48.22 (2009), pp. 4414–4423.
- [66] Marc C Ramsey and Robert W Pitz. “Template matching for improved accuracy in molecular tagging velocimetry.” In: *Experiments in fluids* 51.3 (2011), pp. 811–819.
- [67] AM ElBaz and RW Pitz. “N₂O molecular tagging velocimetry.” In: *Applied Physics B* 106.4 (2012), pp. 961–969.
- [68] Robert W Pitz et al. “Unseeded molecular flow tagging in cold and hot flows using ozone and hydroxyl tagging velocimetry.” In: *Measurement Science and technology* 11.9 (2000), p. 1259.
- [69] Peter C Hill. “Ultraviolet continua of helium molecules.” In: *Physical Review A* 40.9 (1989), p. 5006.
- [70] DN McKinsey et al. “Trace detection of metastable helium molecules in superfluid helium by laser-induced fluorescence.” In: *Physical review letters* 95.11 (2005), p. 111101.
- [71] Yuan Tang et al. “Statistical properties of homogeneous and isotropic turbulence in He II measured via particle tracking velocimetry.” In: *Physical Review Fluids* 5.8 (2020), p. 084602.
- [72] W Guo et al. “Metastable Helium Molecules as Tracers in Superfluid He 4.” In: *Physical review letters* 102.23 (2009), p. 235301.
- [73] WG Rellergert et al. “Detection and imaging of He 2 molecules in superfluid helium.” In: *Physical review letters* 100.2 (2008), p. 025301.

- [74] Wade G Rellergert. *Detecting and imaging helium molecules in superfluid helium by laser-induced fluorescence*. Yale University, 2009.
- [75] Wei Guo et al. “Visualization study of counterflow in superfluid He 4 using metastable helium molecules.” In: *Physical review letters* 105.4 (2010), p. 045301.
- [76] W Guo et al. “Studying the normal-fluid flow in helium-II using metastable helium molecules.” In: *Journal of Low Temperature Physics* 158.1 (2010), pp. 346–352.
- [77] W Guo et al. “Visualization technique for determining the structure functions of normal-fluid turbulence in superfluid helium-4.” In: *Journal of Low Temperature Physics* 171.5 (2013), pp. 497–503.
- [78] AV Benderskii et al. “Photodynamics in superfluid helium: Femtosecond laser-induced ionization, charge recombination, and preparation of molecular Rydberg states.” In: *The Journal of chemical physics* 110.3 (1999), pp. 1542–1557.
- [79] Sidney A Self. “Focusing of spherical Gaussian beams.” In: *Applied optics* 22.5 (1983), pp. 658–661.
- [80] RB Hill and JC Klewicki. “Data reduction methods for flow tagging velocity measurements.” In: *Experiments in Fluids* 20.3 (1996), pp. 142–152.
- [81] AJ Smits et al. “Spatial resolution correction for wall-bounded turbulence measurements.” In: *Journal of Fluid Mechanics* 676 (2011), pp. 41–53.
- [82] Marcus Hultmark et al. “Turbulent pipe flow at extreme Reynolds numbers.” In: *Physical review letters* 108.9 (2012), p. 094501.
- [83] Jian Gao. “Visualization Study Of Thermal Counterflow Turbulence In Superfluid 4 He.” PhD thesis. The Florida State University, 2017.
- [84] Wei Guo. “Molecular tagging velocimetry in superfluid helium-4: Progress, issues, and future development.” In: *Journal of Low Temperature Physics* 196.1 (2019), pp. 60–72.
- [85] Patrick Hammer et al. “A multi-time-delay approach for correction of the inherent error in single-component molecular tagging velocimetry.” In: *Measurement Science and Technology* 24.10 (2013), p. 105302.
- [86] Hendrik Tennekes, John Leask Lumley, Jonh L Lumley, et al. *A first course in turbulence*. MIT press, 1972.
- [87] Shinichi Ikawa and Makoto Tsubota. “Coflow turbulence of superfluid He 4 in a square channel: Vortices trapped on a cylindrical attractor.” In: *Physical Review B* 93.18 (2016), p. 184508.

- [88] F.M. White. *Fluid Mechanics*. McGraw-Hill International Editions. WCB/McGraw-Hill, 1999. ISBN: 9780070697164. URL: https://books.google.com/books?id=fa%5C_pAAAAAAAJ.
- [89] BJ McKeon et al. “Friction factors for smooth pipe flow.” In: *Journal of Fluid Mechanics* 511 (2004), pp. 41–44.
- [90] Chris J Swanson, Russell J Donnelly, and Gary G Ihas. “Turbulent pipe flow of He I and He II.” In: *Physica B: Condensed Matter* 284 (2000), pp. 77–78.
- [91] PL Walstrom et al. “Turbulent flow pressure drop in various He II transfer system components.” In: *Cryogenics* 28.2 (1988), pp. 101–109.
- [92] Paul T Boggs et al. “A computational examination of orthogonal distance regression.” In: *Journal of Econometrics* 38.1-2 (1988), pp. 169–201.
- [93] Roger Bruce Dean. “Reynolds number dependence of skin friction and other bulk flow variables in two-dimensional rectangular duct flow.” In: (1978).
- [94] ES Zanoun. “Answers to some open questions in wall-bounded laminar and turbulent shear flows.” In: *Doctor-Ingenieur, Univ. Erlangen-Nurnberg, Erlangen* (2003).
- [95] OC Jones Jr. “An improvement in the calculation of turbulent friction in rectangular ducts.” In: (1976).
- [96] NT Obot. “Determination of incompressible flow friction in smooth circular and noncircular passages: A generalized approach including validation of the nearly century old hydraulic diameter concept.” In: (1988).
- [97] JP Hartnett, JCY Koh, and ST McComas. “A comparison of predicted and measured friction factors for turbulent flow through rectangular ducts.” In: (1962).
- [98] Nicholas Metropolis and Stanislaw Ulam. “The monte carlo method.” In: *Journal of the American statistical association* 44.247 (1949), pp. 335–341.
- [99] Brindesh Dhruva, Yoshiyuki Tsuji, and Katepalli R Sreenivasan. “Transverse structure functions in high-Reynolds-number turbulence.” In: *Physical Review E* 56.5 (1997), R4928.
- [100] Siegfried Grossmann, Detlef Lohse, and Achim Reeh. “Different intermittency for longitudinal and transversal turbulent fluctuations.” In: *Physics of fluids* 9.12 (1997), pp. 3817–3825.
- [101] T. G. Hammond et al. “Gene expression in space.” In: *Nat. Med.* 5 ((1999)), pp. 359–359. DOI: 10.1038/7331.
- [102] R. J. White and M. Averner. “Humans in space.” In: *Nature* 409 ((2001)), pp. 1115–1118. DOI: 10.1038/35059243.

- [103] D. Williams et al. “Acclimation during space flight: Effects on human physiology.” In: *Can. Med. Assoc. J.* 180.13 ((2009)), pp. 1317–1323. DOI: 10.1503/cmaj.090628.
- [104] M. Stavnichuk et al. “A systematic review and meta-analysis of bone loss in space travelers.” In: *npj Microgravity* 6 ((2020)), pp. 1–9.
- [105] B. R. Unsworth and P. I. Lelkes. “Growing tissues in microgravity.” In: *Nat. Med.* 4 ((1998)), pp. 901–907. DOI: 10.1038/nm0898-901.
- [106] A. R. Nelson and N. R. Gokhale. “Oscillation frequencies of freely suspended water drops.” In: *J. Geophys. Res.* 77.15 ((1972)), pp. 2724–2727.
- [107] H. A. Snyder. “Effect of sloshing on the mechanics of dewar systems in low-gravity.” In: *Cryogenics* 41.11 ((2001)), pp. 825–832. DOI: [https://doi.org/10.1016/S0011-2275\(01\)00174-6](https://doi.org/10.1016/S0011-2275(01)00174-6).
- [108] R. Siegel. “Effects of Reduced Gravity on Heat Transfer.” In: *Adv. Heat Transf.* Vol. 4. Elsevier, (1967), pp. 143–228. DOI: [https://doi.org/10.1016/S0065-2717\(08\)70274-0](https://doi.org/10.1016/S0065-2717(08)70274-0).
- [109] H. Ohta and S. Baba. “Boiling experiments under microgravity conditions.” In: *Exp. Heat Transf.* 26.2-3 ((2013)), pp. 266–295.
- [110] D. Obreschkow et al. “Cavitation Bubble Dynamics inside Liquid Drops in Microgravity.” In: *Phys. Rev. Lett.* 97 (9 (2006)), p. 094502. DOI: 10.1103/PhysRevLett.97.094502.
- [111] B. P. Matisak et al. “The microgravity environment: Its prediction, measurement, and importance to materials processing.” In: *J. Cryst. Growth* 174.1 ((1997)), pp. 90–95. ISSN: 0022-0248. DOI: [https://doi.org/10.1016/S0022-0248\(96\)01083-4](https://doi.org/10.1016/S0022-0248(96)01083-4).
- [112] V. I. Strelov et al. “Crystallization in space: Results and prospects.” In: *Crystallogr. Rep.* 59.1 ((2014)), pp. 781–806. DOI: 10.1134/S1063774514060285.
- [113] National Research Council of The National Academia. *Assessment of NASA’s Mars Architecture 2007-2016*. The National Academies Press, (2006). ISBN: 978-0-309-10273-5. DOI: 10.17226/11717. URL: <https://www.nap.edu/catalog/11717/assessment-of-nasas-mars-architecture-2007-2016>.
- [114] A. Witze. “NASA plans Mars sample-return rover.” In: *Nature News* 509.7500 (2014), p. 272.
- [115] E. Musk. “Making Life Multi-Planetary.” In: *New Space* 6.1 ((2018)), pp. 2–11. DOI: 10.1089/space.2018.29013.emu.
- [116] J. P. Vandenbrink and J. Z. Kiss. “Space, the final frontier: A critical review of recent experiments performed in microgravity.” In: *Plant Sci.* 243 ((2016)), pp. 115–119.
- [117] N. J. Penley, C. P. Schafer, and J. F. Bartoe. “The international space station as a microgravity research platform.” In: *Acta Astronaut.* 50.11 ((2002)), pp. 691–696.

- [118] F. Ferranti, M. Del Bianco, and C. Pacelli. “Advantages and Limitations of Current Microgravity Platforms for Space Biology Research.” In: *Appl. Sci.* 11.1 ((2021)), p. 68.
- [119] D. E. Melnikov et al. “Thermovibrational Convection in Microgravity: Preparation of a Parabolic Flight Experiment.” In: *Microgravity Sci. Technol.* 20 ((2008)), pp. 29–39. DOI: 10.1007/s12217-008-9011-x.
- [120] M. Shelhamer. “Parabolic flight as a spaceflight analog.” In: *J. Appl. Physiol.* 120.12 ((2016)), pp. 1442–1448. DOI: 10.1152/jappphysiol.01046.2015.
- [121] H. Selig, H. Dittus, and C. Lämmerzahl. “Drop tower microgravity improvement towards the nano-*g* level for the MICROSCOPE payload tests.” In: *Microgravity Sci. Technol.* 22.4 ((2010)), pp. 539–549.
- [122] T. Y. Liu et al. “Microgravity level measurement of the Beijing drop tower using a sensitive accelerometer.” In: *Sci. Rep.* 6.1 ((2016)), pp. 1–9.
- [123] E. Fuhrmann and M. Dreyer. “Description of the Sounding Rocket Experiment - SOURCE.” In: *Microgravity Sci. Technol.* 20 ((2008)), pp. 205–212. DOI: 10.1007/s12217-008-9017-4.
- [124] H. Ohta et al. “TR-1A rocket experiment on nucleate pool boiling heat transfer under microgravity.” In: *ASME J. Dyn. Syst. Meas. Control* 62 ((1997)), pp. 249–256.
- [125] A. Sundaresan, D. Risin, and N. R. Pellis. “Cell Growth in Microgravity.” In: *Reviews in Cell Biology and Molecular Medicine*. American Cancer Society, (2006). ISBN: 9783527600908. DOI: <https://doi.org/10.1002/3527600906.mcb.200300183>. eprint: <https://onlinelibrary.wiley.com/doi/pdf/10.1002/3527600906.mcb.200300183>. URL: <https://onlinelibrary.wiley.com/doi/abs/10.1002/3527600906.mcb.200300183>.
- [126] V. Pletser. “Short duration microgravity experiments in physical and life sciences during parabolic flights: The first 30 ESA campaigns.” In: *Acta Astronaut.* 55.10 ((2004)), pp. 829–854.
- [127] R. R. Dedolph and M. H. Dipert. “The physical basis of gravity stimulus nullification by clinostat rotation.” In: *Plant Physiol.* 47.6 ((1971)), pp. 756–764.
- [128] R. Herranz et al. “Ground-based facilities for simulation of microgravity: Organism-specific recommendations for their use, and recommended terminology.” In: *Astrobiology* 13.1 ((2013)), pp. 1–17.
- [129] S. I. Carlsson et al. “Endothelial stress by gravitational unloading: Effects on cell growth and cytoskeletal organization.” In: *Biochim. Biophys. Acta Mol. Cell Res.* 1642.3 ((2003)), pp. 173–179.
- [130] S. L. Wuest et al. “Simulated microgravity: Critical review on the use of random positioning machines for mammalian cell culture.” In: *BioMed. Res. Int.* 2015 ((2015)), pp. 1–8.

- [131] T. Hoson et al. “Evaluation of the three-dimensional clinostat as a simulator of weightlessness.” In: *Planta* 203.1 ((1997)), S187–S197.
- [132] A. H. Brown, A. O. Dahl, and D. K. Chapman. “Limitation on the use of the horizontal clinostat as a gravity compensator.” In: *Plant Physiol.* 58.2 ((1976)), pp. 127–130.
- [133] G. Albrecht-Buehler. “The simulation of microgravity conditions on the ground.” In: *Gravit. Space Res.* 5.2 ((2007)), pp. 3–10.
- [134] R. J. Hill and L. Eaves. “Nonaxisymmetric shapes of a magnetically levitated and spinning water droplet.” In: *Phys. Rev. Lett.* 101.23 ((2008)), p. 234501.
- [135] J. S. Brooks et al. “New opportunities in science, materials, and biological systems in the low-gravity (magnetic levitation) environment.” In: *J. Appl. Phys.* 87.9 ((2000)), pp. 6194–6199.
- [136] M. A. Weilert et al. “Magnetic levitation and noncoalescence of liquid helium.” In: *Phys. Rev. Lett.* 77.23 ((1996)), p. 4840.
- [137] M. V. Berry and A. K. Geim. “Of flying frogs and levitrons.” In: *Eur. J. Phys.* 18.4 ((1997)), p. 307.
- [138] J. M. Valles Jr et al. “Stable magnetic field gradient levitation of *Xenopus laevis*: Toward low-gravity simulation.” In: *Biophys. J.* 73.2 ((1997)), pp. 1130–1133.
- [139] Y. Liu et al. “Magnetic levitation of large water droplets and mice.” In: *Adv. Space Res.* 45.1 ((2010)), pp. 208–213.
- [140] A. K. Geim. “Everyone’s magnetism.” In: *Phys. Today* 51.9 ((1998)), pp. 36–39.
- [141] J. F. Schenck. “Safety of strong, static magnetic fields.” In: *J. Magn. Reson. Imaging* 12.1 ((2000)), pp. 2–19.
- [142] W. B. High et al. “Subchronic in vivo effects of a high static magnetic field (9.4 Tesla) in rats.” In: *J. Magn. Reson. Imaging* 12.1 ((2000)), pp. 122–139.
- [143] J. M. Valles Jr et al. “Magnetic levitation-based Martian and Lunar gravity simulator.” In: *Adv. Space Res.* 36.1 ((2005)), pp. 114–118.
- [144] T. Chow, P. L. Wong, and K. P. Liu. “Shape effect of magnetic source on stabilizing range of vertical diamagnetic levitation.” In: *IEEE Trans. Magn.* 48.1 ((2011)), pp. 26–30.
- [145] G. Kustler, I. V. Nemoianu, and E. Cazacu. “Theoretical and experimental investigation of multiple horizontal diamagnetically stabilized levitation with permanent magnets.” In: *IEEE Trans. Magn.* 48.12 ((2012)), pp. 4793–4801.

- [146] S. Kuznetsov and J. K. Guest. “Topology optimization of magnetic source distributions for diamagnetic and superconducting levitation.” In: *J. Magn. Magn. Mater.* 438 ((2017)), pp. 60–69.
- [147] Hamid Sanavandi and Wei Guo. “A magnetic levitation based low-gravity simulator with an unprecedented large functional volume.” In: *npj Microgravity* 7.1 (2021), pp. 1–7.
- [148] J. D. Jackson. *Classical Electrodynamics*. 3rd. American Association of Physics Teachers, (1999).
- [149] J. C. Maxwell. *A Treatise on Electricity and Magnetism*. Vol. 1. Clarendon press, (1873).
- [150] E. E. Callaghan and S. H. Maslen. *The magnetic field of a finite solenoid*. Vol. 465. National Aeronautics and Space Administration Washington, (1960).
- [151] A. Caciagli et al. “Exact expression for the magnetic field of a finite cylinder with arbitrary uniform magnetization.” In: *J. Magn. Magn. Mater.* 456 ((2018)), pp. 423–432.
- [152] C. Konishi and I. Mudawar. “Review of flow boiling and critical heat flux in microgravity.” In: *Int. J. Heat Mass Transf.* 80 ((2015)), pp. 469–493.
- [153] J. Straub. “Boiling heat transfer and bubble dynamics in microgravity.” In: *Adv. Heat Transfer*. Vol. 35. Elsevier, (2001), pp. 57–172.
- [154] J. R. Tegart and J. R. Butz. *Analysis of Skylab fluid mechanics science demonstrations*. Martin Marietta Corporation, Prepared for National Aeronautics and Space Administration, (1975).
- [155] G. M. Cooper, R. E. Hausman, and R. E. Hausman. *The Cell: A molecular approach*. Vol. 4. ASM press Washington, DC, (2007).
- [156] D. Eisenberg, W. Kauzmann, and W. Kauzmann. *The Structure and Properties of Water*. Oxford University Press on Demand, (2005).
- [157] S. W. Van Sciver and K. R. Marken. “Superconducting Magnets Above 20 Tesla.” In: *Phys. Today* 55.8 ((2002)), pp. 37–42. DOI: 10.1063/1.1510280.
- [158] I. R. Dixon et al. “Performance of the ultra wide bore 900 MHz NMR magnet at the national high magnetic field laboratory.” In: *IEEE Trans. Appl. Supercond.* 15.2 ((2005)), pp. 1334–1337.
- [159] E. Moser et al. “Ultra-High Field NMR and MRI- The Role of Magnet Technology to Increase Sensitivity and Specificity.” In: *Front. Phys.* 5 ((2017)), p. 33. DOI: 10.3389/fphy.2017.00033.
- [160] W. D. Markiewicz et al. “Design of a superconducting 32-T magnet with REBCO high field coils.” In: *IEEE Trans. Appl. Supercond.* 22.3 ((2011)), pp. 4300704–4300704.

- [161] G. H. Fichtl et al. *Spacelab 3 Mission Science Review*. NASA conference publication. Scientific and Technical Information Branch, (1987). URL: <https://books.google.com/books?id=8r8bAQAIAAJ>.
- [162] S. Hahn et al. “45.5-tesla direct-current magnetic field generated with a high-temperature superconducting magnet.” In: *Nature* 570.7762 ((2019)), pp. 496–499.
- [163] R. Fu et al. “Ultra-wide bore 900 MHz high-resolution NMR at The National High Magnetic Field Laboratory.” In: *J. Magn. Reson. Imaging* 177.1 ((2005)), pp. 1–8.
- [164] C. Hendrickson et al. “21 Tesla Fourier transform ion cyclotron resonance mass spectrometer: A national resource for ultrahigh resolution mass analysis.” In: *J. Am. Soc. Mass Spectrom.* 26.9 ((2015)), pp. 1626–1632.
- [165] V. Braccini et al. “Properties of recent IBAD–MOCVD coated conductors relevant to their high field, low temperature magnet use.” In: *Supercond. Sci. Technol.* 24.3 ((2010)), p. 035001.
- [166] Hamid Sanavandi et al. “Boiling and cavitation caused by transient heat transfer in superfluid helium-4.” In: *Phys. Rev. B* 106 (5 Aug. 2022), p. 054501. DOI: 10.1103/PhysRevB.106.054501. URL: <https://link.aps.org/doi/10.1103/PhysRevB.106.054501>.
- [167] L. D. Landau and E. M. Lifshitz. *Fluid Mechanics*. Second. Vol. 6. Oxford: Pergamon Press, 1987. ISBN: 978-0-08-033933-7.
- [168] A. Marakov et al. “Visualization of the Normal-Fluid Turbulence in Counterflowing Superfluid ^4He .” In: *Phys. Rev. B* 91.9 (Mar. 2015), p. 094503. DOI: 10.1103/PhysRevB.91.094503.
- [169] Jian Gao et al. “Decay of counterflow turbulence in superfluid ^4He .” In: *JETP Lett.* 103.10 (2016), pp. 648–652. DOI: 10.1134/S0021364016100064.
- [170] J. Gao et al. “Energy Spectrum of Thermal Counterflow Turbulence in Superfluid Helium-4.” In: *Phys. Rev. B* 96 (2017), p. 094511. DOI: 10.1103/PhysRevB.96.094511.
- [171] J. Gao et al. “Statistical measurement of counterflow turbulence in superfluid helium-4 using He_2^* tracer-line tracking technique.” In: *J. Low Temp. Phys.* 187 (2017), p. 490. DOI: 10.1007/s10909-016-1681-y.
- [172] J. Gao et al. “Dissipation in quantum turbulence in superfluid ^4He above 1 K.” In: *Phys. Rev. B* 97 (18 2018), p. 184518.
- [173] S. Bao et al. “Statistics of turbulence and intermittency enhancement in superfluid ^4He counterflow.” In: *Phys. Rev. B* 98 (2018), p. 174509. DOI: 10.1103/PhysRevB.98.174509.

- [174] Brian Mastracci and Wei Guo. “Exploration of thermal counterflow in He II using particle tracking velocimetry.” In: *Phys. Rev. Fluids* 3.6 (2018), p. 063304. DOI: 10.1103/PhysRevFluids.3.063304.
- [175] M. O. Lutset, S. K. Nemirovskii, and A. N. Tsoi. “Propagation of Nonlinear Second Sound Waves in He II.” In: *Sov. Phys. JETP* 54.1 (1981), pp. 127–129.
- [176] John C. Cummings, Dieter W. Schmidt, and Wolfgang J. Wagner. “Experiments on Second-Sound Shock Waves in Superfluid Helium.” In: *Phys. Fluids* 21.5 (1978), p. 713. ISSN: 00319171.
- [177] W. Fiszdon and M. v. Schwerdtner. “Influence of Quantum Turbulence on the Evolution of Moderate Plane Second Sound Heat Pulses in Helium II.” In: *J. Low Temp. Phys.* 75.3-4 (May 1989), pp. 253–267. ISSN: 0022-2291, 1573-7357. DOI: 10.1007/BF00681912.
- [178] W. Fiszdon et al. “Temperature Overshoot Due to Quantum Turbulence during the Evolution of Moderate Heat Pulses in He II.” In: *J. Fluid Mech.* 212 (Mar. 1990), p. 663. ISSN: 0022-1120, 1469-7645.
- [179] T. Shimazaki, M. Murakami, and T. Iida. “Second Sound Wave Heat Transfer, Thermal Boundary Layer Formation and Boiling: Highly Transient Heat Transport Phenomena in He II.” In: *Cryogenics* 35.10 (Jan. 1995), pp. 645–651. ISSN: 0011-2275.
- [180] D. K. Hilton and S. W. Van Sciver. “Direct Measurements of Quantum Turbulence Induced by Second Sound Shock Pulses in Helium II.” In: *J. Low Temp. Phys.* 141.1 (Oct. 2005), pp. 47–82. ISSN: 1573-7357.
- [181] P. Zhang, M. Murakami, and R. Z. Wang. “Study of the Transient Thermal Wave Heat Transfer in a Channel Immersed in a Bath of Superfluid Helium.” In: *Int. J. Heat Mass Transf.* 49.7 (Apr. 2006), pp. 1384–1394. ISSN: 0017-9310.
- [182] Timothy N. Turner. “Using Second-Sound Shock Waves to Probe the Intrinsic Critical Velocity of Liquid Helium II.” In: *Phys. Fluids* 26.11 (1983), p. 3227. ISSN: 00319171.
- [183] Shiran Bao and Wei Guo. “Transient heat transfer of superfluid ^4He in nonhomogeneous geometries: Second sound, rarefaction, and thermal layer.” In: *Phys. Rev. B* 103 (13 Apr. 2021), p. 134510. DOI: 10.1103/PhysRevB.103.134510.
- [184] R Wang. “Criterion for quantum turbulence onset after rectangular heat pulse in superfluid helium.” In: *Cryogenics* 35.12 (1995), pp. 883–886.
- [185] BA Danilchenko, MO Lutset, and VN Poroshin. “Limit of transient heat absorption by superfluid helium for very large heat pulses.” In: *Cryogenics* 29.4 (1989), pp. 444–447.
- [186] LP Kondaurova. “Dynamics of vortex line density and heat transfer processes in superfluid helium.” In: *Low Temperature Physics* 44.1 (2018), pp. 29–35.

- [187] Luiza Kondaurova, Victor Efimov, and Alexey Tsoi. “Influence of quantum turbulence on the processes of heat transfer and boiling in superfluid helium.” In: *Journal of Low Temperature Physics* 187.1 (2017), pp. 80–89.
- [188] SK Nemirovskii and AN Tsoi. “Transient thermal and hydrodynamic processes in superfluid helium.” In: *Cryogenics* 29.10 (1989), pp. 985–994.
- [189] Takeshi Shimazaki, Masahide Murakami, and Takashi Kanari. “Measurement of characteristic time for quantized vortex tangle development in He II.” In: *Cryogenics* 38.6 (1998), pp. 601–606. ISSN: 0011-2275. DOI: 10.1016/S0011-2275(97)00154-9.
- [190] A.N. Tsoi and M. O. Lutset. “Boiling up of helium I, helium II, and nitrogen during transient heat release.” In: *Inzhenerno-Fizicheskii Zhurnal* 51 (1985), pp. 5–9.
- [191] Elspeth Latimer et al. “Preparation of Ultrathin Nanowires Using Superfluid Helium Droplets.” In: *Nano Lett.* 14.5 (2014), pp. 2902–2906. DOI: 10.1021/nl500946u.
- [192] Eugene B Gordon et al. “The nanowires growth by laser ablation of metals inside rotating superfluid helium.” In: *Laser Phys. Lett.* 16.2 (Dec. 2018), p. 026002. DOI: 10.1088/1612-202x/aaf6a1.
- [193] S. K. Nemirovskii and W. Fiszdon. “Chaotic quantized vortices and hydrodynamic processes in superfluid helium.” In: *Rev. Mod. Phys.* 67 (1 Jan. 1995), pp. 37–84. DOI: 10.1103/RevModPhys.67.37.
- [194] Sergey K Nemirovskii. “On the closure problem of the coarse-grained hydrodynamics of turbulent superfluids.” In: *Journal of Low Temperature Physics* 201.3 (2020), pp. 254–268.
- [195] Isaac M Khalatnikov. *An introduction to the theory of superfluidity*. CRC Press, 2018.
- [196] V. D. Arp, R. D. McCarty, and B. A. Hands. *HEPAK - Thermophysical Properties of Helium from 0.8K or the Melting Line to 1500K*. Cryodata Inc. Boulder, USA, 2005. URL: <https://htess.com/hepak/>.
- [197] William F. Vinen. “Mutual friction in a heat current in liquid helium II. II. Experiments on transient effects.” In: *Proc. Roy. Soc. A* 240.1220 (1957), pp. 128–143. DOI: 10.1098/rspa.1957.0072.
- [198] William Frank Vinen. “Mutual Friction in a Heat Current in Liquid Helium II. III. Theory of the Mutual Friction.” In: *Proc. R. Soc. Lond. A* 242.1231 (Nov. 1957), pp. 493–515. DOI: 10.1098/rspa.1957.0191.
- [199] Russell J. Donnelly and Carlo F. Barenghi. “The Observed Properties of Liquid Helium at the Saturated Vapor Pressure.” In: *J. Phys. Chem. Ref. Data* 27.6 (1998), pp. 1217–1274. DOI: 10.1063/1.556028.

- [200] K. W. Schwarz. “Three-Dimensional Vortex Dynamics in Superfluid He 4 : Homogeneous Superfluid Turbulence.” In: *Phys. Rev. B* 38.4 (Aug. 1988), pp. 2398–2417. ISSN: 0163-1829. DOI: 10.1103/PhysRevB.38.2398.
- [201] S. K. Nemirovskii. “Macroscopic Dynamics of Superfluid Turbulence.” In: *Low Temp. Phys.* 45.8 (Aug. 2019), pp. 841–847. ISSN: 1063-777X, 1090-6517. DOI: 10.1063/1.5116532.
- [202] R. T. Wang, C. E. Swanson, and R. J. Donnelly. “Anisotropy and Drift of a Vortex Tangle in Helium II.” In: *Phys. Rev. B* 36.10 (Oct. 1987), pp. 5240–5244. DOI: 10.1103/PhysRevB.36.5240.
- [203] Luiza Kondaurova et al. “Structure of a Quantum Vortex Tangle in ^4He Counterflow Turbulence.” In: *Phys. Rev. B* 89.1 (Jan. 2014), p. 014502. DOI: 10.1103/PhysRevB.89.014502.
- [204] R. A. Ashton and J. A. Northby. “Vortex Velocity in Turbulent He II Counterflow.” In: *Phys. Rev. Lett.* 35.25 (Dec. 1975), pp. 1714–1717. DOI: 10.1103/PhysRevLett.35.1714.
- [205] Yuri A Sergeev and Carlo F Barenghi. “Turbulent radial thermal counterflow in the framework of the HVBK model.” In: *EPL (Europhysics Letters)* 128.2 (2019), p. 26001.
- [206] P. Zhang and M. Murakami. “Three dimensionality of pulsed second-sound waves in He II.” In: *Phys. Rev. B* 74 (2 July 2006), p. 024528. DOI: 10.1103/PhysRevB.74.024528.
- [207] D. D. Awschalom and K. W. Schwarz. “Observation of a Remanent Vortex-Line Density in Superfluid Helium.” In: *Phys. Rev. Lett.* 52 (1 Jan. 1984), pp. 49–52. DOI: 10.1103/PhysRevLett.52.49.
- [208] Luiza Kondaurova, Victor Efimov, and Alexey Tsoi. “Influence of Quantum Turbulence on the Processes of Heat Transfer and Boiling in Superfluid Helium.” In: *J. Low Temp. Phys.* 187.1-2 (Apr. 2017), pp. 80–89. ISSN: 0022-2291, 1573-7357. DOI: 10.1007/s10909-016-1731-5.
- [209] Clive A. J. Fletcher and Clive A. J. Fletcher. *Specific Techniques for Different Flow Categories*. 2nd ed., 5th print. Vol. 2. Computational Techniques for Fluid Dynamics. Berlin: Springer, 2003. ISBN: 978-3-540-53601-7.
- [210] W. Guo and H. J. Maris. “Observations of the Motion of Single Electrons in Liquid Helium.” In: *J. Low. Temp. Phys.* 148 (2007), p. 199. DOI: 10.1007/s10909-007-9373-2.
- [211] W. Guo et al. “Experiments with single electrons in liquid helium.” In: *Phys. Rev. B* 79 (5 2009), p. 054515. DOI: 10.1103/PhysRevB.79.054515.
- [212] C. E. Brennen. *Cavitation and Bubble Dynamics*. Cambridge: Cambridge University Press, 2013. DOI: 10.1017/CB09781107338760.

- [213] Shiran Bao and Wei Guo. “Quench-Spot Detection for Superconducting Accelerator Cavities Via Flow Visualization in Superfluid Helium-4.” In: *Phys. Rev. Appl.* 11 (2019), p. 044003. DOI: [10.1103/PhysRevApplied.11.044003](https://doi.org/10.1103/PhysRevApplied.11.044003).
- [214] N. Garceau et al. “The design and testing of a liquid helium cooled tube system for simulating sudden vacuum loss in particle accelerators.” In: *Cryogenics* 100 (2019), pp. 92–96. DOI: <https://doi.org/10.1016/j.cryogenics.2019.04.012>.

BIOGRAPHICAL SKETCH

Hamid Sanavandi ... his Doctor of Philosophy in Mechanical Engineering from FSU, Tallahassee, Florida, in 2022. He received his Master of Science in Mechanical Engineering from KNTU, Tehran, Iran, in 2015. He received his Bachelor of Science in Mechanical Engineering from UT, Tehran, Iran, in 2012. He once wrote down his goals on a paper. Among them was: "... I am going to obtain my PhD in Mechanical Engineering in a prestigious university in the United States". Ten months later, despite all difficulties, delays out of his control, and immigration limitations, he was flying to seek success where his hard work would be valued. And yes, he keeps that piece of paper to this day!

The power of dreaming moves mountains.